

AD _____

Award Number: W81XWH-FE~~FE~~ JH

TITLE: ~~Ö^ç^[[] { ^} oí -T æ } ^c&ü^•[] æ &^ÁQ æ ã * Áq { æ\^!•Á[!Á!æ { æ&Ó!æ ÁQb!^~~

PRINCIPAL INVESTIGATOR: ~~Ö:ÖÖ, æoT æ\ P æ& ^~~

CONTRACTING ORGANIZATION: Y æ } ^Áæ^ÁV, ã^!•ã ÊÖ^d[æT Q! ÆG

REPORT DATE: Jul^ ÁGFG

TYPE OF REPORT: Annual

PREPARED FOR: U.S. Army Medical Research and Materiel Command
Fort Detrick, Maryland 21702-5012

DISTRIBUTION STATEMENT: Approved for public release; distribution unlimited

The views, opinions and/or findings contained in this report are those of the author(s) and should not be construed as an official Department of the Army position, policy or decision unless so designated by other documentation.

REPORT DOCUMENTATION PAGE				Form Approved OMB No. 0704-0188	
Public reporting burden for this collection of information is estimated to average 1 hour per response, including the time for reviewing instructions, searching existing data sources, gathering and maintaining the data needed, and completing and reviewing this collection of information. Send comments regarding this burden estimate or any other aspect of this collection of information, including suggestions for reducing this burden to Department of Defense, Washington Headquarters Services, Directorate for Information Operations and Reports (0704-0188), 1215 Jefferson Davis Highway, Suite 1204, Arlington, VA 22202-4302. Respondents should be aware that notwithstanding any other provision of law, no person shall be subject to any penalty for failing to comply with a collection of information if it does not display a currently valid OMB control number. PLEASE DO NOT RETURN YOUR FORM TO THE ABOVE ADDRESS.					
1. REPORT DATE (DD-MM-YYYY) 01-07-2012		2. REPORT TYPE Annual		3. DATES COVERED (From - To) 2 Jun 2011 - 1 Jun 2012	
4. TITLE AND SUBTITLE Development of Magnetic Resonance Imaging Biomarkers for Traumatic Brain Injury				5a. CONTRACT NUMBER	
				5b. GRANT NUMBER W81XWH-11-1-0493	
				5c. PROGRAM ELEMENT NUMBER	
6. AUTHOR(S) Dr. Ewart Mark Haacke E-Mail: nmrimaging@aol.com				5d. PROJECT NUMBER	
				5e. TASK NUMBER	
				5f. WORK UNIT NUMBER	
7. PERFORMING ORGANIZATION NAME(S) AND ADDRESS(ES) Wayne State University Detroit, MI 48202				8. PERFORMING ORGANIZATION REPORT NUMBER	
9. SPONSORING / MONITORING AGENCY NAME(S) AND ADDRESS(ES) U.S. Army Medical Research and Materiel Command Fort Detrick, Maryland 21702-5012				10. SPONSOR/MONITOR'S ACRONYM(S)	
				11. SPONSOR/MONITOR'S REPORT NUMBER(S)	
12. DISTRIBUTION / AVAILABILITY STATEMENT Approved for Public Release; Distribution Unlimited					
13. SUPPLEMENTARY NOTES					
14. ABSTRACT The purpose of this research program is to develop an imaging-based protocol to improve diagnosis and outcome prediction of mild traumatic brain injury (mTBI). It includes the development of a modern technology for processing susceptibility maps to evaluate the presence of bleeding and deoxyhemoglobin and the study of sensitivity of new MR imaging technology in detecting mild TBI. Our major findings relate directly to our specific aims. First, we have demonstrated that these new advanced MRI methods nicely complement conventional imaging methods in their ability to detect mTBI in the acute setting. Second, susceptibility weighted imaging and mapping (SWIM) are able to delineate venous structures and microbleeds making it possible to quantify and monitor evolution of pathological changes. Third, we have developed the process by which to evaluate DTI data throughout the entire brain to look for local variations in ADC and FA values to assess tissue damage. And fourth, we have begun to collect imaging and neuropsychological data for both volunteers and mTBI patients during the last quarter of this year. The significance of this work to date is that we are now able to find evidence of damage in mTBI where that has heretofore been difficult with cMRI.					
15. SUBJECT TERMS Mild traumatic brain injury, susceptibility weighted imaging and mapping,					
16. SECURITY CLASSIFICATION OF:			17. LIMITATION OF ABSTRACT UU	18. NUMBER OF PAGES 84	19a. NAME OF RESPONSIBLE PERSON USAMRMC
a. REPORT U	b. ABSTRACT U	c. THIS PAGE U			19b. TELEPHONE NUMBER (include area code)

Table of Contents

	<u>Page</u>
Introduction.....	5
Body.....	6-13
Key Research Accomplishments.....	14
Reportable Outcomes.....	15-16
Conclusion.....	17
Appendices.....	Attachment

INTRODUCTION

Background: Traumatic brain injury (TBI) has been labeled as a “signature wound” in the anti-terrorism wars in Iraq and Afghanistan. 15% - 25% of surveyed returning service members have been reported to have possible long-term mild traumatic brain injury (mTBI) or concussion. In the civilian sector, the prolonged neuro-cognitive and functional symptoms following mTBI affects over 1.2 million Americans annually. However, our understanding of the neuropathology of mTBI and its recovery process is still very limited due to the lack of sensitive clinical and diagnostic tools. First, current TBI classification scales are mainly based on results from computed tomography (CT) scans of moderate to severe TBI patients, and thus can hardly be applied to mTBI cases. Secondly, current laboratory biological markers, clinical CT and conventional magnetic resonance imaging (MRI) are either insensitive or not specific to the subtle abnormalities in mTBI and poorly predict patient’s long-term outcome. It is in urgent need of developing a set of advanced MR imaging biomarkers that can: i) be sensitive enough to differentiate mTBI patient population from normal healthy ones, ii) have the potential for outcome prediction; and iii) assist in management of mTBI patients in acute settings.

Objective/Hypothesis: The overall goal of the current research is to develop imaging-based biomarkers to improve diagnosis and outcome prediction of mTBI. Advanced MRI techniques reveal many more details than conventional imaging. For example, susceptibility weighted imaging (SWI) and susceptibility mapping (SWIM) can detect and quantify temporal reduction of hemorrhagic lesions associated with mTBI patients’ functional outcome and diffusion tensor imaging (DTI) can detect axonal injury at the acute stage and possible changes over time. As the next generation of SWI developed in our lab, SWIM will be used to quantify iron in microbleeds and oxygen saturation in major veins throughout the brain. Our central hypothesis is that axonal injury (measured by DTI) and vascular damage (detected as hemorrhagic lesions by SWI/SWIM) are important pathologies in mTBI that are associated with patients’ neurocognitive and clinical symptoms in their recovery.

Study Design: Adult mTBI patients will be screened and enrolled at the acute stage (within 24 hours after injury) from the emergency department of our local Level-One Trauma Center. Both up-to-60-minute MRI scan and neuropsychological/clinical assessment will be conducted in mTBI patients. In the subacute (1 month) and chronic (6 months) stages after injury, the patients will be brought back to repeat both the MRI scans and neurocognitive evaluations. Age/gender/education-matched healthy controls will be recruited and followed up using the same imaging and neuropsychological protocol of evaluation.

Specific Aims: **Specific Aim 1** is to assess whether the advanced MRI data (SWI and DTI) acquired acutely (within 24 hours after injury) are more sensitive than conventional imaging (CT and cMRI) in detecting mTBI. **Specific Aim 2** is to determine at what time point after the injury (i.e., acute, subacute and chronic) these advanced MR techniques can differentiate mTBI patients from healthy controls. **Specific Aim 3** is to use susceptibility weighted imaging and mapping (SWIM), our next generation of SWI technique, to quantify the amount of iron in microbleeds, to monitor any changes (evolution) of the microbleed over time and to monitor oxygen saturation compared to normal volunteers. And **Specific Aim 4** is to determine which MRI indices have statistically significant associations with neurocognitive outcome in mTBI patients over all time points.

BODY

Summary of the Statement of Work for Phase I:

Phase I (Years 1-2): recruit a cohort of 50 mTBI patients from the emergency setting of our local Level-One trauma center, and 50 non-TBI volunteers to establish and validate an image-based diagnostic approach to brain injury.

- a) Screen and enroll mTBI patients; perform the MRI protocol (conventional imaging, DTI and SWI); conduct NP tests and clinical outcome measures.

Due to the late approval of IRB, we started enrollment fairly late (March, 2012). To date, we have successfully recruited two mTBI patients and scanned them at the acute stage (within 24 hours after injury).

- b) Screen and enroll healthy volunteers and perform the same procedures as mentioned above.

We have successfully enrolled 7 control subjects in the past month.

- c) Follow up mTBI patients and controls at 1-month and 6-months after injury using the same imaging protocol, NP tests and outcome measures.

We have successfully performed 1-month follow up in our two patients and two controls.

- d) Analyze the data and establish a baseline imaging database for mTBI patients and normals.

We have established the quantification schemes necessary to analyze this data for DTI and SWIM. We are in the process of creating an internal database from which we can gather all relevant quantitative information such as total lesion load, FA histograms and mean FA.

- e) Report preliminary data by presenting it to conferences or publish it in TBI and imaging related journals.

We have published 2 papers and 2 book chapters. We have also given 9 presentations related to this work during the last year by Prof. Haacke and Prof. Kou. The details are given in the reportable results section.

- f) Develop and use SWI and SWIM for use in evaluating abnormal vasculature and microbleeds in mTBI patients.

We are delighted to report that we have made major progress in the evaluation of cerebral microbleeds using a new iterative SWIM algorithm. The reader is referred to the paper by J. Tang et al. “[Improving susceptibility mapping using a threshold-based K-space/image domain iterative reconstruction approach.](#)”, MRM, June 26, 2012, epub, ahead of print for a detailed description of this new concept. However, the basic concept is given below.

While we were pending for the IRB approval of our human data collection, we spent considerable time on the methodology itself and have made some dramatic progress in this direction. We have just published a paper on an advanced form of susceptibility mapping (SM) which we refer to as “Iterative SWIM”. The concept is to take the first guess of the SM and keep only the highest components and then do a forward

model. Now we use the ill-defined portions of k-space from this forward data and embed it into the original k-space data and reconstruct. This has a dramatic effect in terms of removing artifacts. An example data simulation is shown below (Figure 1). Note that even after the first iteration there is a dramatic improvement in the image.

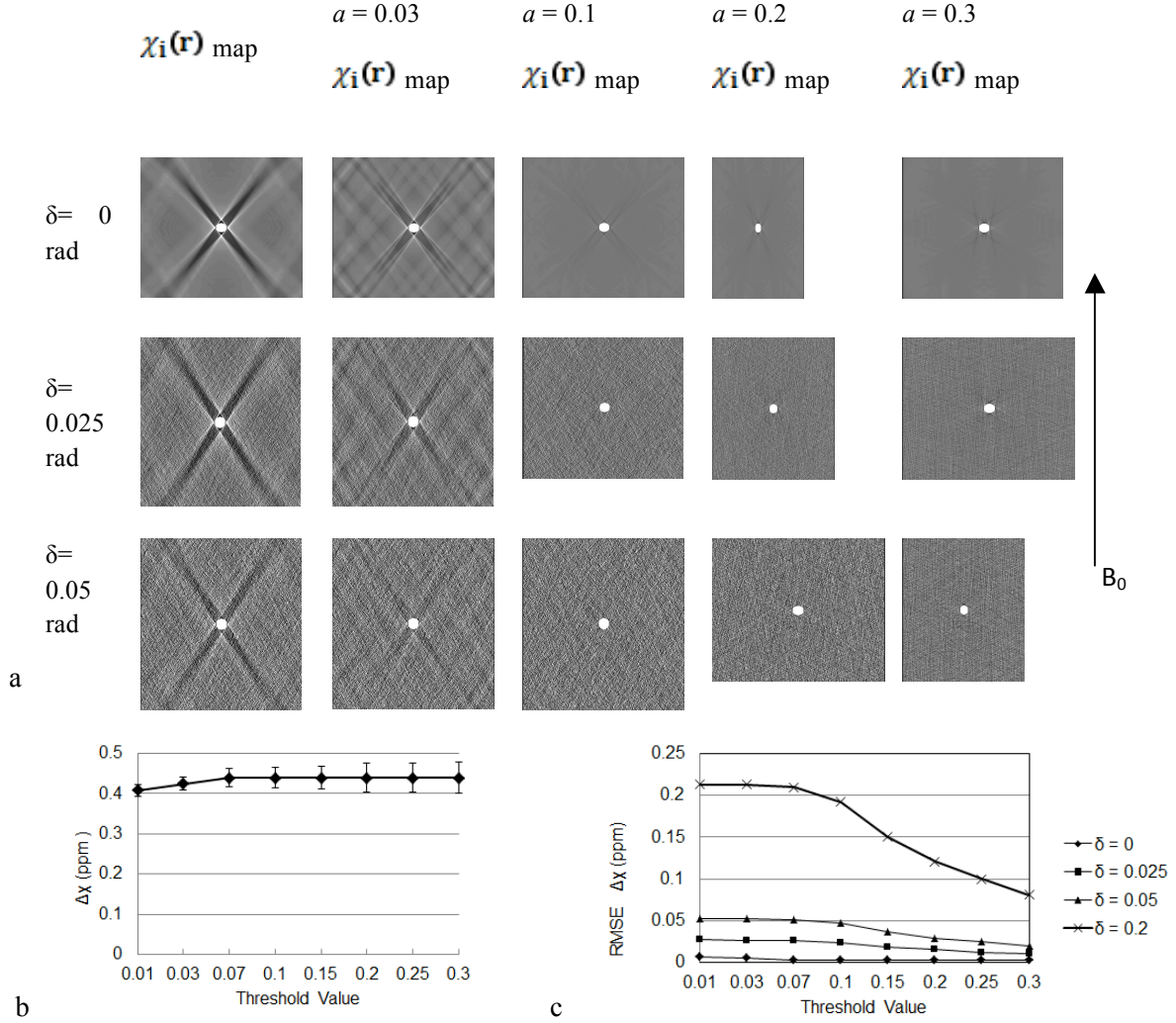


Figure 1: Simulations showing the comparison of the calculated susceptibility distributions for a cylinder perpendicular to B_0 , indicated by a white long arrow, at different threshold values (a) applied to $g(k)$ as well as the initial $\chi_i(\mathbf{r})$ map. The diameter of the cylinder is 32 pixels with a susceptibility $\Delta\chi$ of 0.45 ppm inside the cylinder. a) The top row of images shows calculations with no added phase noise and the second and the third row shows calculations with added phase noises $\delta = 0.025$ and 0.05 radians, respectively. The first column of images are initial $\chi_i(\mathbf{r})$ maps for reference. b) The variation of the mean calculated susceptibility inside the cylinder with different threshold value, a . The mean susceptibility value is independent of the noise level; therefore, only mean value from $\delta = 0$ is provided. The error bar shows the standard deviation (SD) of the calculated susceptibility values. c) The variation of the root

mean squared error (RMSE) of the susceptibility values outside the cylinder as a function of the threshold value, a , and the noise level.

g) Simultaneous acquisition of both MR angiography and venography data.

We have developed a dual echo SWI technique that will provide the ability to not only perform SWI and SWIM but also to calculate $T2^*$. This is not the ordinary double echo sequence but a fully flow compensated double echo sequence so no interference from arteries takes place. It can image both the arteries and veins at the same time, which could potentially assess a relative complete picture of vessel damage after brain injury (see Figure 2). Specifically, we have designed a flow rephase/dephase interleaved double-echo GRE sequence which offers fully flow rephased SWI data for venography, and TOF MRA plus flow dephased data for enhancing angiography using a non-linear subtraction (NLS) method. To our knowledge, currently no MR method other than the interleaved double-echo sequence we proposed can provide all the data needed for both MRAV imaging and selective MRA enhancement in a single scan. Three different types of image contrast, i.e., TOF MRA, SWI and flow dephased dark blood images, could be obtained simultaneously with perfect alignment to each other so that no realignment process is necessary. In conjunction with NLS, one can obtain high resolution SWI and enhanced TOF MRA without the need for contrast agent (Figure 2 a-b), and the process can be easily automated without much additional computational power. NLS offers a clean angiography free of venous contamination as if acquired with maximal TOF effects. Most noticeably, NLS seems to even outperform the low dose CE TOF data by its higher artery-tissue contrast (Figure 2 c-e), extra revelation of some small arteries (e.g. at the frontal lobe), uniform background signal and the lack of veins (except for the easily distinguishable superior sagittal sinus). For future works, the acquisition time may be further reduced to provide whole brain coverage using a segmented echo planar imaging (seg-EPI) readout approach or compress sensing (CS) since the subtracted images have highly sparse information.

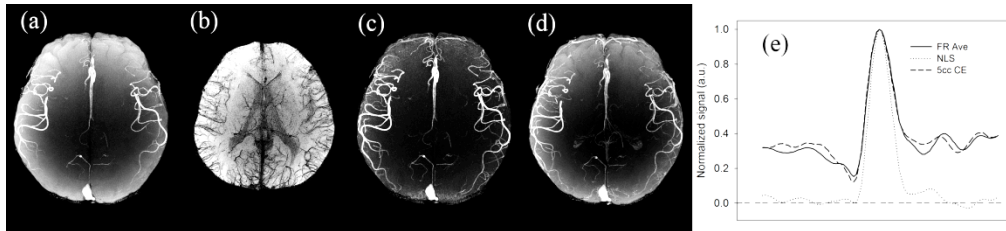


Figure 2: MIP images of (a) normal TOF MRA; (b) SWI; (c) NLS and (d) low dose CE MRA with 5cc gadopentetate dimeglumine. (a-c) were collected with a single scan of the interleaved double-echo sequence before the use of contrast agent. (e) Normalized profiles of one representative artery, extracted from the correspondent single slice images.

h) Investigate the early response of the neurovascular system to brain concussion

In our preliminary study, we investigated the neural vascular response to mild TBI at the acute stage. Specifically, we adopted a combined use of both SWIM and ASL to answer this question.

Subject Enrollment: Twelve mTBI patients were recruited in emergency setting in our Level-1 trauma center. Eighteen aged- and gender-matched healthy controls were also recruited for comparison. All patients met the definition of mTBI by the American Congress of Rehabilitation Medicine (ACRM) with Glasgow Coma Scale (GCS) score of 13-15 at emergency entry. All patients completed a short

neurocognitive test, standard assessment of concussion (SAC), at the acute stage. SAC is a short instrument to measure patients orientation, delayed recall, attention, and executive function.

SWIM Processing: All SWI images were processed to produce SWIM data by using our previously developed method in our in-house developed SPIN software [1]. Specifically, the following steps were used: a) High pass filtering of original phase image to get SWI phase image, b) Inverse transform to generate susceptibility maps of the veins, c) Regularization and interpolation of the data in k-space of the phase image to reduce reconstruction artifacts, and d) finally, minimum intensity projection (mIP) of slices over 8 mm thickness.

After SWIM processing, eight major veins and small transmedullar veins were selected by using semi-automated region of interest (ROI) analysis to quantify blood oxygen saturation of each one (see Figure 3). A student t-test was used to compare the control and patient group data.

ASL Data Processing: First, the skull-stripped untagged T2 weighted image was used to create a mask to skull-strip the relative CBF (rCBF) images. The skull-stripped untagged T2 weighted images were then normalized to the T1 weighted ICBM template by using SPM8 to generate a transformation matrix. Next, the transformation matrix was applied to the rCBF images. Then, the Wake Forest University (WFU) Pickatlas, which is in the same space as ICBM template, was used to extract the rCBF values from specific predefined structures and lobes. rCBF values from frontal, parietal, occipital and temporal lobes were extracted. In addition, values from thalamus and basal ganglia, including caudate nucleus, putamen and globus pallidus, were also extracted.

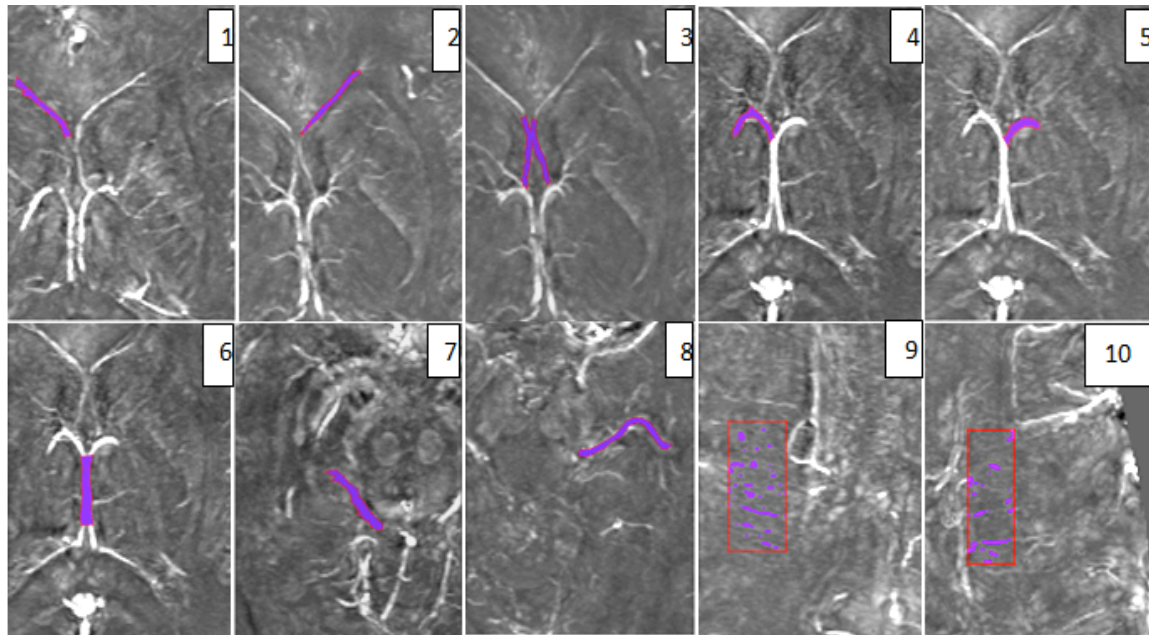


Figure 3: Measurement of susceptibility of major veins. As numbered on the figure, the major veins are 1-Septal Vein (right), 2-Septal Vein (left), 3- Central Septal Vein, 4-Thalamic Striatal Vein (right), 5-Thalamic Striatal Vein (left), 6-Internal Cerebral Vein, 7-Basilar Vein of Rosenthal (right), 8-Basilar Vein of Rosenthal (left), 9-Transmedullar Vein (right), and 10-Transmedullar Vein (left).

Results:

Our data demonstrate that: a) patient group has significant lower susceptibility signal than control group in left thalamus striatal veins (See Figure 4), which implies that patient group has lower deoxygenation in thalamus region than controls; b) Patient group has significant higher CBF levels than control group in left frontal lobe and left striatal region, including caudate, putamen and globuspallidus (See Table 1); c) patient group demonstrated significantly reduced SAC scores than published normative data, especially in delayed recall (See Figure 5); and d) the imaging data is not correlated with SAC data.

Table 1. rCBF of Major Brain Structures

Structure	Thal-L	Thal-R	Stri-L	Stri-R	Caud-L	Caud-R	Put-L	Put-R	GP-L	GP-R
Control	2184.25	2217.42	2127.25	2145.00	2114.42	2123.83	2136.83	2154.42	2151.58	2125.83
Patients	2236.86	2272.43	2190.50	2201.00	2172.67	2182.00	2188.50	2216.00	2190.33	2131.67
T-Test	0.23	0.28	0.02	0.14	0.02	0.09	0.03	0.14	0.12	0.96

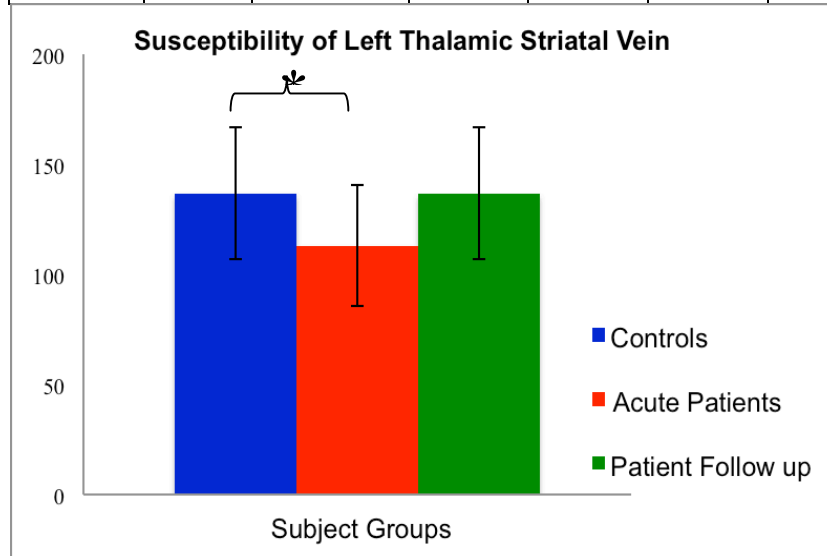


Figure 4: Comparison of left Thalamic Striatal vein at different time points. Star sign indicates statistical significance.

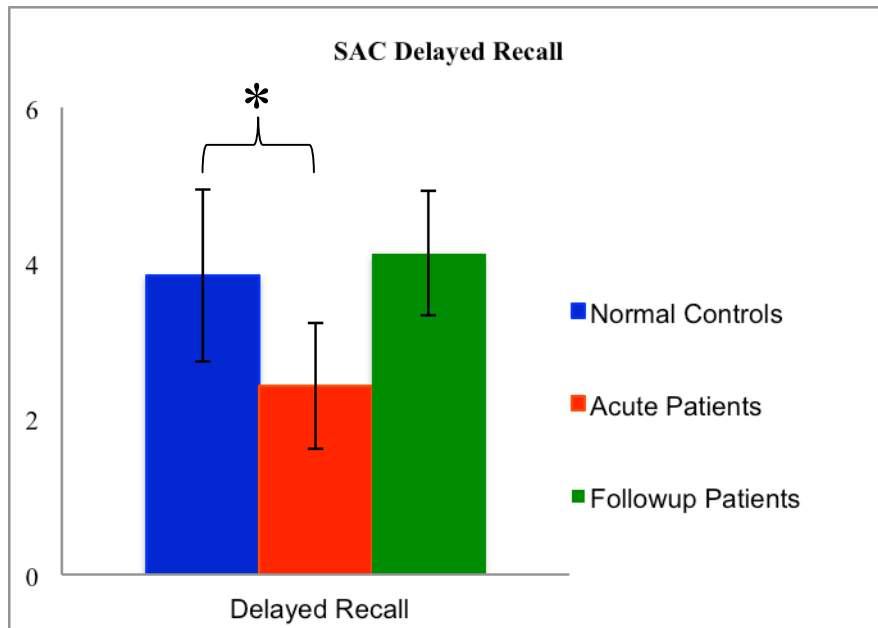


Figure 5: Testing scores of Delayed Recall in the Standard Assessment of Concussion (SAC). As indicated by the bar chart, patients at acute stage have significantly lower scores of delayed recall, which suggests of memory problem.

i) *Investigating medullary vein damage*

A new dimension in imaging technology is the discovery of vascular damage in the form of extravasated blood, thrombus and reduced levels of oxygenation that may better illuminate our understanding of brain injury, particularly related to trauma. Using the SWI and SWIM technology discussed above, we have recognized that there are major changes in iron content and local oxygen saturation, important for evaluating potential changes in local perfusion or tissue function (similar to what is seen in stroke using SWI). SWIM can also be used to monitor changes in iron content over time which can be used to see if previous iron deposition is being resorbed or if bleeding continues, both important diagnostic pieces of information for the clinician.

In this current project, we have demonstrated that there is a lower impact load, either inertia or direct impact forces, that may damage only veins, and we have shown medullary vein damage that hasn't been visualized with other techniques (Figure 6). The medullary veins drain the frontal white matter of the brain, so reduced blood flow here could possibly impair the higher level frontal neurocognitive function. Treatments that improve blood flow to the brain, then, might be a promising direction to pursue.

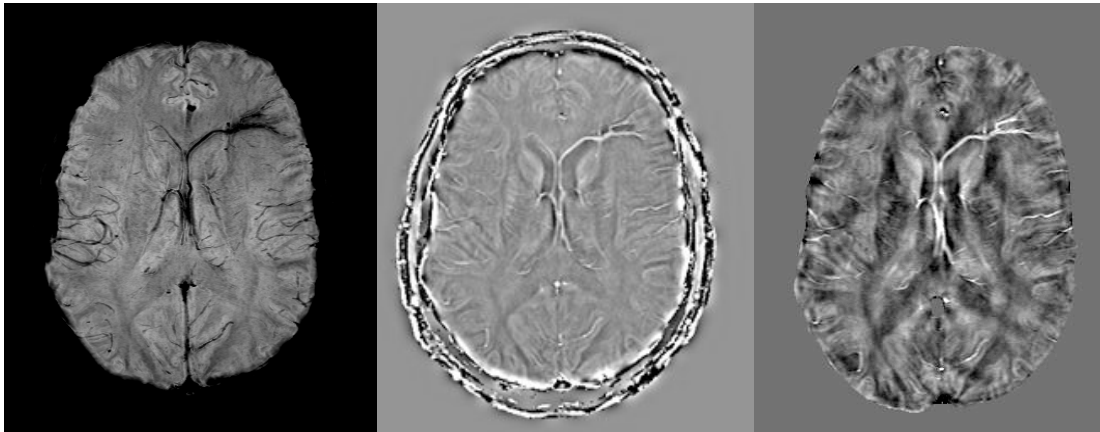


Figure 6: An example mild traumatic brain injury case in the presence of both blast and subsequent traumatic brain injury. The left septal vein and medullary veins draining into it are both show abnormal signal representing either iron deposition or increased levels of deoxyhemoglobin or both. Left image: SWI data. Middle image: SWI filtered phase. Right image: SWIM data showing quantified iron content.

j) Investigating medullary vein structure in three dimensions

Overall results from modeling of major vessels suggests that blood vessels increase the stiffness of the brain and help to resist both rotational and linear impulses and may also increase the threshold of neural injury. However, there is no data that describe the mechanical interaction between the vessels and brain. Medullary vein damage may be due to the presence of internal shear forces (intracerebral stresses). How this occurs likely depends on the stiffness and natural frequency of the structure impacted. For impacts with structures of relatively soft stiffness the brain tends to move with the skull because of the predominantly low frequencies involved in these impacts. These movements result in intracerebral strains (ICS) that can produce lesions in the central parts of the brain. Knowing the tissue properties and the local structures of the vessels and how they are embedded in the surrounding tissue is necessary for proper modeling of the problem. The SWI and MRA data that we have collected makes it possible to create a detailed model of the medullary veins down to 250 microns in size (see Figure 7). Armed with this model and estimates for the tissue properties it may be possible in the future to predict local venous damage. The determination of vessel vulnerability could help engineer safety devices such as helmets to protect the brain from forces that cause venous damage.

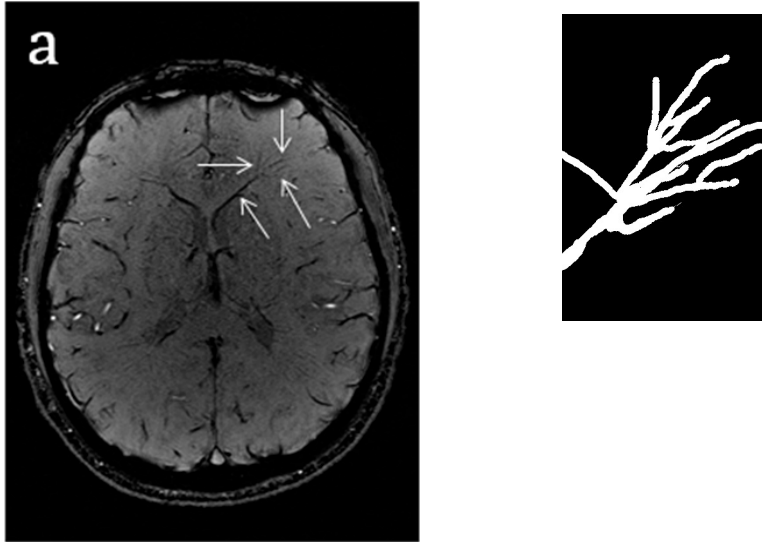


Figure 7: Modeling the medullary veins. An SWI projection image is used to find the medullary veins and then they are extracted in 3D. a) An example image from SWI data showing the septal vein and the confluence of several medullary veins. b) A projection of a 3D model of the medullary veins branching off the septal vein. The resolution in the model is 62.5 microns and the vessels range in size from 1mm (the septal vein) to the first branchings (0.5mm) to the second branchings (0.25mm). These veins can be damaged in frontal or side impact.

KEY RESEARCH ACCOMPLISHMENTS

The following accomplishments have been made in the past year:

- Final approval of study protocol by three Institutional Review Boards (IRBs).
- Recruitment and follow up of patients and controls is established and in progress.
- Analysis of preliminary data. Our data demonstrated an increased blood flow as early response of mild TBI patients.
- A new finding of medullary vein damage has been discovered that is present not only in moderate and severe TBI but also in mild TBI.
- Technical development of susceptibility weighted imaging and mapping (SWIM), including:
 - A method of simultaneous acquisition of both MR angiography and venography has been developed.
 - An advanced iterative approach has been developed to improve the post processing of SWIM data.

REPORTABLE OUTCOMES

Papers:

- a) A review on SWI and fMRI was published: E. M. Haacke and Y. Ye. "The role of susceptibility weighted imaging in functional MRI". Neuroimage: 2012 (epub, ahead of print).
- b) DTI paper on mild TBI. We are currently working on a paper related with DTI study of mild TBI by using our DTI analysis approach as mentioned above.
- c) A book chapter entitled "The presence of venous damage and microbleeds in traumatic brain injury and the potential future role of angiographic and perfusion magnetic resonance imaging" is in press.
- d) A book chapter is published: Zhifeng Kou, Randall R Benson, E Mark Haacke. "Advanced Neuroimaging of Mild Traumatic Brain Injury", in "Biomarkers for Traumatic Brain Injury," edited by Svetlana Dambinova, Ronald L Hayes, Kevin K.W. Wang and David E Thurston. Royal Society of Chemistry, May, 2012.
- e) A paper on the advancement of SWIM has been accepted in MRM. J. Tang et al. "Improving susceptibility mapping using a threshold-based K-space/image domain iterative reconstruction approach.", MRM, Juen 26, 2012, epub, ahead of print.
- f) A manuscript comparing ASL with SWIM data is in progress.

Presentations:

Our group has given a number of presentations in national and international meetings.

2011

- a) The project PI, Dr. E Mark Haacke, was invited by the Human Brain Mapping society to give a presentation on SWIM on June 29th, 2011, Quebec City, Canada.
- b) Dr. Haacke also met with members of Senator Harry Reid's office in Las Vegas regarding his research on August 30th, 2011
- c) Dr. Zhifeng Kou gave a plenary presentation on brain trauma in 2011 NABIS meeting on September 15th, 2011, New Orleans, Louisiana.
- d) Dr. Haacke organized and held a TBI Workshop on November 18, 2011 from 8:00am – 4:00pm at Wayne State University. There were four topic sessions with five speakers in each section for around twenty short talks. Dr. Haacke spoke about the new venous concepts and Dr. Kou about progress in mild TBI.
- e) Wayne State University - WSU Program in Traumatic Brain Injury Research (PTBIR). December 8th, 2011.

2012

- f) Henry Ford Hospital. The role of the vasculature in neurodegenerative disease with a focus on TBI and CCSVI. January 5th, 2012.
- g) The Society for Cardiovascular Magnetic Resonance. CCSVI: Abnormal Venous Flow and Neurodegenerative Disease. February 5th, 2012.
- h) SWI fMRI. American Society of Functional Neuroradiology (ASFNR) 6th Annual Scientific Meeting. March 7th, 2012. Orlando, FL, USA.
- i) SWI: Advanced Applications, Oxygenation, Phase Quantitation. American Society of Functional Neuroradiology (ASFNR) 6th Annual Scientific Meeting. March 8th, 2012. Orlando, FL, USA.
- j) Moderator at the American Society of Functional Neuroradiology (ASFNR) 6th Annual Scientific Meeting. Case Based SWI and Advanced Imaging. March 8th, 2012. Orlando, FL, USA.

k) Susceptibility weighted imaging at the 19th Annual Audiology Conference at the VA Hospital in Johnson City, Tennessee, on June 21st, 2012.

Grants, Honors and Awards

- Dr. Zhifeng Kou obtained a Seed Grant from the International Society for Magnetic Resonance in Medicine (ISMRM) in the annual conference in Melbourne, Australia in May 2012.
- Dr. Zhifeng Kou won the prestigious Charles Hayes award from the North American Brain Injury Society (NABIS) in 2011.

CONCLUSION

Our work during this first year has already led to some major breakthroughs in understanding traumatic brain injury. First, we have observed medullary vein damage even in mild TBI. The implications for this are two-fold: we may be able to understand why certain individuals are suffering from frontal white matter neurocognitive problems and we may be able to propose a treatment for these individuals. Second, we have developed a power quantitative susceptibility mapping advance called iterative SWIM which opens the door to mapping bleeding in TBI. This has the importance of monitoring current damage and patient recovery in the sense that one can follow tissue recovery and clearing of iron from the tissue. Third, we have married SWI and MRA to allow for a complete vascular study of TBI. The impact here is that we should be able to better understand the brain's hemodynamics post trauma. In summary, we are on track with our technical development and are now on track to collecting the human data. Although this may take some time, we anticipate being able to complete this data collection by the end of year two. Our future work will continue along the lines proposed in the original statement of work where we will compare the imaging at different time points and look for biomarkers of patient outcomes.

Improving Susceptibility Mapping Using a Threshold-Based K-Space/Image Domain Iterative Reconstruction Approach

J. Tang,¹ S. Liu,¹ J. Neelavalli,² Y. C. N. Cheng,² S. Buch,¹ and E. M. Haacke^{1–3*}

To improve susceptibility quantification, a threshold-based k-space/image domain iterative approach that uses geometric information from the susceptibility map itself as a constraint to overcome the ill-posed nature of the inverse filter is introduced. Simulations were used to study the accuracy of the method and its robustness in the presence of noise. In vivo data were processed and analyzed using this method. Both simulations and in vivo results show that most streaking artifacts inside the susceptibility map caused by the ill-defined inverse filter were suppressed by the iterative approach. In simulated data, the bias toward lower mean susceptibility values inside vessels has been shown to decrease from around 10% to 2% when choosing an appropriate threshold value for the proposed iterative method. Typically, three iterations are sufficient for this approach to converge and this process takes less than 30 s to process a $512 \times 512 \times 256$ dataset. This iterative method improves quantification of susceptibility inside vessels and reduces streaking artifacts throughout the brain for data collected from a single-orientation acquisition. This approach has been applied to vessels alone as well as to vessels and other structures with lower susceptibility to generate whole brain susceptibility maps with significantly reduced streaking artifacts. *Magn Reson Med* 000:000–000, 2012. © 2012 Wiley Periodicals, Inc.

Key words: oxygen saturation; susceptibility mapping; susceptibility weighted imaging

Susceptibility weighted imaging (SWI) using phase information has become an important clinical tool (1–3). However, the use of phase information itself has stimulated great interest both as a source of contrast (4–6) and a source for producing susceptibility maps (SM) (7–24). The impetus for solving the inverse problem from magnetic field perturbation came from the work described by Deville et al. (25). This was noted by Marques and Bowtell in 2005 (26). Salomir et al. (27) were the first group to utilize this concept in MRI. Unfortunately, this inverse process is ill-posed and requires a regularization

procedure to estimate the SM. There are a variety of approaches to tackle this problem (7–24). One unique method uses a multiple orientation data acquisition to remove the singularities (17). Constrained regularizations (14,20,22,23) have shown good overall results, but they require longer reconstruction times and assumptions about the contrast in or near the object to be detected. Threshold-based, single-orientation regularization methods (TBSO) (11,15,18,24) provide the least acquisition time and the shortest computational time to calculate SM. However, their calculated SMs lead to underestimated susceptibility values ($\Delta\chi$) and display severe streaking artifacts especially around structures with large $\Delta\chi$, such as veins or parts of the basal ganglia.

Based on TBSO approaches, we propose an iterative method to overcome the singularities in the inverse filter and produce improved accuracy for susceptibility mapping. In this approach, we iteratively replace k-space values associated with the SM, $\chi(k)$, near the singularities to obtain an almost artifact free SM, $\chi(r)$. The k-space values used for substitutions are estimated using structural information from the masked version of $\chi(r)$. Simulations using 2D cylinders and full brain 3D models were performed to examine the efficacy of this iterative approach. High resolution human data are also evaluated.

MATERIALS AND METHODS

Briefly, the expression for the susceptibility distribution (26,27) derived from the phase data can be written as (for a right handed system (28)):

$$\chi(r) = \text{FT}^{-1} \left[\frac{1}{g(k)} \times \text{FT} \left[\frac{\Phi(r)}{-\gamma B_0 T_E} \right] \right] \quad [1]$$

where,

$$g(k) = \frac{1}{3} - \frac{k_z^2}{k_x^2 + k_y^2 + k_z^2} \quad [2]$$

and $\Phi(r)$ is the phase distribution, T_E is the echo time, γ is the gyromagnetic ratio for hydrogen protons, B_0 is the main field strength, k_x , k_y , and k_z are coordinates in k-space, and $g(k)$ is the Green's function or filter. Clearly, the analytic inverse filter $g^{-1}(k) = 1/g(k)$, is ill-posed when $g(k)$ is equal or close to zero, i.e., points on or near two conical surfaces in k-space at the magic angles of 54.7° and 125.3° from the B_0 axis. This ill-posedness

¹School of Biomedical Engineering, McMaster University, Hamilton, Ontario, Canada.

²Department of Radiology, Wayne State University, Detroit, Michigan, USA.

³The MRI Institute for Biomedical Research, Detroit, Michigan, USA.

Grant sponsor: National Institutes of Health; Grant numbers: NHLBI R01HL062983-A4, NHLBI R21 HL 108230-A2; Grant sponsor: DoD grant; Grant number: W81XWH-11-1-0493.

*Correspondence to: E. Mark Haacke, PhD, Department of Radiology, Wayne State University, 3990 John R Street, Detroit MI 48201, USA. E-mail: nmrimaging@aol.com

Received 13 September 2011; revised 29 May 2012; accepted 30 May 2012.

DOI 10.1002/mrm.24384

Published online in Wiley Online Library (wileyonlinelibrary.com).

© 2012 Wiley Periodicals, Inc.

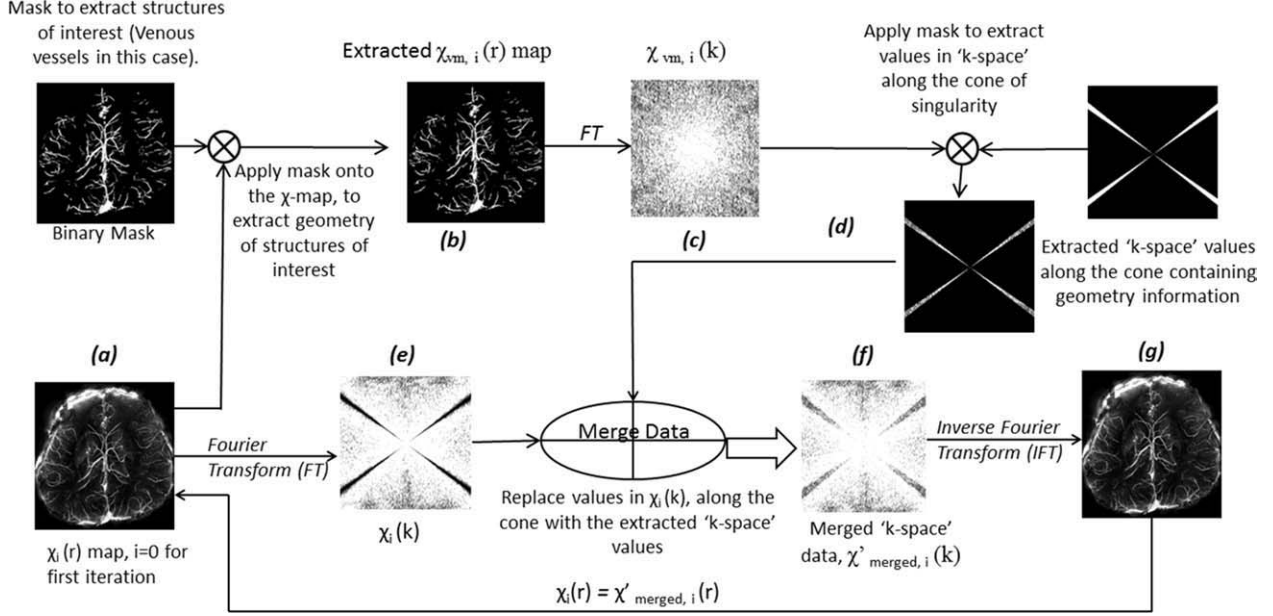


FIG. 1. Illustration of the iterative reconstruction algorithm to obtain artifact free $\chi(r)$ maps.

leads to severe artifacts (including severe streaking) in $\chi(k)$ and noise amplification (29). Thus, for a proper pixel-by-pixel reconstruction of $\chi(r)$, recovering the correct values of $\chi(k)$ near the region of singularities is critical.

K-space Iterative Approach

If the shapes of the structures of interest are known, then one can use this information in the SM to create a more accurate k-space of said SM in the conical region. The structure of the vessels is obtained directly from the first pass SM $\chi_{i=0}(r)$. The detailed steps of the iterative method are discussed below and shown in Fig. 1.

- **Step-1:** An initial estimate of the SM, $\chi_{i=0}(r)$, is obtained by applying a regularized version of the threshold-based inverse filter, $g_{reg}^{-1}(k)$ (18), in Eq. 1 using the suggested threshold value, $thr = 0.1$. The subscript “ i ” denotes the SM after the i th iteration (“ $i = 0$ ” denotes the initial step before doing the iterative method and $i = 1$ for the first iteration).
- **Step-2:** The geometry of the structures of interest is extracted from $\chi_{i=0}(r)$ using a binary vessel mask, i.e. outside the veins, the signal in the mask is set to zero, and inside it is set to unity. Since streaking artifacts associated with veins in the SM are usually outside the vessels, after multiplying the $\chi_i(r)$ map by the mask, little streaking remains in the SM. This leads to $\chi_{vm,i}(r)$ as shown in Fig. 1b. Vessel mask generation will be addressed in the next section.
- **Step-3:** $\chi_{vm,i}(k)$ is obtained by Fourier transformation of $\chi_{vm,i}(r)$ (Fig. 1c).
- **Step-4:** The predefined ill-posed region of k-space in $\chi_{vm,i}(k)$ is extracted (Fig. 1d). These extracted k-space data are denoted by $\chi_{vm,cone,i}(k)$. The size of $\chi_{vm,cone,i}(k)$ is decided by a threshold value, a , which is assigned to $g(k)$. For the matrix size 512×512 , the percentages of the cone region in

k-space for a given a , are 2.4% ($a = 0.01$), 24.1% ($a = 0.1$), 47.1% ($a = 0.2$), and 70.6% ($a = 0.3$), respectively. When a increases, the size of $\chi_{vm,cone,i}(k)$ increases too. If a is increased too much then most of the original information will be lost.

- **Step-5:** Data from $\chi_{vm,cone,i}(k)$ and $\chi_{i=0}(k)$ (Fig. 1e) are merged. This means part of $\chi_{i=0}(k)$ has been replaced by $\chi_{vm,cone,i}(k)$. The merged data are denoted by $\chi'_{merged,i}(k)$ (Fig. 1f).
- **Step-6:** Inverse Fourier transformation of $\chi'_{merged,i}(k)$ gives the improved SM, $\chi_{i+1}(r)$ (Fig. 1g).
- **Step-7:** $\chi_i(r)$ in step-1 is replaced by $\chi_{i+1}(r)$ from step-6 and the algorithm is repeated until

$$\sqrt{\sum [(\chi_i(r) - \chi_{i+1}(r))^2] / N} < \epsilon \quad [3]$$

where N is the number of pixels in $\chi_i(r)$ and ϵ is the tolerance value (chosen here to be 0.004 ppm).

Binary Vessel Mask Generation

The binary vessel mask was generated using thresholding from the $\chi(r)$ map itself. The detailed steps are discussed below and shown in Fig. 2.

- **Step-1:** A threshold, th_1 , is applied to $\chi_{i=0}(r)$ to create an initial binary vessel mask, M_0 . The pixels whose susceptibility values are lower than th_1 will be set to zero while those greater than or equal to th_1 will be set to unity. In this study, a relatively low susceptibility of 0.07 ppm is used for th_1 to capture most vessels. However, this choice of threshold inevitably includes other brain structures in M_0 that have high susceptibility.
- **Step-2:** A morphological closing operation is performed to fill in holes in M_0 to generate an updated mask M_1 .

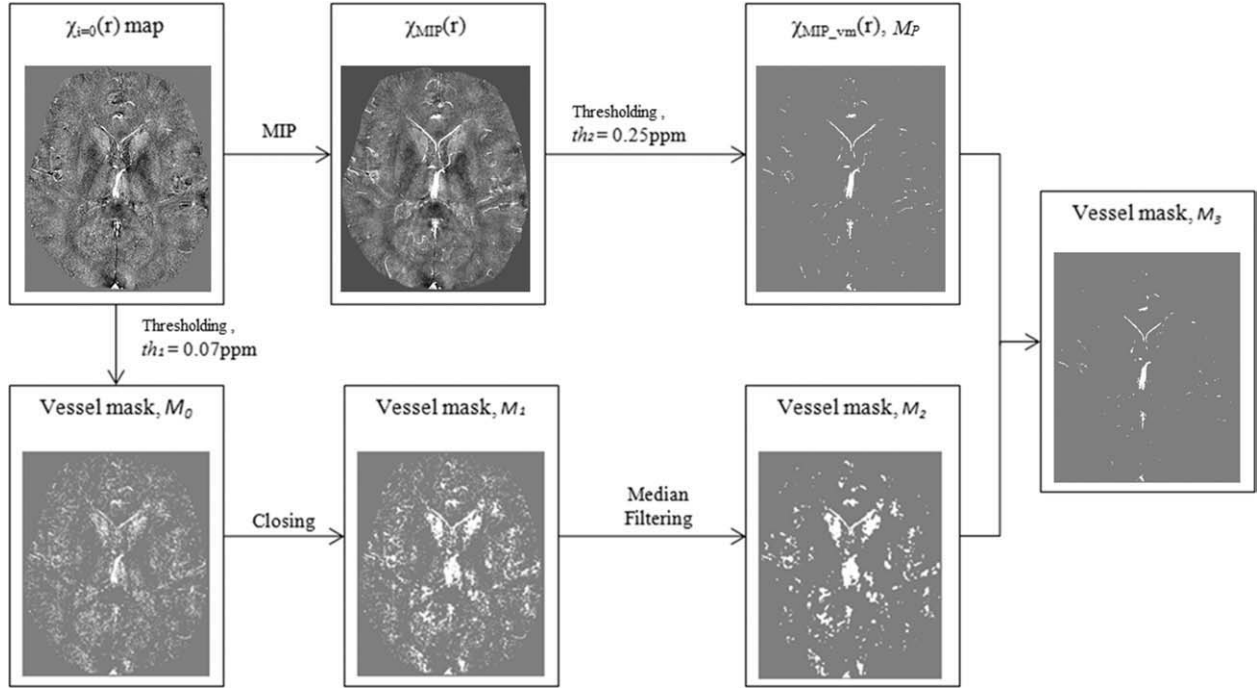


FIG. 2. Illustration of the binary vessel mask generation process.

- **Step-3:** A median filter is applied to remove noise in M_1 and create M_2 .
- **Step-4:** False positive data points from M_2 are removed as follows: First, the $\chi(r)$ map is Mipped over five slices centered about the slice of interest to better obtain contiguous vessel information, as seen in $\chi_{MIP}(r)$. Second, another threshold, $th_2 = 0.25$ ppm, is performed on $\chi_{MIP}(r)$ to create a new $\chi_{MIP_vm}(r)$ and binary mask M_P , which only contains predominantly vessels. Here, 0.25 ppm was chosen to isolate the major vessels in the MIP image. Third, each slice from M_2 is compared with M_P on a pixel-by-pixel basis to create M_3 . If a data point from M_2 does not appear on M_P , this data point will be treated as a false positive and removed from M_2 , otherwise this point is retained. This process can be equally well applied to extract other tissues by choosing appropriate values for th_1 and th_2 .

2D Cylinder Simulations

Simulation of a two dimensional cylinder and its induced phase was first performed using a 8192×8192 matrix. A lower resolution complex image was then obtained by taking the Fourier transform of this matrix and applying an inverse Fourier transform of the central 512×512 matrix in k-space. This procedure is to simulate Gibbs ringing effects caused by finite sampling which we usually see in conventionally required MR data sets. Gibbs ringing comes from discontinuities in both the magnitude and phase images. To avoid Gibbs ringing from magnitude discontinuities, we used a magnitude image with a uniform signal of unity. Cylinders with diameters 32, 64, 128, 256, 512, and 1024 were simulated on 8192×8192 matrices and their effective

diameters were 2, 4, 8, 16, 32, and 64 on 512×512 matrices. All phase simulations were performed using a forward method (8,26,27,30) with $B_0 = 3$ T, $\Delta\chi = 0.45$ ppm in SI units, $T_E = 5$ ms, and the cylinder perpendicular to the main magnetic field. The susceptibility value of 0.45 ppm represents venous blood when the hematocrit (Hct) = 0.44, $\Delta\chi_{do} = 4\pi \cdot 0.27$ ppm (31) and the oxygen saturation level = 70%, where $\Delta\chi_{do}$ is the susceptibility difference between fully deoxygenated and fully oxygenated blood (32). A relatively short echo time was chosen to avoid phase aliasing that can affect the estimated susceptibility values.

Selection of a TBSO Method to Generate the $\chi_{i=0}(r)$ Map

TBSO methods (11,15,18,24) use a truncated $g(k)$ to solve the singularity problem in the inverse filter $g^{-1}(k)$ when $g(k)$ is less than a predetermined threshold value, thr. When $g(k) < thr$, $g^{-1}(k)$ is either set to zero (11,24); or to $1/thr$ (15); or set to $g^{-1}(k) = 1/thr$ first and then $g^{-1}(k)$ is brought smoothly to zero as k approaches k_{zo} . This smoothing is accomplished by multiplying $g^{-1}(k)$ by $\alpha^2(k_z)$ with $\alpha(k_z) = (k_z - k_{zo})/|k_{zthr} - k_{zo}|$ where k_z is the z component of that particular point in k-space, k_{zo} is the point at which the function $g^{-1}(k)$ becomes undefined, and k_{zthr} is the k_z coordinate value where $|g(k)| = thr$ (18).

SMs using the methods in Refs. 11,15,18 were calculated based on Eq. 1 using the 2D cylindrical model. Equation 1 can be used to calculate the SM for the simulated 2D cylinder model perpendicular to the main field since the 2D perpendicular model is a special case of the 3D model with 1 slice [10]. Streaking artifacts are obvious in all three SMs (figures are not shown). The calculated mean susceptibility values inside the cylinder

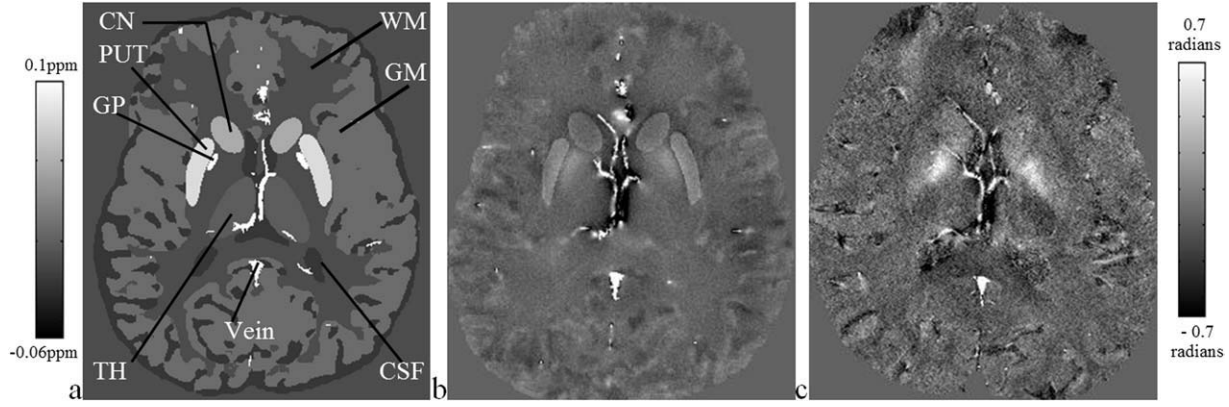


FIG. 3. **a:** A transverse view of the 3D brain model. **b:** The simulated phase map from the model using parameters: $B_0 = 3$ T and $T_E = 18$ ms which are consistent with imaging parameters in the real data **(c)**. Images **(b)** and **(c)** have the same window level setting.

are around 0.40 ± 0.01 ppm for all SMs. The background noise levels, (i.e., standard deviation of the susceptibility values) measured from a region outside the streaking artifact in SM using Ref. 18 are around 1/2 to 2/3 of the background noise levels in SMs using Refs. 11,15 with $\text{thr} = 0.06, 0.07$, and 0.1 , which are the optimal threshold values suggested in Refs. 11,12,18. Given this result, the method in (18) was chosen to generate a $\chi_{i=0}(r)$ map.

Finding an Optimal Threshold Value

To find the optimal threshold, a series of $\chi(r)$ maps were reconstructed by the iterative method using threshold values a of $0.01, 0.03, 0.07, 0.1, 0.15, 0.2, 0.25$, and 0.3 . The larger this threshold, the closer the final estimate for $\chi(r)$ will be to $\chi_{\text{vm}}(r)$. The optimal threshold value was found by comparing the accuracy of the estimated susceptibility values as well as the effects on reducing streaking artifacts in the reconstructed $\chi(r)$ maps. To study the effect of noise in $\chi(r)$ maps due to the noise in phase images, complex datasets for cylinders of diameter 2, 4, 8, 32 voxels, respectively, were simulated with Gaussian noise added to both real and imaginary channels. Noise was added in the complex images to simulate a $\text{SNR}_{\text{magnitude}}$ of 40:1, 20:1, 10:1, and 5:1 in the magnitude images. Since $\sigma_{\text{phase}} = 1/\text{SNR}_{\text{magnitude}}$, this corresponds to $\sigma_{\text{phase}} = 0.025, 0.05, 0.1$, and 0.2 radian.

To estimate the improvement in the SM by the iterative method, we used a root mean squared error (RMSE) to measure streaking artifacts outside the cylinder. Background noise in the SM is measured in a region away from all major sources of streaking artifacts to compare the noise measured in the phase image (i.e., so we can correlate noise in the phase with the expected noise enhancement from the inversion process).

Effect of High-Pass Filter

The effect of high-pass (HP) filtering the phase data on the $\chi(r)$ map generated by the iterative method was also studied. Phase images of a cylindrical geometry with diameters of 2, 4, 8, 16, 32, and 64 voxels were simulated. Homodyne HP filters (33) with a 2D hanning filter (full width at half-maximum, FWHM = 4, 8, 16, and 32 pixels) were applied on these phase images in both in-

plane directions. SM reconstructions were stopped based on the criteria in step 7 of the iterative process.

Three Dimensional Brain Model Simulations

To address the potential of the iterative technique to improve the SM of general structures such as the basal ganglia, a 3D model of the brain was created including the: red nucleus (RN), substantia nigra (SN), crus cerebri (CC), thalamus (TH), caudate nucleus (CN), putamen (PUT), globus pallidus (GP), gray matter (GM), white matter (WM), cerebrospinal fluid (CSF), and the major vessels (34). The structures in the 3D brain model were extracted from two human 3D T_1 weighted and T_2 weighted data sets. Basal ganglia and vessels are from one person; GM and WM are from the other person's data set. Since all structures are from in vivo human data sets, this brain model represents realistic shapes and positions of the structures in the brain. Susceptibility values in parts per million (ppm) for the structures SN, RN, PUT, and GP, were taken from Ref. 12 and others were from measuring the mean susceptibility value in a particular region from SMs using Ref. 18 from in vivo human data: RN = 0.13, SN = 0.16, CC = -0.03, TH = 0.01, CN = 0.06, PUT = 0.09, GP = 0.18, vessels = 0.45, GM = 0.02, CSF = -0.014, and WM = 0. All structures were set inside a $512 \times 512 \times 256$ matrix of zeros. The phase of the 3D brain model was created by applying the forward method (8,26,27,30) to the 3D brain model with different susceptibility distributions using the imaging parameters: $T_E = 5$ ms and $B_0 = 3$ T. A comparison between the phase maps from this brain model and a real data set is shown in Fig. 3. To match the imaging parameters of the real data set, $B_0 = 3$ T and $T_E = 18$ ms were applied for the results presented in Fig. 3. Except for Fig. 3, all other figures in the paper associated with the 3D brain were simulated by using $T_E = 5$ ms.

In Vivo MR Data Collection and Processing

A standard high-resolution 3D gradient echo SWI sequence was used for data acquisition. A transverse 0.5 mm isotropic resolution brain dataset was collected at 3 T from a 23-year-old healthy volunteer. The sequence parameters were: TR = 26 ms, flip angle = 15° , read

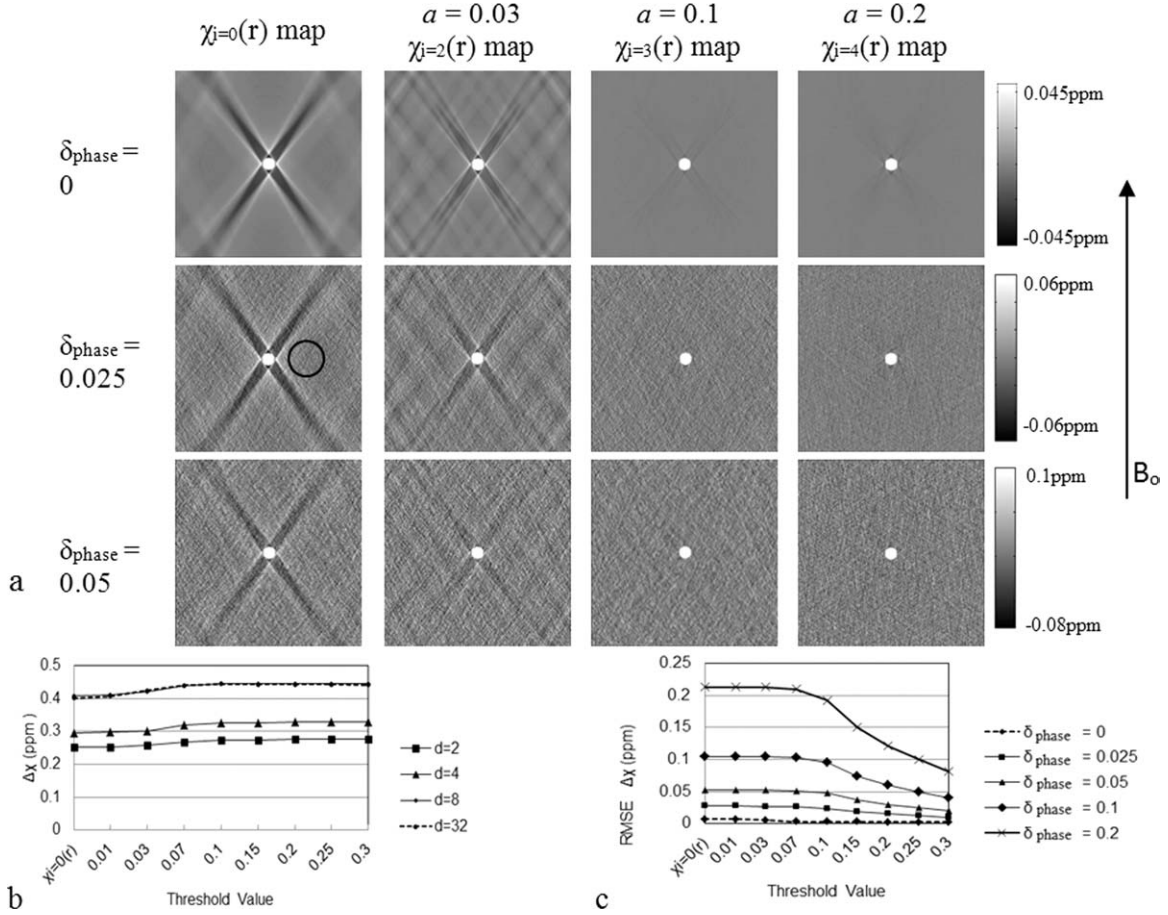


FIG. 4. Simulations showing the comparison of the calculated susceptibility distributions for a cylinder perpendicular to B_0 at different threshold values (a) applied to $g(k)$ as well as the initial $\chi_{i=0}(r)$ map. The direction of B_0 is indicated by a black long arrow. The susceptibility, $\Delta\chi$, inside the cylinder is 0.45 ppm. **a:** The comparison of the converged $\chi_{i=b}(r)$ map with the $\chi_{i=0}(r)$ map for a diameter of 32-pixel cylinder, where b is the iterative step required to reach convergence. In this data, $b = 2$ when $a = 0.03$, $b = 3$ when $a = 0.1$ and $b = 4$ when $a = 0.2$ when $\sigma_{\text{phase}} = 0$. The top row of images shows simulations with no phase noise. The second and the third row show simulations with added phase noises $\sigma_{\text{phase}} = 0.025$ and 0.05 radian, respectively. The first column of images show initial $\chi_{i=0}(r)$ maps for reference. **b:** The variation of the mean calculated susceptibility inside the cylinder with different threshold value, a , for diameter (d) = 2, 4, 8, and 32 pixels cylinders. The mean susceptibility value is independent of the noise level; therefore, only mean values from $\sigma_{\text{phase}} = 0$ were provided. **c:** The variation of the RMSE of the susceptibility values outside the cylinder as a function of the threshold value, a , and the noise level. The $d = 32$ pixels cylinder was used to generate (c). The range of the gray-scale bars is chosen to highlight the artifacts in the images. It does not reflect the quantified higher susceptibility values inside cylinders.

bandwidth = 121 Hz/pixel, $T_E = 14.3$ ms, 192 slices, and a matrix size of 512×368 . To reconstruct $\chi_{i=0}(r)$ with minimal artifacts, the following steps were carried out:

1. The unwanted background phase variations were removed using either: (a) a homodyne HP filter (FWHM = 16 pixels) (33) or (b) Prelude in FMRIB Software Library (FSL) (35) to unwrap the phase, followed by the process of Sophisticated Harmonic Artifact Reduction for Phase data (SHARP) (36) with a filter radius of 6 pixels. To reduce artifacts in the calculated SMs, regions with the highest phase deviations due to air/tissue interfaces were removed manually from the HP filtered phase images and the phase in those regions were set to zero.
2. A complex threshold approach (37) was used to separate the brain from the skull.
3. The phase image with an original matrix size of $512 \times 368 \times 192$ was zero filled to $512 \times 512 \times 256$ to

increase the field-of-view and to avoid streaking artifacts caused by the edge of brain to alias back to the reconstructed SM.

4. The regularized inverse filter, $g_{\text{reg}}^{-1}(k)$ (18) was applied to obtain $\chi_{i=0}(r)$, followed by the iterative process using $a = 0.1$. For in vivo data, the iterative program was terminated at the third iterative step.

RESULTS

Selection of Threshold Level Based on Simulations

To find the optimal threshold value, SMs were reconstructed using $a = 0.01, 0.03, 0.07, 0.1, 0.15, 0.2, 0.25$, and 0.3 , respectively, with different noise levels (Fig. 4). The streaking artifacts shown in $\chi_{i=0}(r)$ (the first column in Fig. 4a) have been significantly reduced by the iterative method and fall below the noise level when $a \geq 0.1$. Also, when $a \geq 0.1$, the mean susceptibility value

inside the cylinder was found to increase to 0.44 ppm when the diameter of the cylinder was larger than 8 pixels (Fig. 4b) and this trend is independent of the object size and the noise in the phase image. The optimal result in terms of obtaining the true susceptibility value was with a threshold of 0.1. Figure 4c shows a plot of RMSE of the susceptibility values from the whole region outside the 32-pixel cylinder using different a . The RMSE of the susceptibility values decreases as a increases. Therefore, for vessels, a value of $a = 0.3$ would be the optimal value. However, a large threshold value means replacing more original k-space with the k-space only consisting of vessel information which will reduce the signals from other brain structures and blur these structures. Since the SM using $a = 0.1$ already reveals the optimal susceptibility value for the vessels and an acceptable RMSE, it is appropriate to choose 0.1 for more general applications to study the entire brain.

Figure 4a compares the converged $\chi_{i=b}(r)$ map with the $\chi_{i=0}(r)$ map, where b is the iterative step required to reach convergence. In this data, $b = 2$ when $a = 0.01$ and 0.03 , $b = 3$ when $a = 0.07$, 0.1 , and 0.15 and $b = 4$ when $a = 0.2$, 0.25 , and 0.3 for $\sigma_{\text{phase}} = 0$. When σ_{phase} increases, more iterative steps were required to reach convergence. For instance, the maximum iterative step number is 9 when $\sigma_{\text{phase}} = 0.2$ radians. Using a noise level of 0.025 radian in the phase image as an example, $g_{\text{reg}}^{-1}(k)$ (18) leads to a susceptibility noise of roughly 0.025 ppm in the $\chi_{i=0}(r)$ map. The iterative approach leads to a slight decrease in background noise, 0.021 ppm, in $\chi_{i=3}(r)$ map when $a = 0.1$. The background noise was measured in a region outside the streaking artifact indicated by the black circle in Fig. 4a. The overall decrease in RMSE in the background (Fig. 4c) is a consequence of both a decrease in streaking artifacts and a reduction in thermal noise contribution.

Selection of the Optimal Iterative Step

The inverse process (18) was applied to the dipole field in Fig. 5a to give the $\chi_{i=0}(r)$ map shown in Fig. 5b; prominent streaking artifacts are evident in this image. Streaking artifacts are significantly reduced at each step of the iterative method quickly reaching convergence (Fig. 5c–e). The largest improvement is seen in the first iterative step, which is verified by Fig. 5f, showing the difference between Fig. 5c ($\chi_{i=1}(r)$ map) and Fig. 5b ($\chi_{i=0}(r)$ map). After the second iteration, we can see some minor streaking reductions (Fig. 5g, the difference between the $\chi_{i=1}(r)$ map and $\chi_{i=2}(r)$ map). The mean susceptibility value approaches 0.44 ppm in a single step. Similar results (not shown) are also obtained when the iterative method is run with different aspect ratios between the in-plane resolution and the through plane resolution (such as 1:2 and 1:4). The iterative results always lead to higher final susceptibility values compared to the initial value in $\chi_{i=0}(r)$. Finally, even when an HP filter is applied, up to a 10% increase in the susceptibility is realized (Fig. 5i). The SMs of large vessels benefit from a low order HP filter (FWHM = 4 pixels) and small vessels up to 8 pixels benefit from a HP filter (FWHM = 16 pixels).

Effect of the Iterative Approach on Surrounding Brain Tissues in the 3D Brain Model

SM Reconstruction Using a Vessel Mask Only

Figure 6a,d represents $\chi_{i=0}(r)$, without noise and with 0.025 radians of noise in phase images. Figure 6f is the vessel map. Streaking artifacts (delineated by the black arrows) are obvious in Fig. 6a,d and significantly reduced in the $\chi_{i=3}(r)$ maps (Fig. 6b,e) using $a = 0.1$. Figure 6c is the $\chi_{i=3}(r)$ map using $a = 0.2$. As can be seen, when a increases, the iterative method still works for vessels, but brain tissues become more blurred. Figure 7a plots the mean susceptibility values inside the vessel (vein of Galen), GP, SN, RN, PUT, and CN from $\chi_{i=3}(r)$ maps generated by using $a = 0.1, 0.15, 0.2, 0.25$, and 0.3 , respectively. The susceptibility value in the brain model and $\chi_{i=0}(r)$ map are also provided in the plot as references. Generally, the susceptibility values of brain tissues except vessels decrease as a increases while, for vessels, the susceptibility value is 0.41 ppm in the $\chi_{i=0}(r)$ map and is increased to 0.45 ppm in the $\chi_{i=3}(r)$ maps.

SM Reconstruction Using a Mask Including Vessels and Brain Structures

The iterative method is not limited to improving SM from just vessels; it can also be applied to the entire brain. Figure 6g shows a coronal view of the $\chi_{i=0}(r)$ map for the brain model. The $\chi_{i=3}(r)$ map using a mask keeping all major structures (GP, SN, RN, PUT, CN) and vessels is shown in Fig. 6h. In practice, this is equivalent to setting thresholds in the $\chi_{i=0}(r)$ map to be greater than 0.09 ppm to extract all these high susceptibility structures from the $\chi_{i=0}(r)$ map to create the mask. Figure 6h reveals that streaking artifacts associated with veins as well as all major structures have been reduced. Figure 6i shows the difference between Fig. 6g, h. In addition, streaking artifacts sometimes cause the appearance of “false” structures. For instance, there is no internal capsule (IC) included in the model (Fig. 6l), yet we see an IC like structure in the $\chi_{i=0}(r)$ map (Fig. 6j) (indicated by a dashed white arrow in Fig. 6j). The iterative method removes the streaking artifacts and the “false” IC (Fig. 6k). Figure 7b shows susceptibility values in each structure in the brain model for $\chi_{i=0}(r)$ and $\chi_{i=3}(r)$ when the mask includes vessels and all major structures. The underestimated susceptibility values of all major structures and vessels in the $\chi_{i=0}(r)$ map have been recovered by the iterative method in the $\chi_{i=3}(r)$ map.

Effect of Errors in the Vessel Map

Accurately extracting vessels from $\chi_{i=0}(r)$ is critical for the iterative method. Figure 8b–d and the corresponding enlarged views (Fig. 8f–h) from the rectangular region indicated in Fig. 8a show the $\chi_{i=3}(r)$ maps using an accurate (Fig. 8j), a dilated (Fig. 8k), and an eroded (Fig. 8l) vessel map to show the effect of errors in the vessel mask on the $\chi_{i=3}(r)$ map. The dilated and eroded vessel maps were generated using Matlab functions based on a 3-by-3 square structuring element object. The susceptibility values measured from a vein indicated by the white arrow in Fig. 8e are 0.40 ± 0.03 ppm (Fig. 8e),

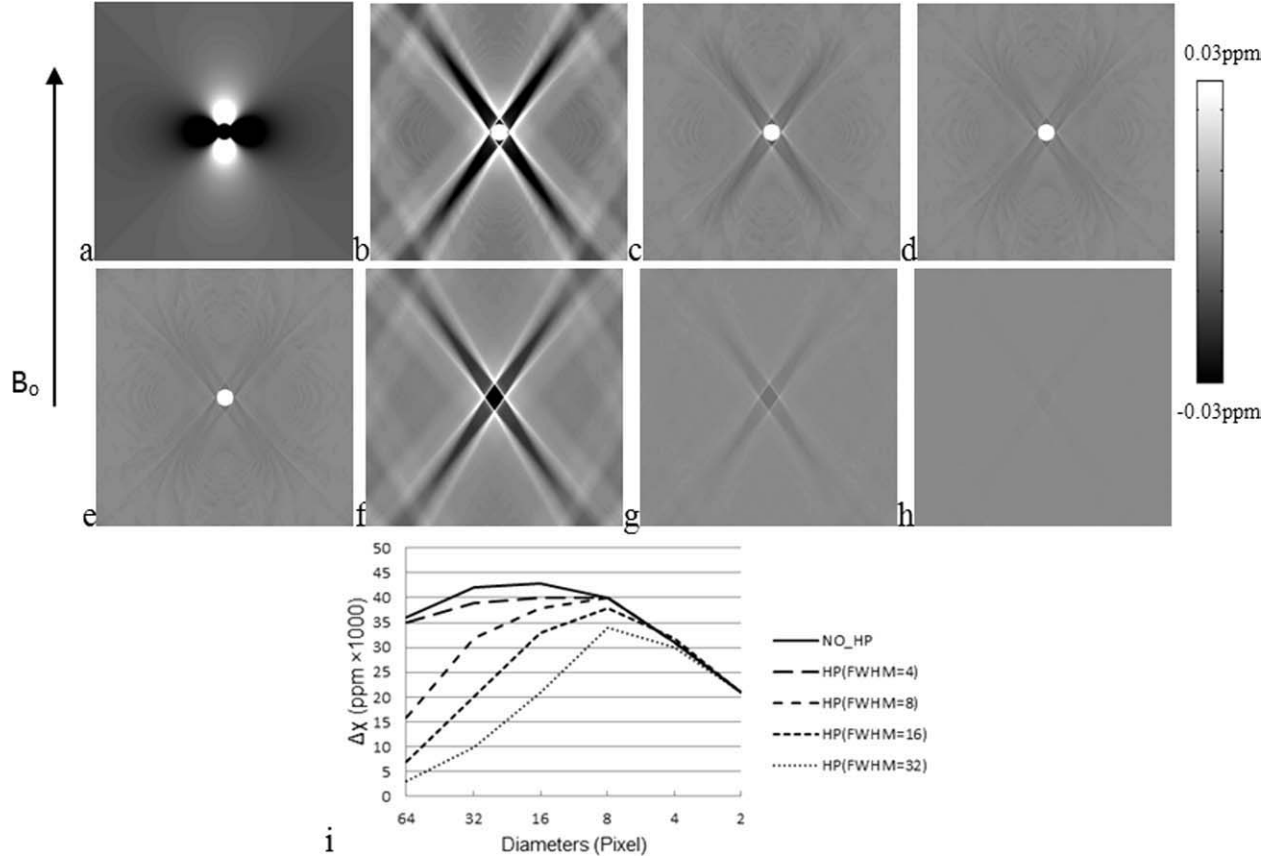


FIG. 5. **a**: Phase images from a cylinder with a diameter of 32 pixels are simulated with: $\Delta\chi = 0.45$ ppm, $B_0 = 3$ T, and $T_E = 5$ ms. The cylinder is perpendicular to the main field. No thermal noise was added in these images. **b**: The initial $\chi_{i=0}(r)$ map. **c**: The SM from the first iteration, $\chi_{i=1}(r)$ map, **(d)** $\chi_{i=2}(r)$ map and **(e)** $\chi_{i=3}(r)$ map using threshold value $\alpha = 0.1$. The SM has converged at $\chi_{i=3}(r)$ map. The streaking artifacts are reduced as the number of iterative steps increases. **f**: The difference image of (c) subtracted from (b) illustrates that the streaking artifacts were reduced by the iterative procedure and the largest improvement happens in this first iterative step. **g**: The difference image of the $\chi_{i=1}(r)$ map subtracted from the $\chi_{i=2}(r)$ map indicates that the streaking artifacts were further reduced by the second iterative step. **h**: The difference image of $\chi_{i=2}(r)$ map subtracted from $\chi_{i=3}(r)$ map shows much less improvement at the third iterative step. Thus it indicates a convergence of the iterative procedure. All images were set to the same window level setting for direct comparisons and for enhancing the presence of the streaking and the remnant error. **i**: The effect of the iterative approach on the changes in susceptibility values from HP filtered phase images. Differences between the values in iterative and non-iterative susceptibility map reconstruction (i.e., $\chi_{i=3}(r) - \chi_{i=0}(r)$) from HP filtered phase images are plotted for different filter sizes. Results for four filter sizes (FWHM = 4, 8, 16, and 32 pixels) are shown here. Applying an HP filter leads to an underestimation of $\Delta\chi$ (18). The iterative approach helps to improve the accuracy of the estimated susceptibility values. The range of the gray-scale bars is chosen to highlight the artifacts in the images. It does not reflect the quantified higher susceptibility values inside cylinders.

0.45 ± 0.03 ppm (Fig. 8f), 0.45 ± 0.03 ppm (Fig. 8g), and 0.40 ± 0.07 ppm (Fig. 8h), respectively. The iterative method still works if the vessel is slightly enlarged but does little to change the original $\chi_{i=0}(r)$ map if the vessels are too small or absent in the mask. As we just discussed, streaking artifacts produced “false” vessels indicated by the dashed black arrow in Fig. 8e since these vessels are not in the model (Fig. 8i). These false vessels disappeared in Fig. 8f.

Results from the In Vivo Dataset

In the in vivo example, we compare the differences between SHARP (Fig. 9a–d) and a homodyne HP filter (FWHM = 16 pixels) (Fig. 9e–h). Compared to the transverse view, streaking artifacts are more obvious in the sagittal or coronal view. Figure 9a shows the $\chi_{i=0}(r)$ map with severe streaking artifacts. The streaking artifacts

were significantly reduced in the $\chi_{i=3}(r)$ map (Fig. 9b) using $\alpha = 0.1$. The streaking artifacts associated with the superior sagittal sinus vein (indicated by two black arrows in Fig. 9a) were significantly decreased in Fig. 9b,d. The subtracted image (Fig. 9c), Fig. 9a minus Fig. 9b, reveals the removed streaking artifacts. These streaking artifacts are one of the reasons why the $\chi_{i=0}(r)$ maps appear noisy. In the $\chi_{i=3}(r)$ map, the reduction in streaking artifacts from individual veins leads to a decrease of noise therefore an increased SNR of veins. If veins are the only interest, even a threshold of 0.2 can work reasonably well (Fig. 9d). Two relatively big veins, V1 and V2, indicated by the white dashed and white solid arrows, respectively, in Fig. 9b, were chosen to measure the susceptibility values. Results are provided in Table 1. The susceptibility values of these two veins have been improved by roughly 16% by the iterative method. The standard deviation of the susceptibility values measured

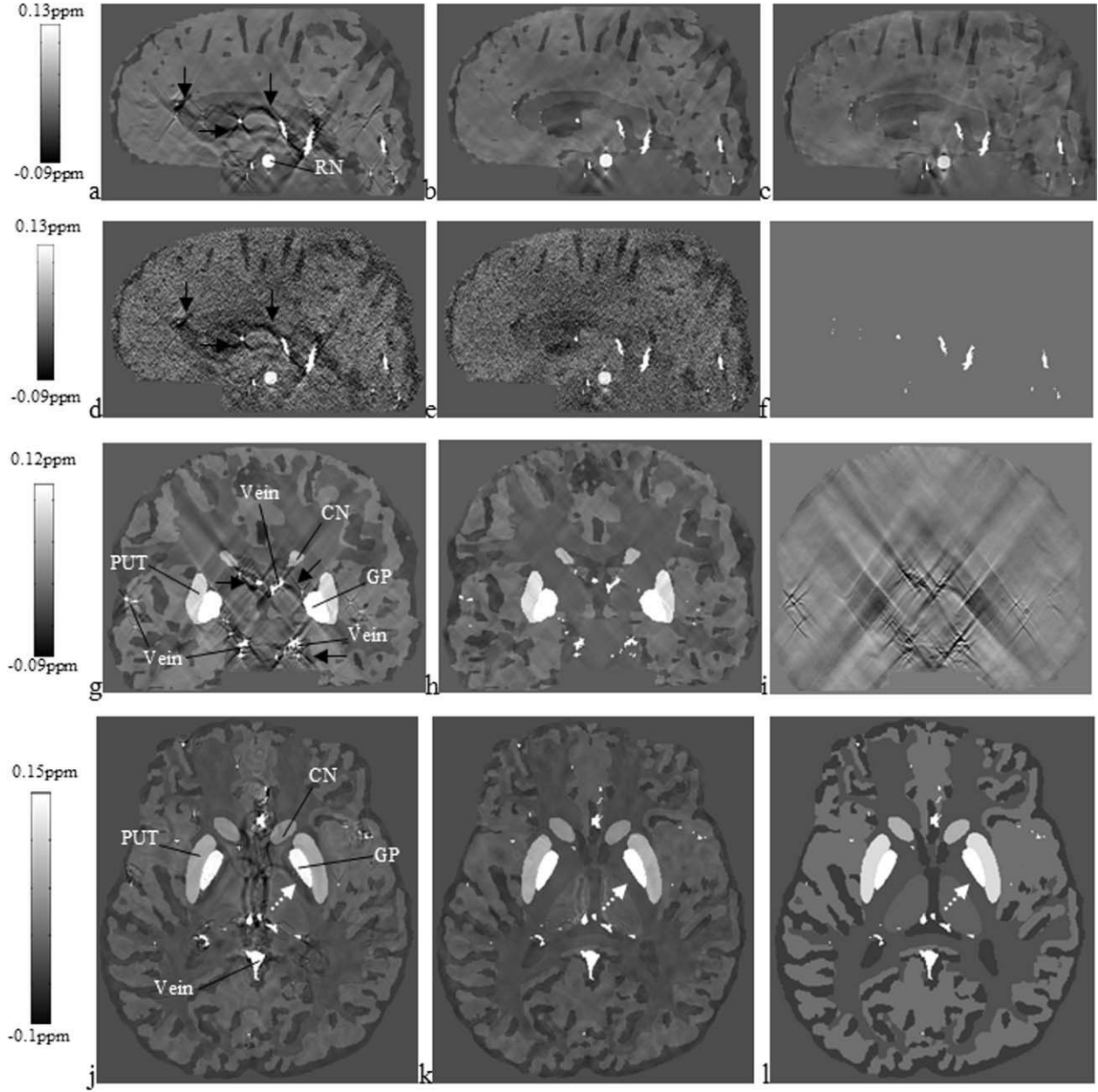


FIG. 6. Results before and after the iterative method using a region of interest map which consists of either only vessels or specific brain structures (in this case the basal ganglia) plus vessels. **a**: The initial $\chi_{i=0}(r)$ map without noise added in the original simulated images. **b**: $\chi_{i=3}(r)$ map of (a) using threshold value $\alpha = 0.1$. **c**: Similar to (b), $\alpha = 0.2$. **d**: The initial $\chi_{i=0}(r)$ map with noise added in original images, resulting a standard deviation of 0.025 radian in phase images. **e**: $\chi_{i=3}(r)$ map of (d) using $\alpha = 0.1$. **f**: The associated vessel map. **g**: The $\chi_{i=0}(r)$ map in the coronal plane as a reference. The streaking artifacts are clearly shown in every structure. **h**: The $\chi_{i=3}(r)$ maps created by using a region of interest map which consists of GP, SN, RN, PUT, CN, and vessels. **i**: The difference image of (g) and (h). **j**: The initial $\chi_{i=0}(r)$ map in the transverse plane has “false” internal capsule (IC) (pointed by an arrow) around GP; **k**: The $\chi_{i=3}(r)$ map shows no “IC.” This matches the originally simulated model (l). No noises were added to images from (g) to (l).

from a uniform region inside the WM decreased from 0.042 ppm in $\chi_{i=0}(r)$ map to 0.035 ppm and 0.023 ppm in the $\chi_{i=3}(r)$ map with $\alpha = 0.1$ and 0.2, respectively. The baseline susceptibilities of the major structures are higher with SHARP than with the HP filter. The iterative method works for brain structures too when the structure is included in the mask. For instance, the mean susceptibility values of the GP and SN have been increased from 0.155 ± 0.058 ppm and 0.162 ± 0.067 ppm in the $\chi_{i=0}(r)$

map to 0.163 ± 0.070 ppm and 0.186 ± 0.083 ppm in the $\chi_{i=3}(r)$ map, from the dataset processed using SHARP. The result after HP filtering (Fig. 9e) shows more edge artifacts indicated by the left arrow in Fig. 9e. Much of this error was reduced by the iterative method (Fig. 9f). It seems that the iterative method compensated for the worse first guess (Fig. 9e) and ended up with almost the same result (Fig. 9f,h) as having started with SHARP (Fig. 9b,d) from the image perspective. Since a

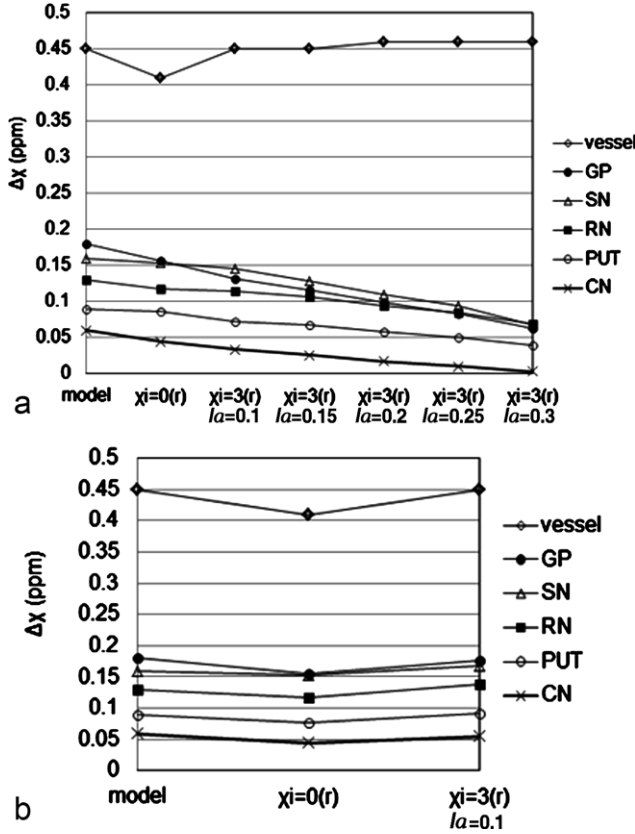


FIG. 7. The plots of mean susceptibility values inside the vessel (vein of Galen), GP, SN, RN, PUT, and CN from $\chi_{i=3}(r)$ maps. The first two data points of each curve is the value inside each structure from the brain model and the $\chi_{i=0}(r)$ map, respectively. **a:** $\chi_{i=3}(r)$ maps generated by applying a region of interest map which consists only vessels using $\alpha = 0.1, 0.15, 0.2, 0.25$, and 0.3 , respectively. **b:** $\chi_{i=3}(r)$ maps generated by applying a region of interest map which consists of the GP, SN, RN, PUT, CN, and vessels using $\alpha = 0.1$.

small sized HP filter cannot remove rapid phase wrapping at air-tissue interfaces; we had to cut out the region near the sinuses in the phase images.

DISCUSSION

In this article, a threshold-based k-space/image domain iterative approach has been presented. Simulations and in vivo results show that the ill-posed problems of streaking artifacts and biases in the estimates of susceptibilities can be significantly reduced. The replacement of the $\chi(k)$ values near the singularities by $\chi_{vm}(k)$, which is obtained from the geometric information from the $\chi(r)$ map itself, obviates many of the current problems seen in the TBSO methods. Since $\chi_{vm}(r)$ contains little streaking artifacts itself, the values used inside the thresholded regions in $\chi(k)$ now contain no artifact either. In this sense, we obtain an almost perfect k-space without bad data points in the region of singularities. This explains why this method converges quickly and the major improvement is in the first iterative step (Fig. 5).

The proposed iterative approach is different from the other threshold-based methods (11,15,18,19,24) which fill a predefined conical region using a constant, zero or 1/thr threshold (11,15,24) or the first-order derivative of $g^{-1}(k)$ (19). The iterative method uses full geometry information from the SM (vessels or predefined structures and not edge information) to iteratively change k-space values in the conical region using the forward model. This is also quite different than other currently proposed solutions (9,12,20,22). Even though spatial priors such as gradients of the magnitude are used (9,12,20,22), in those methods, the meaningful values of the singularity regions in k-space are obtained through solving the complex cost function problem. However, the iterative method uses priors not from the magnitude image but from the SM. The missing data in the singularity regions are obtained through iterating back and forth between

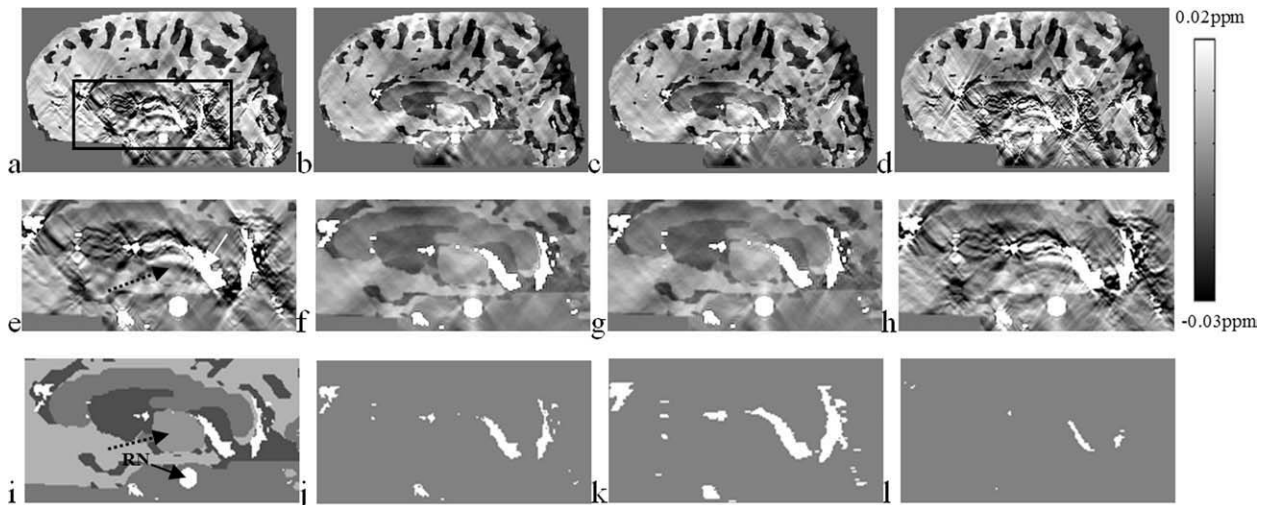


FIG. 8. Comparison of the reconstructed $\chi_{i=3}(r)$ maps using (j) accurate, (k) dilated, and (l) eroded vessel maps. Their corresponding vessel maps and the enlarged views from the rectangular regions are provided in (b)–(d) and (f)–(h). (a) and (e) The initial $\chi_{i=0}(r)$ maps and (i) the original brain model as references. The circle in the midbrain in the $\chi(r)$ maps represents the RN and is indicated by a black arrow in (i). Other hyper-intense regions in SMs are vessels.

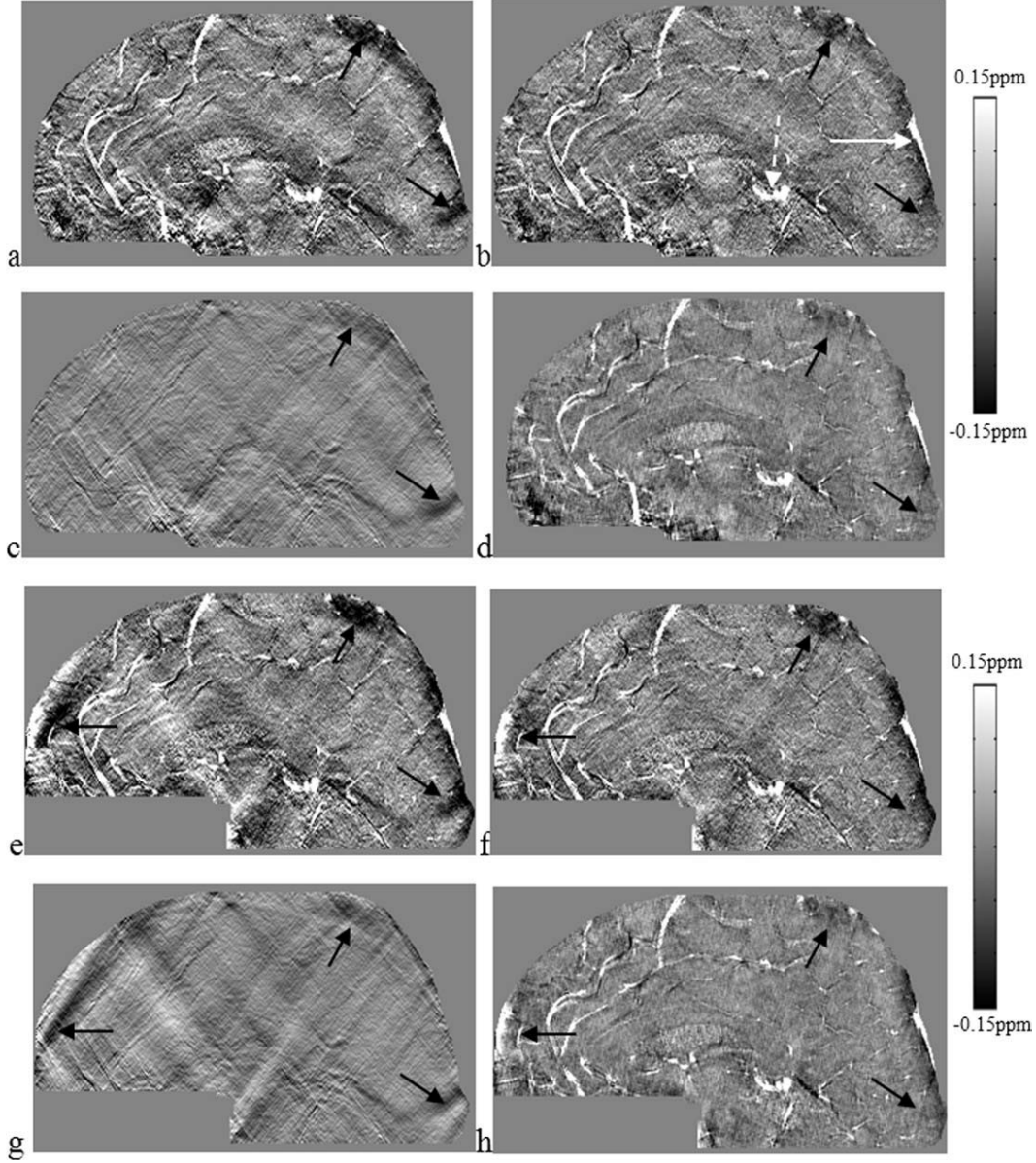


FIG. 9. Comparisons of SMs using SHARP or a HP filter (FWHM = 16 pixels) to remove the background field. The iterative method with $a = 0.1$ and 0.2 is applied after the background is removed. (a)–(d) and (e)–(h) are results after the application of SHARP and the HP filter, respectively. (a) and (e) the initial $\chi_{i=0}(r)$ maps. (b) and (f) the $\chi_{i=3}(r)$ maps generated from the iterative method with $a = 0.1$. (c) and (g) the differences of images between (a) and (b), and between (e) and (f), respectively. These two images show the successful reduction of the streaking artifacts. (d) and (h) the $\chi_{i=3}(r)$ maps generated from the iterative method with $a = 0.2$. The range of the gray-scale bars is chosen to highlight the artifacts in the images. It does not reflect the quantified susceptibility values inside veins.

the SMs and their k-space. The advantage of cost function approaches is that they do not need to predefine the singularity region in k-space which is solved by the optimization process automatically (although the optimization process itself is usually quite time-consuming). On the other hand, the iterative method is the most time-efficient. It is fast enough to reconstruct SMs for a $512 \times 512 \times 256$ data set using an Intel Core i7 CPU 3.4 GHz processor in less than 30 s, since in practice usually three iterations are good enough to generate decent results.

The threshold value also plays a key role. A threshold value of 0.1 is a reasonable choice since a lower threshold value leads to an increase in noise and a higher

threshold value leads to a blurring of the object (Figs. 6c, 9d, h).

It is known that the ill-posedness of the inverse filter will increase the noise level from the phase to the SM. Based on both simulations and real data, we find that there is a factor of 4 increase in noise in the SM relative to the original phase data. This result and the fact at $B_0 = 3$ T, $T_E = 5$ ms, and $\sigma_{\chi_{i=0}(r)} = 0.025$ ppm make it possible to write the total noise in the background region in $\chi_{i=0}(r)$ as $0.025 \cdot 4 \cdot (3/B_0) \cdot (5/T_E)$ in ppm. The noise in $\chi_{i=3}(r)$ will be less than this value since the iterative method will reduce streaking artifact in SM.

The iterative method can be used to remove streaking artifacts associated with not only vessels but also other

Table 1
 $\Delta\chi$ Measured *In Vivo* in Two Veins in $\chi_{i=0}$ (r) Maps and $\chi_{i=3}$ (r) Maps With Different Threshold Values

	$\chi_{i=0}$ (r) map	$\chi_{i=3}$ (r) map/ $a = 0.1$	$\chi_{i=3}$ (r) map/ $a = 0.2$
V1 (SHARP)	0.32 ± 0.07	0.37 ± 0.08	0.38 ± 0.09
V1 (HP)	0.24 ± 0.05	0.28 ± 0.06	0.28 ± 0.06
V2 (SHARP)	0.35 ± 0.04	0.40 ± 0.05	0.41 ± 0.05
V2 (HP)	0.25 ± 0.05	0.31 ± 0.06	0.30 ± 0.06

Mean and standard deviation for the susceptibility values (in ppm) of two veins processed using SHARP and a HP filter (FWHM = 16 pixels), respectively, were chosen from the 0.5 mm isotropic resolution data. V1 and V2 are shown in Fig. 9. The susceptibility values of these two veins have been increased by the iterative method. There is not much variation of the susceptibility value with different threshold values.

brain structures as well. Figure 6h shows a reduction in artifacts associated specifically with iron-rich regions such as the GP and CN.

Accurately extracting vessels from the $\chi_{i=0}(r)$ map is critical for the iterative method (Fig. 8). In this study, vessels were segmented directly from the SM (Fig. 2). It may also possible to segment veins from original magnitude images [9,12,20,22], phase images, and/or SWI images. Extraction of accurate anatomic information from phase data sometimes is difficult since phase is orientation dependent and phase changes are generally nonlocal. SWI images work better for an anisotropic dataset rather than an isotropic dataset since phase cancellation is needed to highlight vessel information. Therefore, we may consider combining SMs with magnitude images, phase images, and/or SWI images together to segment the veins, since different types of images can compensate for missing information.

The iterative method appears to help even in the presence of non-isotropic resolution with partial volume effects and to a minor degree when an HP filter is applied. A smaller sized HP filter would be better, since a larger HP filter will significantly underestimate the susceptibility value (Table 1). SHARP gave us better results compared with the HP filter (FWHM = 16 pixels) (Fig. 9), but SHARP requires phase unwrapping which can be time consuming and is noise dependent [19]. From this perspective, an HP filter has the advantage since it does not need unwrapped phase. If the forward modeling approach of Neelavalli et al. [38] can be used to reduce air/tissue interface fields, then it may be possible to use a small size HP filter (FWHM = 8 pixels) which may provide similar results to SHARP.

Severe streaking artifacts associated with structures having high susceptibility values such as veins can lead to major changes in the appearance of the brain structures with low susceptibility. Practically, the susceptibility of the veins is a factor of 2.5–20 times higher than other structures in the brain. Therefore, even a 10% streaking artifact can overwhelm the information in the rest of the brain and create false appearing structures as in (Fig. 6j) and in (Fig. 8e). The reduction of these artifacts makes a dramatic difference in the ability to properly extract the susceptibility of other tissues.

In conclusion, both simulations and human studies have demonstrated that the proposed iterative approach can dramatically reduce streaking artifacts and improve the accuracy of susceptibility quantification inside the structures of interest such as veins or other brain tissues. Given its relatively fast processing time, it should be possible to expand its use into more daily clinical practice. With the improved accuracy of the susceptibility values inside veins, this method could be used potentially to improve quantification of venous oxygen saturation [18].

REFERENCES

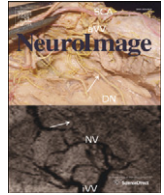
- Haacke EM, Mittal S, Wu Z, Neelavalli J, Cheng YC. Susceptibility-weighted imaging: technical aspects and clinical applications, part 1. *AJNR Am J Neuroradiol* 2009;30:19–30.
- Mittal S, Wu Z, Neelavalli J, Haacke EM. Susceptibility-weighted imaging: technical aspects and clinical applications, part 2. *AJNR Am J Neuroradiol* 2009;30:232–252.
- Haacke EM, Reichenbach JR. *Susceptibility weighted imaging in MRI: basic concepts and clinical applications*. Hoboken, NJ: Wiley; 2011.
- Duyn JH, van Gelderen P, Li TQ, de Zwart JA, Koretsky AP, Fukunaga M. High-field MRI of brain cortical substructure based on signal phase. *Proc Natl Acad Sci USA* 2007;104:11796–11801.
- Haacke EM, Lai S, Yablonskiy DA, Lin W. In-vivo validation of the BOLD mechanism: a review of signal changes in gradient-echo functional MRI in the presence of flow. *Int J Imaging Syst Technol* 1995; 6:153–163.
- Rauscher A, Sedlacik J, Barth M, Mentzel HJ, Reichenbach JR. Magnetic susceptibility-weighted MR phase imaging of the human brain. *AJNR Am J Neuroradiol* 2005;26:736–742.
- Haacke EM, Cheng NY, House MJ, Liu Q, Neelavalli J, Ogg RJ, Khan A, Ayaz M, Kirsch W, Obenaus A. Imaging iron stores in the brain using magnetic resonance imaging. *Magn Reson Imaging* 2005;23:1–25.
- Koch KM, Papademetris X, Rothman DL, de Graaf RA. Rapid calculations of susceptibility-induced magnetostatic field perturbations for in vivo magnetic resonance. *Phys Med Biol* 2006;51: 6381–6402.
- de Rochefort L, Brown R, Prince MR, Wang Y. Quantitative MR susceptibility mapping using piece-wise constant regularized inversion of the magnetic field. *Magn Reson Med* 2008;60:1003–1009.
- Cheng YC, Neelavalli J, Haacke EM. Limitations of calculating field distributions and magnetic susceptibilities in MRI using a Fourier based method. *Phys Med Biol* 2009;54:1169–1189.
- Wharton S, Schafer A, Bowtell R. Susceptibility mapping in the human brain using threshold-based k-space division. *Magn Reson Med* 2010;63:1292–1304.
- Wharton S, Bowtell R. Whole-brain susceptibility mapping at high field: a comparison of multiple- and single-orientation methods. *Neuroimage* 2010;53:515–525.
- Schweser F, Deistung A, Lehr BW, Reichenbach JR. Differentiation between diamagnetic and paramagnetic cerebral lesions based on magnetic susceptibility mapping. *Med Phys* 2010;37:5165–5178.
- Kressler B, de Rochefort L, Liu T, Spincemaille P, Jiang Q, Wang Y. Nonlinear regularization for per voxel estimation of magnetic susceptibility distributions from MRI field maps. *IEEE Trans Med Imaging* 2010;29:273–281.
- Shmueli K, de Zwart JA, van Gelderen P, Li TQ, Dodd SJ, Duyn JH. Magnetic susceptibility mapping of brain tissue in vivo using MRI phase data. *Magn Reson Med* 2009;62:1510–1522.
- Schafer A, Wharton S, Gowland P, Bowtell R. Using magnetic field simulation to study susceptibility-related phase contrast in gradient echo MRI. *Neuroimage* 2009;48:126–137.
- Liu T, Spincemaille P, de Rochefort L, Kressler B, Wang Y. Calculation of susceptibility through multiple orientation sampling (COSMOS): a method for conditioning the inverse problem from measured magnetic field map to susceptibility source image in MRI. *Magn Reson Med* 2009;61:196–204.
- Haacke EM, Tang J, Neelavalli J, Cheng YC. Susceptibility mapping as a means to visualize veins and quantify oxygen saturation. *J Magn Reson Imaging* 2010;32:663–676.

19. Li W, Wu B, Liu C. Quantitative susceptibility mapping of human brain reflects spatial variation in tissue composition. *NeuroImage* 2011;55:1645–1656.
20. Liu T, Liu J, de Rochefort L, Spincemaille P, Khalidov I, Ledoux JR, Wang Y. Morphology enabled dipole inversion (MEDI) from a single-angle acquisition: comparison with COSMOS in human brain imaging. *Magn Reson Med* 2011;66:777–783.
21. Li L, Leigh JS. Quantifying arbitrary magnetic susceptibility distributions with MR. *Magn Reson Med* 2004;51:1077–1082.
22. de Rochefort L, Liu T, Kressler B, Liu J, Spincemaille P, Lebon V, Wu J, Wang Y. Quantitative susceptibility map reconstruction from MR phase data using bayesian regularization: validation and application to brain imaging. *Magn Reson Med* 2010;63:194–206.
23. Li Y, Xu N, Fitzpatrick JM, Morgan VL, Pickens DR, Dawant BM. Accounting for signal loss due to dephasing in the correction of distortions in gradient-echo EPI via nonrigid registration. *IEEE Trans Med Imaging* 2007;12:1698–1707.
24. Grabner G, Trattnig S, Barth M. Filtered deconvolution of a simulated and an in vivo phase model of the human brain. *J Magn Reson Imaging* 2010;32:289–297.
25. Deville G, Bernier M, Delrieux J. NMR multiple echoes observed in solid ^3He . *Phys Rev B* 1979;19:5666–5688.
26. Marques JP, Bowtell R. Application of a Fourier-based method for rapid calculation of field inhomogeneity due to spatial variation of magnetic susceptibility. *Concepts Magn Reson B Magn Reson Eng* 2005;25:65–78.
27. Salomir R, De Senneville BD, Moonen CTW. A fast calculation method for magnetic field inhomogeneity due to an arbitrary distribution of bulk susceptibility. *Concepts Magn Reson B Magn Reson Eng* 2003;19:26–34.
28. Hagberg GE, Welch EB, Greiser A. The sign convention for phase values on different vendor systems: definition and implications for susceptibility weighted imaging. *Magn Reson Imaging* 2010;28:297–300.
29. Demmel JW. Perturbation theory for the least squares problem. *Applied numerical linear algebra*. Berkeley, CA: SIAM; 1997. pp 117–118.
30. Hoffman RE. Measurement of magnetic susceptibility and calculation of shape factor of NMR samples. *J Magn Reson* 2006;178:237–247.
31. Spees WM, Yablonskiy DA, Oswood MC, Ackerman JJ. Water proton MR properties of human blood at 1.5 Tesla: magnetic susceptibility, $T(1)$, $T(2)$, $T^*(2)$, and non-Lorentzian signal behavior. *Magn Reson Med* 2001;45:533–542.
32. Haacke EM, Brown RW, Thomson MR, Venkatesan R. Magnetic resonance imaging. Physical principles and sequence design. New York: Wiley; 1999. 766 p.
33. Reichenbach JR, Venkatesan R, Schillinger DJ, Kido DK, Haacke EM. Small vessels in the human brain: MR venography with deoxyhemoglobin as an intrinsic contrast agent. *Radiology* 1997;204:272–277.
34. Buch S, Liu S, Neelavalli J, Haacke EM. Simulated 3D brain model to study the phase behavior of brain structures. In: *Proceedings of the 20th Annual Meeting of ISMRM*, Melbourne, Australia; 2012. p. 2332.
35. Smith SM. Fast robust automated brain extraction. *Hum Brain Mapp* 2002;17:143–155.
36. Schweser F, Deistung A, Lehr BW, Reichenbach JR. Quantitative imaging of intrinsic magnetic tissue properties using MRI signal phase: an approach to in vivo brain iron metabolism? *Neuroimage* 2011;54:2789–2807.
37. Pandian DS, Ciulla C, Haacke EM, Jiang J, Ayaz M. Complex threshold method for identifying pixels that contain predominantly noise in magnetic resonance images. *J Magn Reson Imaging* 2008;28:727–735.
38. Neelavalli J, Cheng YCN, Jiang J, Haacke EM. Removing background phase variations in susceptibility weighted imaging using a fast, forward-field calculation. *J Magn Reson Imaging* 2009;29:937–948.



Contents lists available at SciVerse ScienceDirect

NeuroImage

journal homepage: www.elsevier.com/locate/ynimg

Review

The role of susceptibility weighted imaging in functional MRI

E. Mark Haacke ^{a,*}, Yongquan Ye ^{b,1}^a MR Research Facility, Department of Radiology, Wayne State University, HUH-MR Research G030/Radiology, 3990 John R Road, Detroit, MI 48201, USA^b MR Research Facility, Department of Radiology, Wayne State University, DRH 5E-13, 3990 John R Road, Detroit, MI 48201, USA

ARTICLE INFO

Article history:

Received 3 October 2011

Revised 15 November 2011

Accepted 1 January 2012

Available online xxxxx

Keywords:

fMRI

SWI

High resolution

Blood oxygenation level

ABSTRACT

The development of functional brain magnetic resonance imaging (fMRI) has been a boon for neuroscientists and radiologists alike. It provides for fundamental information on brain function and better diagnostic tools to study disease. In this paper, we will review some of the early concepts in high resolution gradient echo imaging with a particular emphasis on susceptibility weighted imaging (SWI) and MR angiography (MRA). We begin with the history of our own experience in this area, followed by a discussion of the role of high resolution in studying the vasculature of the brain and how this relates to the BOLD (blood oxygenation level dependent) signal. We introduce the role of SWI and susceptibility mapping (SWIM) in fMRI and close with recommendations for future high resolution experiments.

© 2012 Elsevier Inc. All rights reserved.

Contents

Introduction	0
The role of high resolution	0
High resolution MR angiography: the role of saturation and dephasing	0
Susceptibility weighted imaging (SWI)	0
Susceptibility weighted imaging and mapping (SWIM) and oxygen saturation maps	0
Summary and conclusions	0
Acknowledgement	0
References	0

Introduction

In the early 1990s, our research interests were in developing and understanding 3D gradient echo imaging methods to study neurological diseases. It would be no surprise to the reader that we were delighted to see the early work from Seiji Ogawa at Bell Labs (Ogawa et al., 1993) and Jack Belliveau and colleagues at MGH (Belliveau et al., 1991) regarding the use of magnetic resonance imaging (MRI) for functional MRI (fMRI) of the brain. The news came to our attention quickly, as we were then focusing on the effects of changes in local fields in gradient echo imaging at Case Western Reserve University (CWRU) more as artifacts than as a useful tool. At that time, we had interests in O¹⁷ imaging (Hopkins et al., 1988; Kwong et al., 1991)

using gradient echo imaging for brain function and Amos Hopkins, the major instigator in this direction, became interested immediately in collaborating with people at MGH on the concept of fMRI with O¹⁷ imaging. Some of the experiments done in this area showed that we could see major changes in the pial veins between activation and resting state (Frahm et al., 1993; Haacke et al., 1994; Lai et al., 1993), and that the early explanation of diffusion as the source of signal change in fMRI was likely not correct. This began what was then known as the brain/vein debate.

It took some years later and a number of key papers to show that the intravascular and extravascular effects, at least at 1.5 T, were the major sources of signal change in fMRI. To demonstrate this, researchers applied strong dephasing gradients and/or saturation pulses to basically remove the arterial signal from the images and then evaluated the fMRI response (Duong et al., 2003). After suppressing blood flow, there was little fMRI response remaining, implicating a major intravascular source. An example of the effect of saturation pulses applied outside the slices of interest for a 3 T fMRI experiment

* Corresponding author. Fax: +1 313 745 9182.

E-mail addresses: nmrimg@aol.com (E.M. Haacke), mqyeah@gmail.com (Y. Ye).¹ Fax: +1 313 745 9182.

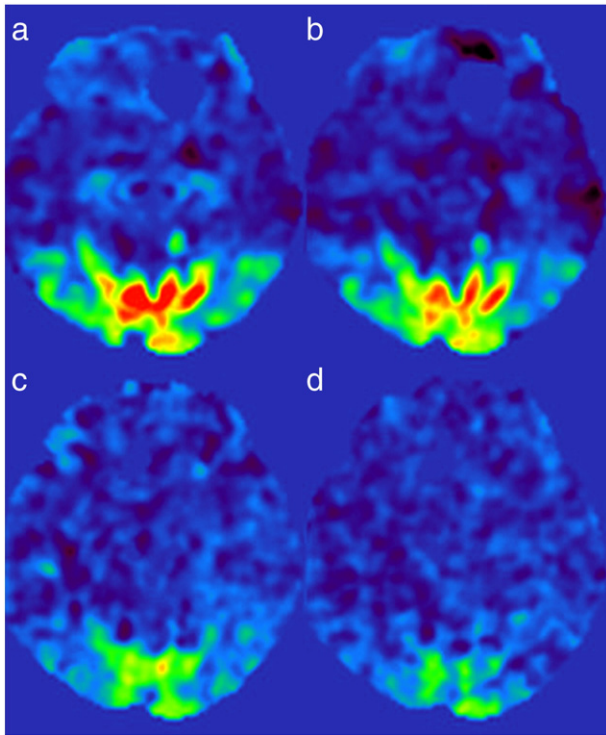


Fig. 1. GE- (a, b) and SE-EPI (c, d) t-maps obtained without (a, c) and with (b, d) blood saturation, showing a reduced BOLD response when blood signal is saturated. TE of GE- and SE-EPI was 24 ms and 96 ms respectively. The blood saturation was done by placing two saturation bands above and below the imaging slab, and the visual stimulation was 8 Hz flashing checkerboard with 30 s/30 s on/off block design.

in the visual cortex is shown in Fig. 1. Clearly, there is a decrease in the signal even for the gradient echo EPI sequence. It should be noted that for the long TR experiments used for whole brain multi-slice EPI, there is a strong inflow of fresh blood, which is referred to

as “inflow BOLD enhancement” (Duong et al., 2003; Duyn et al., 1994). By suppressing the signal from blood, the inflow BOLD enhancement effects are also suppressed, leaving only the extravascular effects. During the last 20 years, many papers have been written studying the role of intravascular and extravascular BOLD effects, even up to today, especially since higher and higher field strengths have become available and more and more signal is generated from extravascular effects (Baudendistel et al., 1998; Boxerman et al., 1995; Casciaro et al., 2008; Song et al., 2007; Ugurbil et al., 2000).

The role of high resolution

One of our goals has been to look for methods to increase resolution and yet keep imaging time reasonable. One early example of this was partial Fourier imaging (Haacke et al., 1999; Xu and Haacke, 2001). This approach allowed us (and still does) to take an asymmetric echo, keep flow compensation for short echoes, and collect many points after the echo to maintain high resolution in the read direction. We also focused on segmented EPI to improve speed for high resolution imaging (Haacke et al., 1986; Xu and Haacke, 2008). We believed that new information awaited us structurally and functionally if we could push resolution down to 100 μm . Today, high-field and parallel imaging are re-opening the door to that goal. The group in Minnesota pioneered this direction in the visual cortex by studying ocular dominance columns with high resolution fMRI (Menon et al., 1997; Yacoub et al., 2008). Of course, the most interesting approach would be to create high resolution functional imaging with anatomical qualities, whether it be vascular, metabolic, or brain function. No doubt researchers in this field will continue to fine tune the MR microscope to push these limits further and further in the future thanks to the continued technical developments that lead to higher signal-to-noise, faster imaging and better resolution.

Why high resolution? Evidently the workhorse for fMRI today remains a low resolution scan with roughly 3 mm resolution in each direction. The argument for this is that the signal-to-noise (SNR) has to be high enough that one can detect changes in signal as small as 1%. However, it depends on whether or not there is a scale invariant

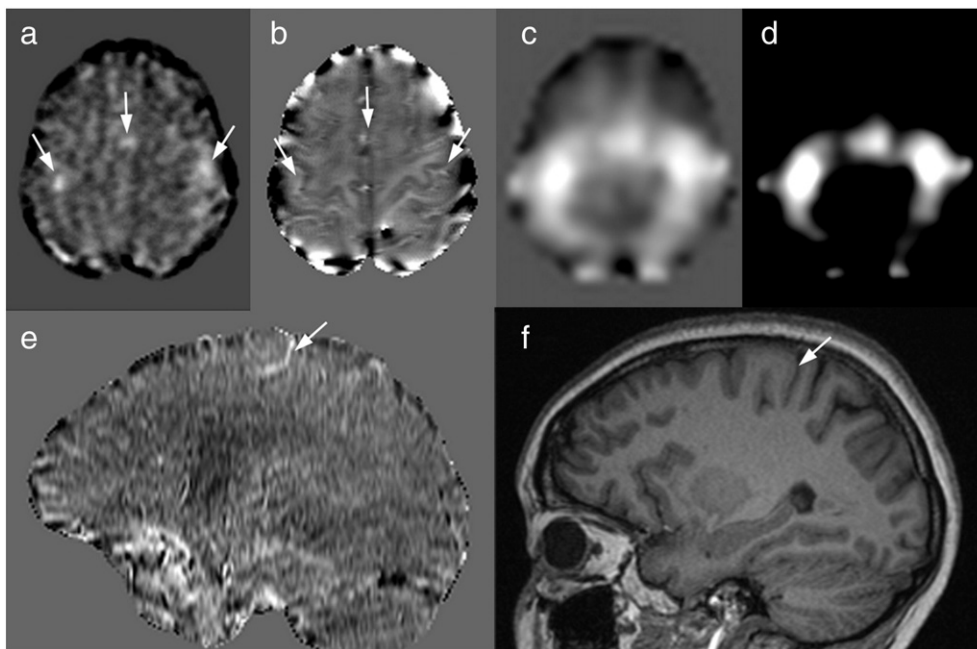


Fig. 2. Activations in the primary motor cortex using a block design finger tapping paradigm. (a) Filtered 3D GRE images of single subtraction between activation and resting state, with voxel size of $1.75 \times 1.75 \times 2 \text{ mm}^3$; (b) phase image from the same slice showing the motor cortex; (c) t-value map calculated from the GE-EPI data acquired using 3.5 mm isotropic voxels and a TE of 30 ms; (d) same as in (c) but with modified window level settings; (e) sagittal reformat of the 3D GE subtraction; and (f) sagittal MP-RAGE image. Imaging parameters for the 3D GRE sequence were: TR/TE = 30/20 ms, flip angle = 15° , BW = 80 Hz/pixel, $2 \times$ GRAPPA, resolution = $0.875 \times 0.875 \times 2 \text{ mm}^3$, $N_z = 64$, acquisition time for each block was 96 s. The average signal change in GE-EPI activation (d) is about 0.8% with maximum of 3.5%, and the signal change in the 3D GRE data (e) is about 14%.

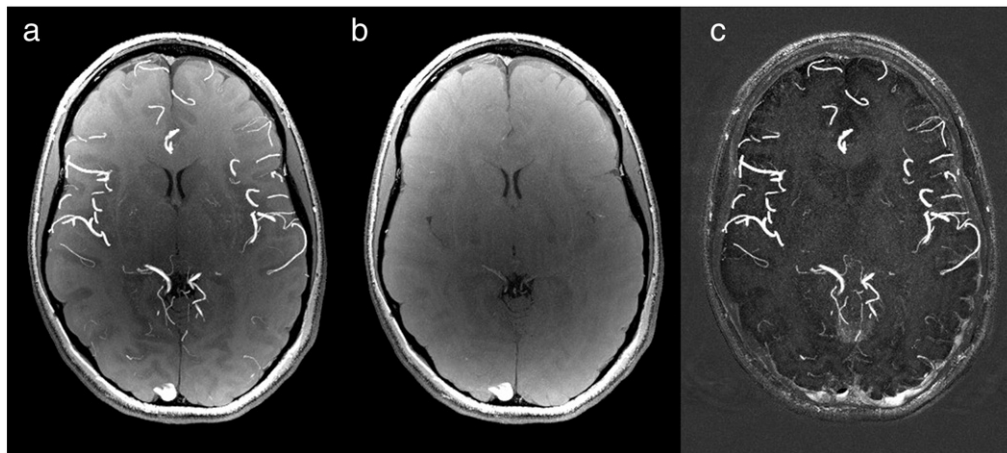


Fig. 3. (a) MaxIP images of a normal TOF; (b) TOF with a fixed arterial saturation pulse; and (c) their subtraction image. The imaging parameters were: $0.5 \times 0.5 \times 0.5 \text{ mm}^3$ isotropic voxels, TR/TE = 20/11 ms, flip angle = 15° , and fully flow compensated. All MaxIP was done over 16 slices. Although most major vessels are suppressed, one can see some remnant arterial/venous signal even with saturation. The reduced signal from the veins in this case actually leads to a poorer signal cancellation in the usual SWI data (not shown here) which relies on having a strong intravascular component.

response. For capillary structures, resolution is probably not important. But what are we really seeing in current low resolution EPI fMRI results? In 1999, Hoogenraad et al. (1999) showed that a very high resolution gradient echo scan could be used to collect fMRI data (albeit much more slowly than EPI) and then collapsed back to the same low resolution as EPI and that the results were basically the same. This suggests that the signal from the major veins still plays a key role in the fMRI response even for low resolution imaging (see Fig. 2).

As mentioned earlier, the only way to really remove the intravascular effects is by saturation or dephasing or both, and in this way one can be sure that the response being imaged is predominantly extravascular. But saturation alone may not explain the fact that there remains some signal from what appears to be the same location as before in Fig. 1 but just reduced in amplitude. Consider the high resolution angiogram in Fig. 3. The role of saturation can be appreciated in this figure and its effect is demonstrated by subtraction of the saturated data from the unsaturated data (Fig. 3c). The second image (Fig. 3b) shows that the signal from the arteries and veins is almost isointense to the surrounding tissue but certainly not completely nulled either due to T_1 recovery. To remove any remnant effects from the venous blood, one could then apply dephasing gradients. This should null any remaining intravascular contribution to the signal (see also (Song et al., 1996) and Fig. 4). This was indeed the argument in the early brain/vein debate.

The results in Fig. 2 however are very suggestive. They are identical in nature to the earlier results from Frahm et al. (1993), Haacke et al. (1994), Lai et al. (1993), only acquired faster at 3 T. The unfiltered EPI acquired with lower resolution show pretty much the same areas of activation. The filtered EPI activation t-maps have lost the ability for good spatial localization and show activation badly blurred over that portion of the brain. Perhaps one of the best clinical applications for these high resolution fMRI methods would be in the study of eloquent cortex when the neurosurgeon must operate on a tumor (Baudalet et al., 2006; Hou et al., 2006; Sherman et al., 2011). Given the results seen in the 3D data with complete visualization of the brain, one wonders why this method has not been used more in the last 20 years. Can we use high resolution gradient echo methods practically? To understand when this is possible, we need to first address the role of vessel size.

The work by Cheng and Haacke (2001) tried to address this question of scale variance more carefully, showing that the expected fMRI response is scale invariant when the voxels are larger than the largest veins, hence making EPI the method of choice after that point ($2 \times 2 \times 2 \text{ mm}^3$ is probably large enough to meet that limit and would provide far better spatial delineation than what people are using today which is often just a broadly spread out inflow enhanced vascular response). However, Haacke et al. (1994) and Cheng and Haacke (2001) also showed that when the scale becomes on the order of the vessel size and smaller, there will be a dramatic increase

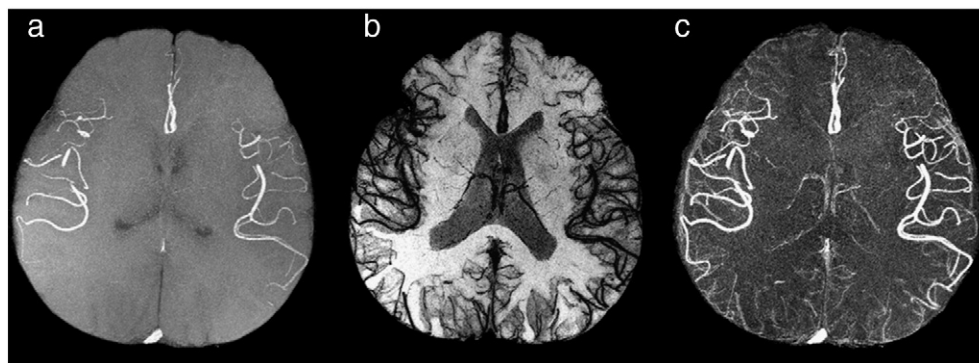


Fig. 4. (a) MRA MaxIP images acquired without dephasing gradients, and (b) MinIP images acquired with dephasing gradients, with a VENC value of 0.94 cm/s. Both arteries and even medullary veins are well suppressed. (c) is the result of subtracting (b) from (a), removing most of the background tissues while accentuating the vessels. All MaxIP was done over 16 slices of 0.5 mm thickness. In this subtraction both arteries and veins are evident although the venous structures are not as bright as the arteries structures in part because the signal from the veins is already suppressed because of their low T_2^* value.

in signal response. In fact, in [Lai et al. \(1993\)](#), the authors showed an image from [Duvernoy et al. \(1981\)](#) showing the pial vein, venules and capillaries, and commented that as resolution improves so will the ability to localize the fMRI signal once the resolution is on the order of the size of the vessel (vein) of interest. The general argument against this has been that there is not enough SNR or temporal resolution to collect the data at such high resolution (and [Cheng and Haacke's](#) paper even suggests this to a point). However, this has all changed with the advent of high fields such as 3 T and even more so with 7 T, where very high SNR and very high resolution fMRI has become viable. It is a testament to the progress made in MRI that the picture from [Duvernoy](#) showing the pial veins, venules and capillaries has basically been replicated now with SWI filtered phase ([Haacke et al., 1995; Haacke and Reichenbach, 2011](#)) and gradient echo images at 7 T ([Ge et al., 2008; Lee et al., 2010](#)) and is beginning to be seen at 3 T ([Haacke and Reichenbach, 2011](#)).

In the early days, much work went into suppressing the signal from the veins ([Duong et al., 2003; Glover et al., 1996](#)). But now it is possible to do what was alluded to in the work of [Haacke et al. \(1994\)](#), image the small draining veins adjacent to the activated tissue, especially if the goal is to do the neuroscience to understand the sources of the local neural activity involved in activation. With these high SNR, high resolution, rapid scanning methods, it should be possible to begin to see local changes in venous oxygen saturation (which is the underlying mechanism of BOLD effect) at the level of medullary veins (several hundred microns) to perhaps even local changes in venules (50 μm). It turns out that the optimal resolution according to [Cheng and Haacke](#) is about four times larger than the vessel volume. So a vein that is 250 μm could be seen and imaged with a resolution of 500 μm (as it is now with SWI for example ([Belliveau et al., 1992; Haacke et al., 1997, 2004, 2009; Mittal et al., 2009](#)) or a vessel that is 50 μm could be seen with a resolution of 100 μm . Practically, the results are better than [Cheng and Haacke](#) had anticipated. The 7 T data of today can already reveal venules with a resolution of $0.2 \times 0.2 \times 1 \text{ mm}^3$ ([Ge et al., 2008; Lee et al., 2010](#)). We can expect to see many more publications in the future on high resolution functional MRI using 3D gradient echo imaging techniques.

There are some practical issues that need to be dealt with to make imaging with high resolution more attractive. One of these is scanning time and the other is SNR. To cover the entire brain at 3 T with 64 2 mm thick slices and an in-plane resolution of $0.5 \text{ mm} \times 0.5 \text{ mm}$ will take about 5 min. Keeping a single activation task running for 5 min is not easy and then of course another 5 min to obtain the resting state images. However, with the marriage of parallel imaging and segmented echo-planar imaging, we anticipate this time being reduced to one and a half minutes. Reducing the resolution slightly to $1 \text{ mm} \times 1 \text{ mm} \times 2 \text{ mm}$ would further reduce the time by about 30 s. Now this allows for a more conventional block design of 30 s activation and 30 s resting for five cycles, allowing the entire 3D scan to take place in just 5 min. This is similar to current imaging times in most fMRI experiments.

High resolution MR angiography: the role of saturation and dephasing

Before we address the practical issue of high resolution fMRI with 3D gradient echo imaging and SWI, it is important to understand what is possible on the MR angiography side from the perspective of collecting high resolution data, enhancing contrast, and nulling signal from blood. In fMRI with EPI, one gets excellent intravascular signal contributions thanks to the inflow enhancement from the arterial side and hence venous signal. But with gradient echo imaging, blood signal will be suppressed with respect to gray matter due to blood's longer T_1 . One can do MRA both with and without contrast agent to best enhance the vascular signal and more importantly, the contrast between vessels and surrounding tissue. Recall that if the vascular signal is too low, the enhancement from the intravascular BOLD effect

will be minimized. [Fig. 3](#) and particularly [Fig. 4](#) show the capability of high resolution imaging in mapping out not just the major arteries but also, most importantly, smaller branches that are the basic source of blood supply to the tissue.

These images can be further improved by using a magnetization transfer contrast (MTC) pulse, using a saturation band, dephasing the signal from the moving spins, or other means to suppress the background. Consider the use of MTC as a first approach. The problem with MTC is that it lengthens the scan time and increases the specific absorption rate (SAR) making it less desirable to use at high magnetic fields. A second approach is to perform two scans: one with high vessel signal and the other with low signal and subtract them. One can use saturation bands to suppress the arterial signal or venous signal by saturating the inflowing blood, or use a strong set of bipolar gradients to dephase moving spins in both arteries and veins. The advantage of the bipolar gradients over saturation bands is that it suppresses fast flowing blood, requires no SAR increases and can be acquired in an interleaved TR manner (i.e., one TR with dephasing and the next TR without) without interfering with equilibrium of the magnetization and without suffering from misregistration artifacts. The VENC concept in flow quantification methods ([Haacke et al., 1999](#)) can be used to describe the dephasing effects, that flowing blood with a velocity higher than the VENC value will be dephased. Setting the VENC values to about 1 cm/s or less should do a reasonably good job dephasing laminar flow even for small vessels (250 to 500 μm sized arteries and veins). The disadvantage is that it still requires twice the time (except in some special double or triple echo sequence designs ([Kimura et al., 2009](#))), and both arteries and veins will be shown in the subtracted images. [Fig. 4a](#) shows an example of the usual arterial inflow effects, [Fig. 4b](#) a MinIP image showing that most vessels are dephased, and [Fig. 4c](#) the subtraction of [Fig. 4b](#) from [4a](#). As a side note, those in the fMRI field often quote a b-value rather than the VENC value. However, the bipolar gradients are not being used as diffusion gradients, nor is the diffusion effect the underlying mechanism for signal suppression here. Therefore, we have used the more conventional nomenclature from MR angiography of VENC value above which aliasing occurs. With a pair of bipolar rectangular gradients, for simplicity, one can relate the VENC value to the b-value via $\text{VENC} = \pi / (6b\tau)^{1/2}$ (since $\text{VENC} = \pi / (2\gamma G\tau^2)$ and $b = 2\gamma^2 G^2 \tau^3 / 3$), where τ is the duration of one gradient lobe. So, for example, if the applied gradient is 25 mT/m with 5 ms duration, then $b = 3.73 \text{ s/mm}^2$ and $\text{VENC} = 0.94 \text{ cm/s}$. Since the peak flows in pial veins is on the order of 1–4 cm/s, one can expect their signal to be fully suppressed with a VENC of 0.94 cm/s.

As a fourth approach, a contrast agent can be used to enhance vessel signal throughout the brain without being concerned about saturation effects even for slower flowing blood in small vessels. The challenge in imaging the vessels *in vivo* is to strive to mimic the example of the arteries from [Salamon \(1971\)](#) as shown in [Fig. 5a](#). In this sagittal view, one can see the radial branching of the arteries into the brain. Many of the major arteries that are a few millimeters in size bifurcate into arteries that are perhaps only 100 to 200 μm in size. These in turn branch into vessels only a few dozen microns in size and these finally to the capillaries. Using the high resolution MRA approach with contrast agent injection yields the comparative results shown in [Fig. 5b](#). Although no dephasing example has been used to subtract away the remaining background tissue, there is still clear evidence of small arteries in these images that are approaching 100 to 200 μm in size. A key component in understanding the role of the vasculature in BOLD imaging is to be able to map out the arteries and veins separately. Further, since a major component of the BOLD signal comes from intravascular effects, the use of a T_1 reducing contrast agent to increase the venous signal should in principle lead to an improvement in the BOLD response.

The thrust for high resolution MR angiographic approaches is not just to better understand the vascular structure and source of vascular

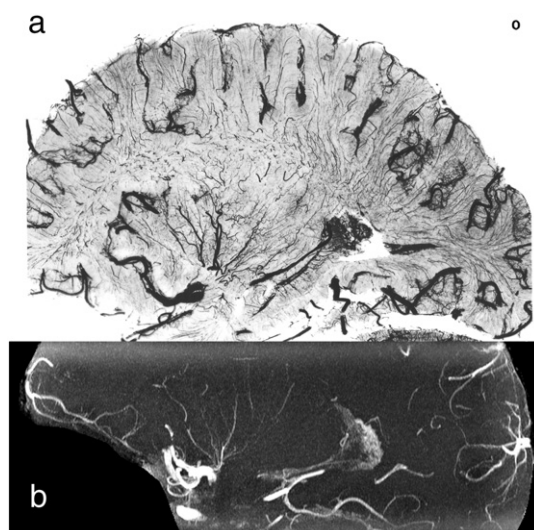


Fig. 5. (a) High resolution radiographic image of the arteries obtained by injecting radio-opaque dye in a cadaver brain within a few hours after death (Salamon, 1971). (b) A representative sagittal MaxIP image from a high resolution MRA dataset acquired in a transverse plane post-contrast with a voxel size of $0.25 \times 0.5 \times 0.5 \text{ mm}^3$ and then reformatted to match this sagittal view. Note the radial pattern of the arteries into the thalamus and surrounding regions. Many very small vessels can be seen on the order of only a few hundred microns. No subtraction was performed here.

signal, but also to consider the novel approach of using the arterial signal as a means to study inflow changes induced by the activation state. This has been considered in the past for arterial spin labeling applications in fMRI (Detre and Wang, 2002; Obata et al., 2004) and more recently for task induced arterial inflow changes (Kang et al., 2010). Being able to analyze the inflow as well as cerebral blood reserve (such as CBV and CBF) may serve as a bridge to connect arterial input and venous BOLD effects, as well as to understand the underlying vasculature basis for the significant inter-individual variation commonly seen in BOLD fMRI.

Susceptibility weighted imaging (SWI)

Throughout this early period our interest was to understand BOLD imaging by studying the veins. This focus eventually led to pushing the resolution limits until, in 1997 (Reichenbach et al., 1997), we came up with the concept of susceptibility weighted imaging (SWI). One of the key participants in this work was Jurgen Reichenbach, then a post-doctoral fellow in St. Louis, Missouri at the Mallinckrodt Institute of Radiology (he is now a full Professor running his own imaging laboratory at the Friedrich-Schiller Universität in Jena, Germany). Other researchers who were involved at this time included Song Lai (Lai et al., 1993) and Frank Hoogenraad (Hoogenraad et al., 1999). Although the precursor to this had been a paper in 1995 studying the susceptibility effects that could be visualized with phase (Haacke et al., 1995), the potential clinical applications started first with SWI. During the next ten years, we saw SWI show its value in a wide-ranging set of conditions such as aging, multiple sclerosis, stroke, trauma and tumors (Mittal et al., 2009). In 1997, we used phase for both flow and susceptibility to study changes in oxygen saturation in fMRI experiments using a method we referred to as SAIF for susceptibility and interleaved flow imaging (Haacke et al., 1997).

In the late 1990s, we proposed that multi-echo fMRI (Barth et al., 1999) would be of interest and would serve as a new tool to investigate the echo time dependence of the BOLD response and how it led to different spatial response patterns. In that work, we also evaluated phase data showing that phase could serve as a good marker for susceptibility (oxygen saturation) changes in fMRI. In 1995 (Haacke et al., 1995), 1997 (Haacke et al., 1997; Reichenbach et al., 1997), and

in 2004 (Haacke et al., 2004), we published again with an effort to push the SWI filtered phase as a useful tool in itself. We have also used the phase as a means to map the primary motor cortex as the iron content in the gray matter is quite high in this region and the phase images give excellent gray matter/white matter contrast there (Ogg et al., 1999). More recently, there has been increased interest and attention paid to phase in fMRI (Rowe and Haacke, 2009; Rowe and Logan, 2004). The final thrust in this direction is an interesting return to quantifying oxygen saturation using susceptibility mapping (de Rochefort et al., 2008; Haacke et al., 2010) or it has also been called susceptometry (Fernandez-Seara et al., 2006). Perhaps one day direct measurements of changes in oxygen saturation at the level of the smallest veins will be a viable means to study local neural responses.

Practically, SWI has been used to create exquisite images of the veins without contrast agent. The standard clinical approaches use a resolution of $0.5 \times 1.0 \times 2 \text{ mm}^3$ or when there is time $0.5 \times 0.5 \times 2 \text{ mm}^3$. The usual TE, TR and flip angle values at 3 T are 20 ms, 30 ms and 15° . Bandwidth is kept low at around 100 Hz/pixel to keep signal-to-noise high. With parallel imaging, whole brain coverage for the lower resolution of $0.5 \times 1.0 \times 2 \text{ mm}^3$ takes only 3 to 4 min. An example of a processed MRA/SWI data set at 3 T is shown in Fig. 6. Until recently, only one echo was used with SWI scans, but there are now a number of papers extolling the virtues of multiple echo SWI with the idea that the first echo can be used for MRA (Barnes and Haacke, 2009b; Deistung et al., 2009; Du and Jin, 2008; Haacke and Reichenbach, 2011), the second for SWI and the combination for T_2^* . Here the small medullary veins are clearly seen in the MinIP images for SWI. With sufficient resolution, phase can be measured in the small veins and is, of course, proportional to the susceptibility, which, in turn, is proportional to the deoxyhemoglobin content. Phase itself has been used to measure changes in flow indirectly through changes in oxygen saturation in traumatic brain injury studies (Shen et al., 2007) and more recently in stroke (Li et al., 2011b). But because phase is non-local and depends on the geometry of the source and the location of the object relative to the main field, a direct measure of the venous susceptibility would be more appropriate. Hence, our closing section will be about the use of susceptibility mapping to measure oxygen saturation (Barnes and Haacke, 2009a; Li et al., 2011a; Reichenbach et al., 1997).

Susceptibility weighted imaging and mapping (SWIM) and oxygen saturation maps

The ability to map oxygen saturation may help develop the potential of high resolution SWI as a means to detect local BOLD changes, especially

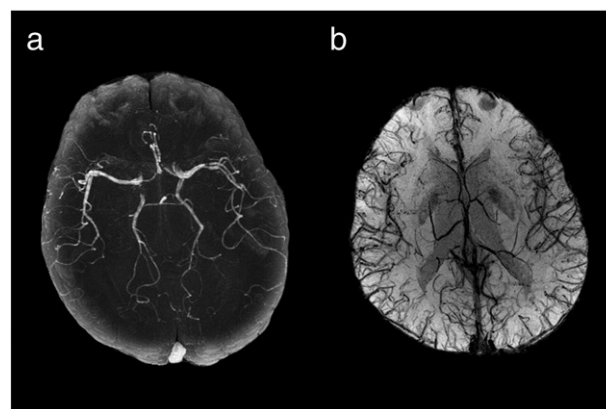


Fig. 6. An MRA MaxIP image (a) and SWI MinIP image (b) from the same data set with a $0.5 \times 0.5 \times 1 \text{ mm}^3$ voxel size. The original data was acquired using a single echo GRE sequence with TR/TE = 30/20 ms. Prior to the SWI MinIP processing, a two-slice sliding window averaging along the slice direction was done to enhance the phase effect.

at high fields. The presence of local changes in susceptibility causes a local change in magnetic field inside the object and a non-local change outside the object of interest. The phase inside the object is a constant while the change outside decays as $1/r^2$ for a cylinder and $1/r^3$ for a sphere. These non-local phases are generally unwelcome. SWI usually emphasizes phase of one sign and uses this to enhance the magnitude image (Reichenbach et al., 1997; Xu and Haacke, 2006).

As alluded to earlier, the phase itself is of great interest. It has been used for contrast between white matter and gray matter (Haacke et al., 1995, 1999; Ogg et al., 1999; Shmueli et al., 2009) and today for contrast between a variety of structures in the brain and throughout the body. It offers the potential to study everything from vessel wall to even imaging nerves (Haacke et al., 1999). The problem with phase is that it is a non-local manifestation of the magnetic field. However, this very non-local behavior contains everything we need to predict the inherent local susceptibility source (Deville et al., 1979; Haacke et al., 2010; Salomir et al., 2003). This has garnered great interest in the last few years to create a quantitative susceptibility map (QSM) of the tissue (de Rochefort et al., 2008; Liu et al., 2009; Marques and Bowtell, 2008; Salomir et al., 2003) for the study of brain iron and oxygen saturation. The latter is possible because the resulting field inside the veins is directly related to the hematocrit and the local oxygen saturation. Therefore, a QSM (or as we refer to it, SWIM) analysis can provide, in practice, a relative oxygen saturation map of the major veins in the body. When the hematocrit is known, the absolute oxygen saturation can be found (Barnes and Haacke, 2009b; Haacke and Reichenbach, 2011). With such a map, one could, in principle, open a new means to study fMRI by directly monitoring changes in oxygen saturation.

As a means to demonstrate a systemic BOLD effect, we scanned a subject with and without caffeine. The patient ingested a 200 mg NoDoz pill and then was scanned over a 30 min period. The SWI MinIP images are shown in Figs. 7a and b, and the SWIM MaxIP images are shown in Figs. 7c and d, both before and after caffeine intake.

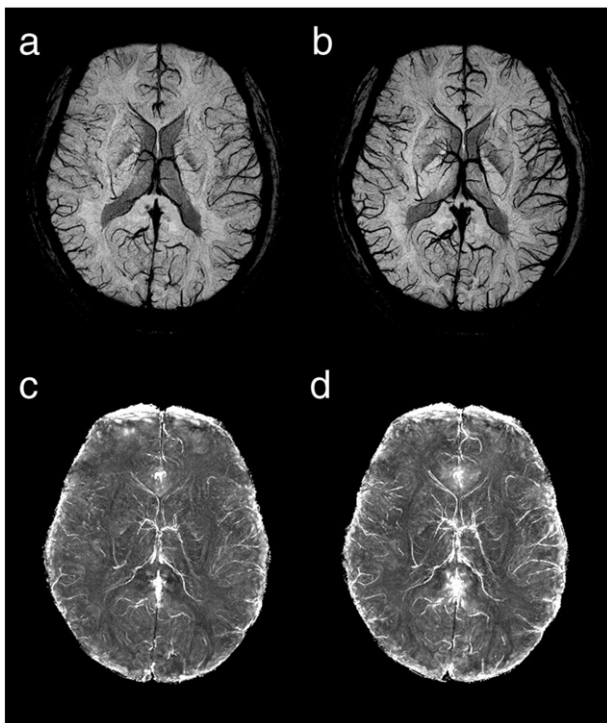


Fig. 7. Using susceptibility to monitor system changes in oxygen saturation. The SWI/SWIM results before (a, c) and after (b, d) 200 mg caffeine intake (one NoDoz pill) show significant systemic susceptibility changes in the veins, suggesting a corresponding change in oxygenation saturation. In the future, these types of SWIM images may provide a source of monitoring activation in high resolution, high field fMRI studies.

Although the SWI projections are qualitatively exquisite images, the QSM or SWIM projections are quantitative in nature. Despite the fact that the hematocrit is not known, a measurement of the venous signal changes normalized to the pre-caffeine data provides an accurate measure of the percent change in oxygen saturation and is independent of the hematocrit. It is very difficult to measure BOLD changes in the parenchyma since the blood volume fraction is so small and the BOLD changes are small, but this is not a problem in the major veins (Sedlacik et al., 2008). Even changes in the medullary veins are visible in Figs. 7c and d. Perhaps this new approach will open the door to using the veins as the major source of functional activity in the future rather than trying to discard the venous information.

Summary and conclusions

With the advent of high fields, it is now possible to image the vasculature of the brain with high resolution rapidly. Having the ability to do so provide a means to understand better the flow and function of the vasculature system and to model the vascular system for any individual. In return, modeling the system can predict what we expect to see from an activated to resting state (Marques and Bowtell, 2008). This will surely lead to a better understanding of why different individuals respond differently to specific stimuli, and certainly to separating out structural effects from real functional effects. Along these lines, we would recommend that all fMRI experiments that collect T_1 weighted images for anatomical information also collect a high resolution SWI scan to monitor the venous vasculature in the activated regions of interest.

Further, imaging with high resolution may herald the day when complicated statistical analysis will no longer be needed as rapid 3D scanning during a single activated and resting state may allow for simple subtractions to be used to monitor changes in the vascular system. When resolution becomes so high that individual local veins draining the activated region can be discerned, the percent change in fMRI experiments can jump to as high as 30% (Cheng and Haacke, 2001; Haacke et al., 1994; Lai et al., 1993).

Acknowledgement

The authors would like to acknowledge the Telemedicine and Advanced Technology Research Center for the support of this work through Award No: W81XWH-11-1-0493.

References

- Barnes, S., Haacke, E.M., 2009a. Settling properties of venous blood demonstrated in the peripheral vasculature using susceptibility-weighted imaging (SWI). *J. Magn. Reson. Imaging* 29, 1465–1470.
- Barnes, S.R., Haacke, E.M., 2009b. Susceptibility-weighted imaging: clinical angiographic applications. *Magn. Reson. Imaging Clin. N. Am.* 17, 47–61.
- Barth, M., Reichenbach, J.R., Venkatesan, R., Moser, E., Haacke, E.M., 1999. High-resolution, multiple gradient-echo functional MRI at 1.5 T. *Magn. Reson. Imaging* 17, 321–329.
- Baudelet, C., Cron, G.O., Gallez, B., 2006. Determination of the maturity and functionality of tumor vasculature by MRI: correlation between BOLD-MRI and DCE-MRI using P792 in experimental fibrosarcoma tumors. *Magn. Reson. Med.* 56, 1041–1049.
- Baudendistel, K.T., Reichenbach, J.R., Metzner, R., Schroeder, J., Schad, L.R., 1998. Comparison of functional MR-venography and EPI-BOLD fMRI at 1.5 T. *Magn. Reson. Imaging* 16, 989–991.
- Belliveau, J.W., Kennedy Jr., D.N., McKinstry, R.C., Buchbinder, B.R., Weisskoff, R.M., Cohen, M.S., Vevea, J.M., Brady, T.J., Rosen, B.R., 1991. Functional mapping of the human visual cortex by magnetic resonance imaging. *Science* 254, 716–719.
- Belliveau, J.W., Kwong, K.K., Kennedy, D.N., Baker, J.R., Stern, C.E., Benson, R., Chesler, D.A., Weisskoff, R.M., Cohen, M.S., Tootell, R.B., et al., 1992. Magnetic resonance imaging mapping of brain function. Human visual cortex. *Invest. Radiol.* 27 (Suppl 2), S59–S65.
- Boxerman, J.L., Hamberg, L.M., Rosen, B.R., Weisskoff, R.M., 1995. MR contrast due to intravascular magnetic susceptibility perturbations. *Magn. Reson. Med.* 34, 555–566.
- Casciaro, S., Bianco, R., Distanto, A., 2008. Quantification of venous blood signal contribution to BOLD functional activation in the auditory cortex at 3 T. *Magn. Reson. Imaging* 26, 1221–1231.
- Cheng, Y.C., Haacke, E.M., 2001. Predicting BOLD signal changes as a function of blood volume fraction and resolution. *NMR Biomed.* 14, 468–477.

- de Rochefort, L., Brown, R., Prince, M.R., Wang, Y., 2008. Quantitative MR susceptibility mapping using piece-wise constant regularized inversion of the magnetic field. *Magn. Reson. Med.* 60, 1003–1009.
- Deistung, A., Ditttrich, E., Sedlacik, J., Rauscher, A., Reichenbach, J.R., 2009. ToF-SWI: simultaneous time of flight and fully flow compensated susceptibility weighted imaging. *J. Magn. Reson. Imaging* 29, 1478–1484.
- Detre, J.A., Wang, J., 2002. Technical aspects and utility of fMRI using BOLD and ASL. *Clin. Neurophysiol.* 113, 621–634.
- Deville, G., Bernier, M., Delrieux, J., 1979. NMR multiple echoes observed in solid ^3He . *Phys. Rev. B* 19, 5666–5688.
- Du, Y.P., Jin, Z., 2008. Simultaneous acquisition of MR angiography and venography (MRAV). *Magn. Reson. Med.* 59, 954–958.
- Duong, T.Q., Yacoub, E., Adriany, G., Hu, X., Ugurbil, K., Kim, S.G., 2003. Microvascular BOLD contribution at 4 and 7 T in the human brain: gradient-echo and spin-echo fMRI with suppression of blood effects. *Magn. Reson. Med.* 49, 1019–1027.
- Duvernoy, H.M., Delon, S., Vannson, J.L., 1981. Cortical blood vessels of the human brain. *Brain Res. Bull.* 7, 519–579.
- Duyn, J.H., Moonen, C.T., van Yperen, G.H., de Boer, R.W., Luyten, P.R., 1994. Inflow versus deoxyhemoglobin effects in BOLD functional MRI using gradient echoes at 1.5 T. *NMR Biomed.* 7, 83–88.
- Fernandez-Seara, M.A., Techawiboonwong, A., Detre, J.A., Wehrli, F.W., 2006. MR susceptibility for measuring global brain oxygen extraction. *Magn. Reson. Med.* 55, 967–973.
- Frahm, J., Merboldt, K.D., Hancic, W., 1993. Functional MRI of human brain activation at high spatial resolution. *Magn. Reson. Med.* 29, 139–144.
- Ge, Y., Barnes, S., Heller, S., Xu, Y., Chen, Q., Haacke, E.M., Grossman, R.I., 2008. 3D high resolution susceptibility weighted imaging (SWI) venography at 3T and 7T. *Proc. Int'l. Soc. Magn. Reson. Med.* 17th Meeting, Honolulu, US.
- Glover, G.H., Lemieux, S.K., Drangova, M., Pauly, J.M., 1996. Decomposition of inflow and blood oxygen level-dependent (BOLD) effects with dual-echo spiral gradient-recalled echo (GRE) fMRI. *Magn. Reson. Med.* 35, 299–308.
- Haacke, E.M., Reichenbach, J.R., 2011. *Susceptibility Weighted Imaging in MRI: Basic Concepts and Clinical Applications*. Wiley-Blackwell, Hoboken, N.J.
- Haacke, E.M., Bearden, F.H., Clayton, J.R., Ling, N.R., 1986. Reduction of MR imaging time by the hybrid fast-scan technique. *Radiology* 158, 521–529.
- Haacke, E.M., Hopkins, A., Lai, S., Buckley, P., Friedman, L., Meltzer, H., Hedera, P., Friedland, R., Klein, S., Thompson, L., et al., 1994. 2D and 3D high resolution gradient echo functional imaging of the brain: venous contributions to signal in motor cortex studies. *NMR Biomed.* 7, 54–62.
- Haacke, E.M., Lai, S., Yablonskiy, D.A., Lin, W., 1995. In vivo validation of the BOLD mechanism: a review of signal changes in gradient echo functional MRI in the presence of flow. *Int. J. Imaging Syst. Technol.* 6, 153–163.
- Haacke, E.M., Lai, S., Reichenbach, J.R., Kuppusamy, K., Hoogenraad, F.G.C., Takeichi, H., Unl, W., 1997. In vivo measurement of blood oxygen saturation using magnetic resonance imaging: a direct validation of the blood oxygen level-dependent concept in functional brain imaging. *Hum. Brain Mapp.* 5, 341–346.
- Haacke, E.M., Brown, R., Thompson, M., Venkatesan, R., 1999. *Magnetic Resonance Imaging. Physical Principles and Sequence Design*. Wiley-Liss, New York.
- Haacke, E.M., Xu, Y., Cheng, Y.C., Reichenbach, J.R., 2004. Susceptibility weighted imaging (SWI). *Magn. Reson. Med.* 52, 612–618.
- Haacke, E.M., Mittal, S., Wu, Z., Neelavalli, J., Cheng, Y.C., 2009. Susceptibility-weighted imaging: technical aspects and clinical applications, part 1. *AJNR Am. J. Neuroradiol.* 30, 19–30.
- Haacke, E.M., Tang, J., Neelavalli, J., Cheng, Y.C., 2010. Susceptibility mapping as a means to visualize veins and quantify oxygen saturation. *J. Magn. Reson. Imaging* 32, 663–676.
- Hoogenraad, F.G., Hofman, M.B., Pouwels, P.J., Reichenbach, J.R., Rombouts, S.A., Haacke, E.M., 1999. Sub-millimeter fMRI at 1.5 Tesla: correlation of high resolution with low resolution measurements. *J. Magn. Reson. Imaging* 9, 475–482.
- Hopkins, A.L., Haacke, E.M., Tkach, J., Barr, R.G., Bratton, C.B., 1988. Improved sensitivity of proton MR to oxygen-17 as a contrast agent using fast imaging: detection in brain. *Magn. Reson. Med.* 7, 222–229.
- Hou, B.L., Bradbury, M., Peck, K.K., Petrovich, N.M., Gutin, P.H., Holodny, A.I., 2006. Effect of brain tumor neovasculature defined by rCBV on BOLD fMRI activation volume in the primary motor cortex. *Neuroimage* 32, 489–497.
- Kang, C.K., Kim, S.H., Lee, H., Park, C.A., Kim, Y.B., Cho, Z.H., 2010. Functional MR angiography using phase contrast imaging technique at 3T MRI. *Neuroimage* 50, 1036–1043.
- Kimura, T., Ikeda, M., Takemoto, S., 2009. Hybrid of opposite-contrast MR angiography (HOP-MRA) combining time-of-flight and flow-sensitive black-blood contrasts. *Magn. Reson. Med.* 62, 450–458.
- Kwong, K.K., Hopkins, A.L., Belliveau, J.W., Chesler, D.A., Pong, K.A., McInstry, R.C., Finelli, D.A., Hunter, G.J., Moore, J.B., Barr, R.G., et al., 1991. Proton NMR imaging of cerebral blood flow using H₂(17)O. *Magn. Reson. Med.* 22, 154–158.
- Lai, S., Hopkins, A.L., Haacke, E.M., Li, D., Wasserman, B.A., Buckley, P., Friedman, L., Meltzer, H., Hedera, P., Friedland, R., 1993. Identification of vascular structures as a major source of signal contrast in high resolution 2D and 3D functional activation imaging of the motor cortex at 1.5T: preliminary results. *Magn. Reson. Med.* 30, 387–392.
- Lee, J., Hirano, Y., Fukunaga, M., Silva, A.C., Duyn, J.H., 2010. On the contribution of deoxy-hemoglobin to MRI gray-white matter phase contrast at high field. *Neuroimage* 49, 193–198.
- Li, C., Langham, M.C., Epstein, C.L., Magland, J.F., Wu, J., Gee, J., Wehrli, F.W., 2011a. Accuracy of the cylinder approximation for susceptometric measurement of intravascular oxygen saturation. *Magn. Reson. Med.* doi:10.1002/mrm.23034.
- Li, M., Wu, J., Miao, Y., Yang, Z., Raza, W., Wang, Y., Haacke, E.M., Hu, J., 2011b. In vivo measurement of oxygenation changes after stroke using susceptibility weighted imaging. *Proc. Int'l. Soc. Magn. Reson. Med.* 19th Meeting, Montreal, Quebec, Canada, p. 4062.
- Liu, T., Spincemaille, P., de Rochefort, L., Kressler, B., Wang, Y., 2009. Calculation of susceptibility through multiple orientation sampling (COSMOS): a method for conditioning the inverse problem from measured magnetic field map to susceptibility source image in MRI. *Magn. Reson. Med.* 61, 196–204.
- Marques, J.P., Bowtell, R.W., 2008. Using forward calculations of the magnetic field perturbation due to a realistic vascular model to explore the BOLD effect. *NMR Biomed.* 21, 553–565.
- Menon, R.S., Ogawa, S., Strupp, J.P., Ugurbil, K., 1997. Ocular dominance in human V1 demonstrated by functional magnetic resonance imaging. *J. Neurophysiol.* 77, 2780–2787.
- Mittal, S., Wu, Z., Neelavalli, J., Haacke, E.M., 2009. Susceptibility-weighted imaging: technical aspects and clinical applications, part 2. *AJNR Am. J. Neuroradiol.* 30, 232–252.
- Obata, T., Liu, T.T., Miller, K.L., Luh, W.M., Wong, E.C., Frank, L.R., Buxton, R.B., 2004. Discrepancies between BOLD and flow dynamics in primary and supplementary motor areas: application of the balloon model to the interpretation of BOLD transients. *Neuroimage* 21, 144–153.
- Ogawa, S., Menon, R.S., Tank, D.W., Kim, S.G., Merkle, H., Ellermann, J.M., Ugurbil, K., 1993. Functional brain mapping by blood oxygenation level-dependent contrast magnetic resonance imaging. A comparison of signal characteristics with a biophysical model. *Biophys. J.* 64, 803–812.
- Ogg, R.J., Langston, J.W., Haacke, E.M., Steen, R.G., Taylor, J.S., 1999. The correlation between phase shifts in gradient-echo MR images and regional brain iron concentration. *Magn. Reson. Imaging* 17, 1141–1148.
- Reichenbach, J.R., Venkatesan, R., Schillinger, D.J., Kido, D.K., Haacke, E.M., 1997. Small vessels in the human brain: MR venography with deoxyhemoglobin as an intrinsic contrast agent. *Radiology* 204, 272–277.
- Rowe, D.B., Haacke, E.M., 2009. Magnitude and Phase Thresholding (MAPHT) of noisy complex-valued magnetic resonance images. *Magn. Reson. Imaging* 27, 1271–1280.
- Rowe, D.B., Logan, B.R., 2004. A complex way to compute fMRI activation. *Neuroimage* 23, 1078–1092.
- Salomon, G., 1971. *Atlas of the arteries of the human brain*. Sandoz, Paris.
- Salomir, R., de Senneville, B.D., Moonen, C.T.W., 2003. A fast calculation method for magnetic field inhomogeneity due to an arbitrary distribution of bulk susceptibility. *Concepts Magn. Reson.* 19B, 26–34.
- Sedlacik, J., Helm, K., Rauscher, A., Stadler, J., Mentzel, H.J., Reichenbach, J.R., 2008. Investigations on the effect of caffeine on cerebral venous vessel contrast by using susceptibility-weighted imaging (SWI) at 1.5, 3 and 7 T. *Neuroimage* 40, 11–18.
- Shen, Y., Kou, Z., Kreipke, C.W., Petrov, T., Hu, J., Haacke, E.M., 2007. In vivo measurement of tissue damage, oxygen saturation changes and blood flow changes after experimental traumatic brain injury in rats using susceptibility weighted imaging. *Magn. Reson. Imaging* 25, 219–227.
- Sherman, J.H., Hoes, K., Marcus, J., Komotar, R.J., Brennan, C.W., Gutin, P.H., 2011. Neurosurgery for brain tumors: update on recent technical advances. *Curr. Neurol. Neurosci. Rep.* 11, 313–319.
- Shmueli, K., de Zwart, J.A., van Gelderen, P., Li, T.Q., Dodd, S.J., Duyn, J.H., 2009. Magnetic susceptibility mapping of brain tissue in vivo using MRI phase data. *Magn. Reson. Med.* 62, 1510–1522.
- Song, A.W., Wong, E.C., Tan, S.G., Hyde, J.S., 1996. Diffusion weighted fMRI at 1.5 T. *Magn. Reson. Med.* 35, 155–158.
- Song, A.W., Guo, H., Truong, T.K., 2007. Single-shot ADC imaging for fMRI. *Magn. Reson. Med.* 57, 417–422.
- Ugurbil, K., Adriany, G., Andersen, P., Chen, W., Gruetter, R., Hu, X., Merkle, H., Kim, D.S., Kim, S.G., Strupp, J., Zhu, X.H., Ogawa, S., 2000. Magnetic resonance studies of brain function and neurochemistry. *Annu. Rev. Biomed. Eng.* 2, 633–660.
- Xu, Y., Haacke, E.M., 2001. Partial Fourier imaging in multi-dimensions: a means to save a full factor of two in time. *J. Magn. Reson. Imaging* 14, 628–635.
- Xu, Y., Haacke, E.M., 2006. The role of voxel aspect ratio in determining apparent vascular phase behavior in susceptibility weighted imaging. *Magn. Reson. Imaging* 24, 155–160.
- Xu, Y., Haacke, E.M., 2008. An iterative reconstruction technique for geometric distortion-corrected segmented echo-planar imaging. *Magn. Reson. Imaging* 26, 1406–1414.
- Yacoub, E., Harel, N., Ugurbil, K., 2008. High-field fMRI unveils orientation columns in humans. *Proc. Natl. Acad. Sci. U. S. A.* 105, 10607–10612.

Metadata of the chapter that will be visualized online

Series Title		
Chapter Title	The Presence of Venous Damage and Microbleeds in Traumatic Brain Injury and the Potential Future Role of Angiographic and Perfusion Magnetic Resonance Imaging	
Chapter SubTitle		
Copyright Year	2012	
Copyright Holder	Springer Science + Business Media New York	
Corresponding Author	Family Name	Haacke
	Particle	
	Given Name	E. M.
	Suffix	
	Division	Department of Radiology
	Organization	Wayne State University
	Address	48201, Detroit, MI, USA
	Email	nrmrimaging@aol.com
Author	Family Name	Raza
	Particle	
	Given Name	Waqar
	Suffix	
	Division	Department of Radiology
	Organization	Wayne State University
	Address	48201, Detroit, MI, USA
	Email	
Author	Family Name	Bo
	Particle	
	Given Name	Wu
	Suffix	
	Division	Department of Radiology
	Organization	Wayne State University
	Address	48201, Detroit, MI, USA
	Email	
Author	Family Name	Kou
	Particle	
	Given Name	Zhifeng
	Suffix	
	Division	Department of Radiology
	Organization	Wayne State University
	Address	48201, Detroit, MI, USA
	Email	
Abstract	Imaging plays a key role in the diagnosis and longitudinal follow up of traumatic brain injury (TBI). Among injury pathologies, vascular injury is associated with diffuse axonal injury (DAI) and traumatic	

axonal injury (TAI). The vascular network is ubiquitous and is an integral part of the tissue structure. In this chapter, we focus on angiographic and venographic-related imaging methods and their role in assessing mild, moderate, and severe TBI. We begin with an introduction to susceptibility weighted imaging (SWI) and magnetic resonance angiography (MRA) and then provide evidence of different types of vascular damage. Examples of TBI-induced microbleeds are presented along with the concept of low-impact medullary vein damage (MVD). This MVD has been seen even for so-called mild TBI cases. Vascular damage can also manifest as a reduction in local perfusion even when no clear macroscopic vessel damage is seen. To further understand the role of vascular abnormalities, we then introduce the different perfusion weighted imaging (PWI) techniques available and their application in TBI. The combination of SWI and PWI should make it possible to differentiate the role of local thrombus versus changes in oxygen saturation in MVD, for example. Since MRA and SWI are able to provide a full description of the brain's vasculature in 3D, we briefly discuss the presence of finite element modeling in understanding vascular injury. We conclude with recommendations related to the use of perfusion with MRA, SWI, and oxygen saturation measurements to obtain a complete picture of the hemodynamics of the brain.

Chapter 4

The Presence of Venous Damage and Microbleeds in Traumatic Brain Injury and the Potential Future Role of Angiographic and Perfusion Magnetic Resonance Imaging

E.M. Haacke, Waqar Raza, Wu Bo, and Zhifeng Kou

4.1 Introduction

Imaging is playing a more and more important role in the diagnosis and longitudinal follow up of traumatic brain injury (TBI). It has been suggested that for both anatomical and functional purposes magnetic resonance imaging (MRI) offers one of the best means to investigate the status of brain function and hemodynamics (Duhaime et al. 2010; Haacke et al. 2010a). Among injury pathologies, vascular injury is an important part of the spectrum. It is associated with diffuse axonal injury (DAI) and traumatic axonal injury (TAI). This bleeding has become a symbolic sign of brain tissue damage from DAI or TAI in diagnostic radiology (Grossman 1996). The vascular network is ubiquitous and is present at all levels in terms of size from the 5 μm capillaries, to the 50 μm arterioles and venules, to the several 100 μm large vessels, and finally those vessels on the order of a millimeter. Presumably, disruption of these vessels leads to a disturbance of local blood perfusion.

Vascular damage can manifest in a number of ways. Recently, Kou et al. gave a summary of the different patterns of vascular bleeding (Kou et al. 2008, 2010). Although more dated, chapter by Grossman et al. gives a classical description of the different types of hemorrhages (Grossman 1996). Anatomically, at a macroscopic level, both hemorrhages and non-hemorrhagic shearing lesions are found in major white matter (WM) tracts, including frontal white matter, corpus callosum, internal capsule, the upper part of the brain stem, the gray matter (GM)/(WM) boundaries and the cerebellar region. Morphologically, there are several types of bleeding. Extra axially, there are epidural and subdural hematomas, which could be caused by direct impact; subarachnoid hemorrhage, which can be seen reasonably well visualized with computed tomography (CT) and now with MRI as well (Wu et al. 2010)

E.M. Haacke, PhD (✉) • W. Raza, MS • W. Bo, BS • Z. Kou, PhD
Department of Radiology, Wayne State University, Detroit, MI 48201, USA
e-mail: nmrimaging@aol.com

and periventricular hemorrhage, which is due to the vascular damage along the ventricle walls or associated with damage in the splenium of the corpus callosum. For parenchymal hemorrhage, examples include (a) petechial microbleeds, where blood is seen to build up at isolated points after TBI; (b) DAI, where multi-focal bleeding is seen in the major white matter tracts; and (c) focal contusions, including coup and contra-coup contusions, which are often seen in direct impact or falls. If the focal contusion reaches a certain size, it may need immediate surgical intervention to alleviate the rise of intracranial pressure (ICP).

Of course any impact may have microvascular repercussions and, as such, damage could easily occur at both axonal and microvascular levels simultaneously since axons and neurons are completely intertwined with the vasculature (although each has its own unique mechanical properties). From a biomechanical point of view, the neural vasculature provides physical and structural support of neuronal and glial cells. From a physiological point of view, the blood flow provides nutritional support for neuronal and glial cells. By the time of axonal injury, it is hard to imagine that there is pure axonal injury without any vascular damage or functional disturbance. The impairment of the neurovascular blood supply further jeopardizes the nutritional support and the physiological hemostasis environment for neuronal cells to survive the recovery battle. This impairment may be manifest as a reduction in perfusion to the tissue. An immediate perfusion reduction is seen when using the weight drop impact model in rats using the Marmarou model even without any evident tissue damage (Shen et al. 2007). Perfusion usually recovers to normal levels within 72 h in rats. Depending on the injury severity, the vascular damage could present as macroscopic damage or bleeding or severe reductions in deoxyhemoglobin without any direct evidence of tissue damage. Damage to the vessel could lead to an impaired neural vascular tone, either sympathetic or parasympathetic vasoconstriction, and further result in the loss of control of blood flow or to reduced perfusion (Bouma and Muizelaar 1995). Or it may even be an autoimmune response through which the brain protects itself in case there is major bleeding after impact. We just do not yet understand the mechanisms behind these immediate responses to mechanical impact.

Furthermore, arteries and veins are different in many aspects. Anatomically, major veins are located on the surface of the brain with branches collecting returning blood from the inside of the brain, while major arteries are located inside the brain and tend to branch out. From Ommaya's Centripetal Theory or Gennarelli's Depth of Lesion model, with the increase of the injury severity, the injured locations tend to penetrate from the surface deeper into the brain. That means the brain surface is always the most vulnerable location of injury, which makes veins exposed to this trauma more vulnerable. Biomechanically, arteries are smaller but much stronger than veins since they must withstand the systolic blood pressure during the pumping of blood. Weaker venous walls makes veins more vulnerable than arteries for the same force of impact. As a result, the veins on the cortical surface tend to be the most vulnerable part of the vascular structure. Damage here may also lead to deeper damage to the veins draining into these surface veins. Originally developed as a venography technique, susceptibility weighted imaging (SWI) has the unique

capacity to visualize both venous structures and hemorrhagic bleeds. This allows researchers to visualize the spatial relationship between bleeding and vascular structures. Therefore, it is possibly to identify the possible bleeding of veins and/or the changes in local oxygen saturation of the tissue feeding these veins.

Modern imaging technologies now make it possible to image the vasculature, perfusion, and oxygen saturation all in one sitting with MRI methods. Although the former can also be done with CT angiography (CTA) using a contrast agent, CT is based on the use of ionizing radiation in the form of x-rays. On the other hand, MR angiography (MRA) and SWI can be used to image the arteries and the veins, respectively, down to 250 μm without a contrast agent. Perfusion imaging can also be done with CT with the help of a contrast agent. MRI also requires a contrast agent for dynamic contrast enhanced (DSC) perfusion weighted imaging (PWI). However a contrast agent is not required for arterial spin labeling (ASL) or for an average cerebral blood flow measurement using flow quantification in the neck (Haacke 2012). Although oxygen saturation can be measured using positron emission tomography, it is much more accessible and patient friendly to use when extracted from MRI measures such as T2(Lu and Ge 2008; Ge et al. 2012), T2*(Li et al. 1998), or susceptibility mapping (Haacke et al. 2010b).

In this chapter, we will focus on these angiographic- and venographic-related imaging methods and their role in assessing mild, moderate, and severe TBI. We will begin with an introduction to SWI and MRA and then provide evidence of different types of vascular damage at different levels of impact. We will show that for mild TBI, even when other damage is not visible with most clinical techniques, there is potential venous damage. We will then introduce the different perfusion techniques available and their application in TBI. After that, we will discuss the role of finite element modeling in understanding the vascular injury, and, finally we will conclude with recommendations related to the use of perfusion with MRA, SWI, and oxygen saturation measurements. Taken together, these MRI techniques offer different aspects of neural vascular injury and tend to complement each other to depict a clear panorama of this phenomenon.

4.2 Susceptibility Weighted Imaging (SWI) and Mapping (SWIM)

SWI exploits the susceptibility differences between tissues. It uses phase images to detect these differences and subsequently a phase mask to enhance the presence of veins, blood products, and iron-containing tissues. Due to its sensitivity to deoxyhemoglobin in venous blood and hemosiderin in hemorrhage, SWI is commonly used in TBI studies (Haacke et al. 2010b; Tong et al. 2008). Compared with the traditional invasive manner of clinical monitoring of cerebral vascular damage and reductions in blood flow, this method offers a novel, safe, and noninvasive approach to quantify changes in oxygen saturation and cerebral blood flow (Shen et al. 2007; Fujima et al. 2011) and to visualize structural changes in the brain's vasculature

after TBI. These three pieces of information can be used to improve the diagnosis of the state of health of brain tissue both pre- and post-TBI. The detection of micro-hemorrhages and shearing lesions in TAI/DAI in trauma patients is often difficult as the injuries tend to be relatively small and can be easily missed by low-resolution scans. SWI is usually run at relatively high resolution (1 mm³ or better) and is extremely sensitive to bleeding in the GM/WM boundaries making it possible to see very small lesions and increasing the ability to detect more subtle injuries.

The phase information collected in SWI represents the magnetic field distribution created from the different sources such as veins, microbleeds, ferritin, and hemosiderin. It is possible to use this phase information to find the local source of the field changes. Using a rather simple dipole approximation, it is possible to develop an inverse reconstruction approach that uses the phase information to create a source or susceptibility map (Haacke et al. 2010b; Zaitzu et al. 2011). We refer to this quantitative susceptibility mapping as SWIM. The problem with phase is that a simple spherical dipole source will create a non-local phase behavior that will make it very difficult to do a good job with SWI by itself. By creating SWIM data, that phase disappears and is replaced by the source itself, the local sphere. This new approach should make it possible to map out iron content in microbleeds and to map oxygen saturation in the major veins in the brain (Haacke et al. 2010b, 2011).

4.2.1 *Visible Vascular Injury in TBI and the Presence of Damaged or Compromised Medullary Veins*

In this section, we will review what can be seen in TBI using SWI and discuss a new finding, the presence of damaged or compromised medullary veins. Whenever there is damage to the vascular system that leaves behind extravasated blood, there is a good chance that it will be seen with SWI. Depending on the scope of the damage, one may see local damage as focal lesions or one may see widespread damage in the form of DAI. This damage may or may not produce an alteration in brain function. Successfully visualizing the damaged veins by itself is an important biomarker of TBI but, to be sure if there is or is not a perfusion deficit, one also needs to measure perfusion. Even if there is a perfusion loss in the putatively damaged tissue, one needs to measure oxygen saturation to see if the tissue function is intact. With all four components, the anatomy of the vasculature, the presence of vascular damage, the state of perfusion, and the level of oxygen saturation, it should be possible to obtain a relatively complete picture of the hemodynamics of the brain.

As a demonstration of the types of venous damage we are now seeing with SWI, we show several cases of medullary vein damage (MVD) from frontal and side impacts. Figure 4.1 shows two separate cases of mild TBI with clear damage to the medullary veins. In reviewing more than 100 TBI cases, including mild, moderate, and severe, we have seen 35 cases with MVD. Of the 100 cases, 15 of these were mild and of these 15 only 3 showed MVD. However, in these three cases, no other technique showed the presence of tissue damage (Figs. 4.1, 4.2, and 4.3).

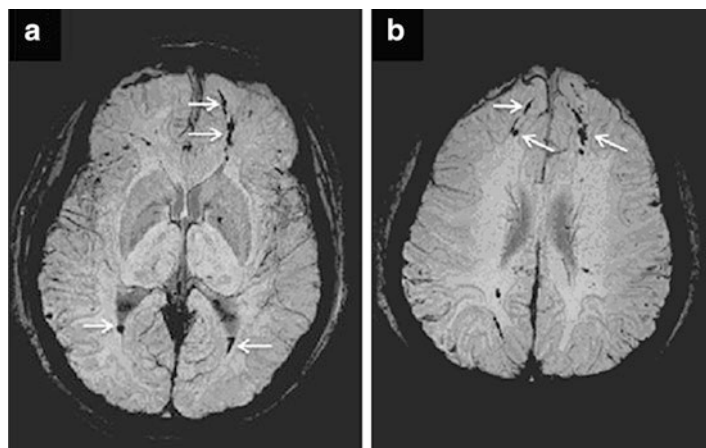


Fig. 4.1 Medullary vein damage in the frontal lobes shown with SWI. Resolution is $0.5\text{ mm} \times 0.5\text{ mm} \times 2\text{ mm}$. **(a)** MVD emanating from the septal vein in the left frontal lobe (*upper arrows*). This image also shows blood in the ventricles (*lower arrows*). **(b)** MVD in both the left and right frontal lobes. The damaged medullary veins are depicted by arrows

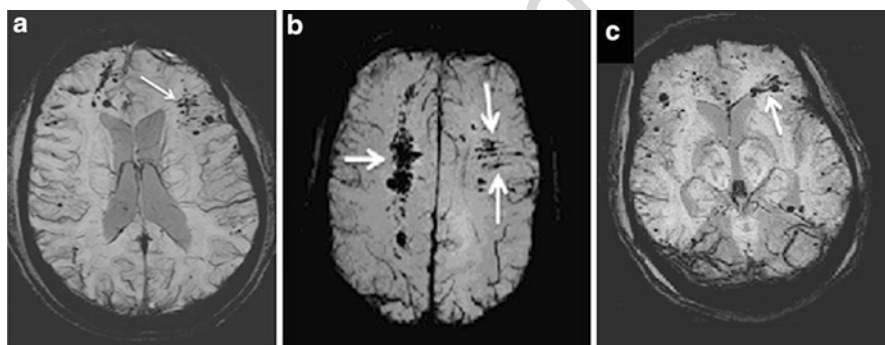


Fig. 4.2 Lateral medullary vein damage shown with SWI. Resolution is $0.5\text{ mm} \times 0.5\text{ mm} \times 2\text{ mm}$. **(a)** Lateral MVD in the frontal lobes. **(b)** Lateral MVD in the left temporal lobe. This patient also shows damage in the right anterior cerebral artery territory. **(c)** Lateral MVD in the left frontal lobe emanating from the septal vein. The damaged medullary veins are depicted by arrows

4.3 MR Angiography

158

Depending on the impact strength, the vasculature can be severely damaged in TBI. It behooves us to study the small vessel damage and eventually compare this to any perfusion deficit. The SWI data above already suggest that veins are more sensitive to abnormal stress/strain changes than arteries because they have weaker vessel walls. However, one would expect that would also be true for smaller arteries. In any case, to really do a complete job studying TBI, imaging both the small

159
160
161
162
163
164

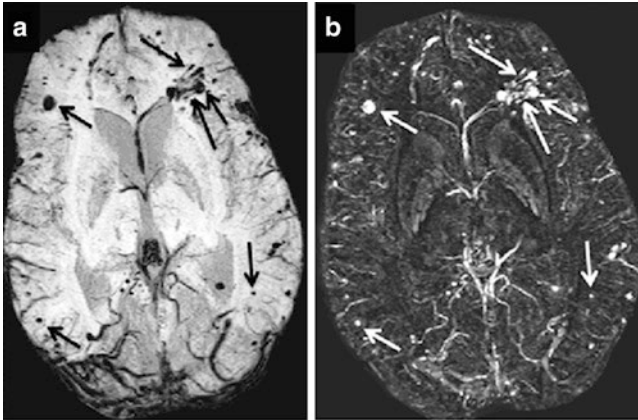


Fig. 4.3 Lateral medullary vein damage shown with both SWI and SWIM. Resolution is $0.5\text{ mm} \times 0.5\text{ mm} \times 2\text{ mm}$. The same subject from Fig. 4.2c is shown here with (a) the usual SWI minimum intensity projection and (b) the processed phase data used to create a SWIM image. The SWIM data makes it possible to quantify the amount of iron in the bleed and to monitor if this is resorbing over time, remains stable or continues to bleed. The damaged medullary veins are depicted by *long arrows* and the microbleeds by *short arrows*

arteries and small veins would seem to be the right way to go. Up to recently, the major focus in imaging vessels has been at the M1/M2/M3 levels but not beyond. Now the capability exists to see much smaller arteries, on the order of $100\text{--}250\text{ }\mu\text{m}$. The methods that make this possible are the usual time-of-flight (TOF) MRA methods, TOF with background suppression such as magnetization transfer contrast (MTC) or preferably, at high field, using a rephasing/dephasing method, and finally the use of a contrast agent to enhance the signal from the vessels far above the background tissue. In principle, the latter two can also be combined for potential further improvement in vessel–tissue contrast. An example of a conventional MR angiogram and the same individual post-contrast is shown in Fig. 4.4a. The data are collected with 0.5 mm isotropic resolution which means that even some $250\text{ }\mu\text{m}$ -sized vessels may be visualized if their signal is high enough. (Pushing this to $250\text{ }\mu\text{m}$ in plane resolution makes it possible to see even $100\text{ }\mu\text{m}$ -sized arteries but takes too long practically at the moment.) (Haacke et al. 2011). The advantage of the conventional approach is that there are no veins visible in the images. When a contrast agent is used, both arteries and veins get bright, although the larger veins tend to be not as bright at 3 T as they have a much lower $T2^*$. Despite the veins causing some difficulty in visualizing the arteries, with high-resolution 3D imaging, arteries and veins can be separated by image processing. Figure 4.4b shows that there are indeed smaller arteries now visible that could not be seen without the use of a contrast agent (Fig. 4.4).

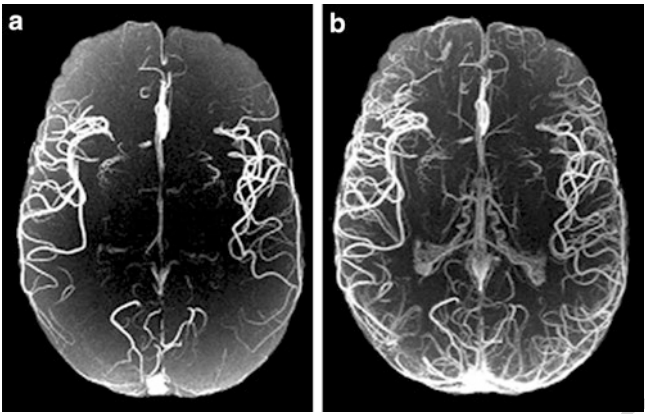


Fig. 4.4 MR angiograms with 0.5 mm isotropic resolution. (a) A conventional TOF MRA. (b) A contrast-enhanced TOF MRA. Clearly many veins are also now seen in the contrast-enhanced image. However, there are also many small arteries now visible that could not be seen before

4.4 Clinical Impact of Vascular Damage and Disrupted Perfusion to the Brain

Damage to vessels may cause a change in the brain's microcirculation that leads to a persistent state of hypoperfusion and improper delivery of vital metabolites to the brain parenchyma. The toxic contents may also leak through damaged blood brain barrier (BBB) into the already vulnerable neurons. This is not dissimilar to what we see with stroke patients, and it would behoove us to collect the same type of information for TBI patients. Early impairment of cerebral blood flow (CBF) in patients with severe injury correlates with poor brain tissue oxygenation (Zwienenberg and Muizelaar 2001). Some researchers have suggested that it would be important to normalize cerebral perfusion and blood flow after TBI for better outcome (Gennarelli 1987). In clinical studies, a global reduction in CBF has been found in the first few hours following TBI using ^{133}Xe (Zwienenberg and Muizelaar 2001; Gennarelli 1987; Gennarelli and Graham 1998; Kelly and Martin 1997). This is similar to what is found in animal studies as well (DeWitt et al. 1992). Patients who have a global CBF below the threshold for infarction (approximately 18 mL/100 g/min) (Bouma et al. 1991) have a worse clinical outcome. However, Zhao et al. reported a threshold for ischemia as 30 mL/100 g/min in his study (Zhao and Nowak 2006). Kelly et al. showed that outcome for patients with CBF less than this were poor (Kelly and Martin 1997). CBF and brain tissue oxygenation are proving to be crucial parameters to monitor in intensive care units along with others. Moreover, measurement of absolute regional blood flow at rest allows a clear estimation of the magnitude of blood flow changes that occur with drug treatment or other interventions. There are

several perfusion-imaging techniques available today for measuring cerebral perfusion in brain tissue and for visualizing the healthy and damaged vessels in the brain. We give a brief overview of these as they are related to applications in TBI.

4.4.1 Computer Tomography

Since the prohibition of the use of Xenon by the FDA, contrast enhanced perfusion has become the method of choice in CT. Computed tomography perfusion (CTP) is initiated by injecting iodinated contrast media (iodixanol) into a peripheral vein. Only a few studies have been performed on TBI using this technique but the results show that there were significant perfusion changes. One study reported a significant decrease of blood flow after trauma in a group comparison (Metting et al. 2010). However, unlike conventional CT, which can show bleeding or mass effect on individual basis, perfusion changes on CTP would rely on quantitative measurement to show group differences. Wintermark et al. suggested that intermittent perfusion-CT measurements will complement the information acquired by continuous cerebral perfusion pressure (CPP) alone. Perfusion-CT gives exclusive information about the regional heterogeneity of brain perfusion. This information will be very useful in differentiating patients with preserved auto-regulation and impaired autoregulation and could therefore steer interpretation of CPP measurements and therapy (Wintermark et al. 2004).

4.4.2 Positron Emission Computer Tomography

Positron emission tomography (PET) is a nuclear medicine test in which tissue function can be imaged. In A PET scan, the tracer stays in the blood stream rather than being absorbed by surrounding tissues, thereby limiting the images to areas where blood flows. Damaged tissues have reduced metabolic activity; therefore, gamma radiation from these areas is reduced or absent (Alexander 1995). Indeed, some PET data suggest discordance between blood flow and metabolism following TBI (Obrist et al. 1984); (Abu-Judeh et al. 1998; Mintun et al. 2001). The results of the Mintun study indicate that the metabolic state of the traumatically injured brain should be defined differentially in terms of glucose and oxygen metabolism. The use of FDG-PET demonstrates that hyperglycolysis occurs both locally and globally following severe head injury in humans cellular pathophysiology characteristic of head injury (Bergsneider et al. 1997). TBI studies in animals have shown a well-defined triphasic pattern of the cerebral metabolic rate of glucose (CMR_{glc}) (Bergsneider et al. 2001). The initial brief response of hyperglycolysis is followed by a second relatively prolonged period of metabolic depression. The second period, characterized by metabolic depression, typically lasts several hours and is associated with persistent neurological deficits as long as the metabolic depression is

present. The third period is characterized by a recovery behavioral function that parallels that of the recovery of metabolic function. No such pattern was seen in human data (Bergsneider et al. 2001).

Soustiel et al. compared the respective effects of established measures used for management of TBI patients on CBF and cerebral metabolic rates of oxygen (CMRO2), glucose (CMRGlc), and lactate (CMRLct) and found out that moderate hyperventilation could aggravate pre-existing impairment of CBF and metabolism (Soustiel et al. 2006). Therefore, TBI patients should be carefully monitored. Some suggest the use of mannitol for ICP control.

It is now well established that PET is somewhat superior to SPECT in terms of spatial resolution and permits a better visualization of subtle abnormalities. With the advent and implementation of novel tracers as well as improvement in instrumentation, molecular brain imaging using PET may be able to illustrate TBI pathophysiology and point to novel treatment strategies. However, despite these advantages PET requires the use of radiation.

4.4.3 Single-Photon Emission Computed Tomography (SPECT)

SPECT is a nuclear medicine tomography imaging technique that uses gamma rays to probe the tissue, specifically to show blood flow to tissues and organs. A SPECT scan integrates two technologies to view the body namely, CT and a radioactive material (tracer). The tracer makes it possible to see how blood flows to tissues and organs. Before the SPECT scan, a gamma-emitting radio-labeled chemical is injected into the blood stream that can then be detected by the scanner. The computer collects the information emitted by the gamma rays and translates them into two-dimensional cross-sections. These cross-sections can be merged to create a 3D image of the brain. A SPECT scan is primarily used to view blood flow through both arteries and veins in the brain. Tests have shown that it might be more sensitive to brain injury than either MRI or CT scanning because it can detect reduced blood flow to injured sites (Lewine et al. 2007; Abdel-Dayem et al. 1998). These qualifications aside, SPECT offers promise with regard to meeting the criteria of sensitivity, incremental validity, and clinical correlates. SPECT scans are cheaper and more readily available than the higher resolution PET scans, but they also still involve the use of radiation and radioactive agents. Another reason for SPECT not gaining so much popularity is that it requires co-registration with MRI.

4.4.4 Laser Doppler Flow

Laser Doppler is an inexpensive, noninvasive method of measuring the continuous circulation of blood flow on a microscopic level. The beam from a low-power laser (usually a laser diode) penetrates the skin sufficiently to be scattered with a

Doppler shift by the red blood cells and returns to be concentrated on a detector. These measurements are useful to monitor the effect of exercise, drug treatments, environmental, or physical manipulations on targeted micro-sized vascular areas.

It is reported by Rafols et al. using Laser Doppler Flow (LDF) that the hypoperfusion following TBI is a result of the loss of autoregulatory response of reacting vessels of the brain. This loss of autoregulation causes the improper delivery of oxygen and metabolites to the brain tissue and results in secondary injury and poor cognitive outcome (Rafols et al. 2007). In this study, he used the Marmarou model to induce TBI to avoid focal brain contusions and tissue necrosis. This study revealed a 37% reduction in cortical blood flow. Ultrastructural alterations in the lumen and wall of sensorimotor cortical microvessels, including endothelial cell distortion and luminal collapse, were seen between 1 and 48 h after trauma. Smooth muscle in the wall of reacting microvessels showed evidence of increased contractility that coincided temporally with the decreased perfusion of cortical CBF.

Thomale et al. showed that the acute hypoperfusion after TBI is due to vasoconstriction (Thomale et al. 2002). This study also found hyperemia occurring between 24 and 48 h after TBI in the controlled cortical impact model using LDF. Muir et al. studied the continuous pattern of CBF following TBI in a lateral percussion fluid model (Muir et al. 1992). The results showed that seconds after injury, blood flow in the left parietal cortex increased about 200% followed falling to about 80% of control after 5 min, and to 56% at the 1 h time point. Dewitt et al. reported that L-arginine administered after TBI prevents post-traumatic hypoperfusion and that pre-treatment with superoxide dismutase will restore CBF after a brief period of hypoperfusion (DeWitt et al. 1992). Lam et al. performed a study to monitor autoregulation using LDF in patients with head injury. It was concluded from the study that maintenance of CPP is important in preventing cerebral ischemia (Lam et al. 1997). Zweifel et al. showed that changes in CBF detected by LDF matched well with flow measurements performed with Transcranial Doppler Sonography (Christian et al. 2010).

The clinical application of LDF is limited by a number of problems. It can only access a small volume of brain tissue and thus can only monitor a focal area and LDF does not provide absolute values for blood flow. Further, since LDF is operator dependent especially in making contact on the skull for cases of subdural hematoma or prominent subarachnoid space, inaccurate measurements may follow (Lam et al. 1997).

4.4.5 Transcranial Doppler Sonography

Transcranial Doppler Ultrasound (TCD) is a noninvasive method for the measurement of flow in the major vessels in the head such as the middle cerebral artery (MCA), petrosal sinuses, and ophthalmic vessels. It is commonly used in the standard care of TBI patients. TCD is particularly accurate in detection of episodes of hypoperfusion induced by low CPP (Brandi et al. 2010), (Schmidt et al. 2000) and ICP (Homburg et al. 1993). This is a relatively quick and inexpensive test and is growing in popularity in the USA. The equipment is portable, making it possible to use not only in the

hospital but also in a doctor’s office, nursing home, or patient’s home. There are two methods used for recording the data. The first method uses “B-mode” imaging, which displays a two-dimensional image as seen by the ultrasound probe. Once the desired blood vessel is found, blood flow velocities can be measured with a pulsed Doppler probe to plot velocity over time. Together, these make a duplex test. The second method of recording uses only the second probe function, relying instead on the training and experience of the clinician in finding the correct vessels.

A number of observational studies have suggested that vasospasm develops in some patients following TBI (Oertel et al. 2005). Lee et al. confirmed that hemodynamically significant vasospasm with low CBF was a significant predictor of poor outcome (Lee et al. 1997). These studies have almost exclusively used TCD to identify vasospasm criteria similar to those used in subarachnoid hemorrhage. The limitation of transcranial Doppler is penetrating the bone. There are several “windows” through the temporal area that allow the visualization of the petrosal sinuses and the ophthalmic vein. TCD can also be used to measure flow in the middle, anterior, and posterior cerebral arteries.

Cerebral perfusion should be estimated as soon as possible after severe TBI to deaccelerate secondary brain injury. TCD is a simple and noninvasive method for cerebral perfusion assessment and is particularly accurate to detect hypoperfusion. Catherine et al. confirmed that early TCD makes it possible to identify high-risk patients with impaired cerebral perfusion and poor outcome. Moreover, this study (Catherine et al. 2007) has also discovered that TCD goal-directed therapy has the potential to improve cerebral perfusion before invasive cerebral monitoring is available, thereby limiting secondary brain injuries. Although study suggested the need for further studies to define optimal treatment TCD threshold values for the initial management of TBI, and its effect on outcome (Catherine et al. 2007).

4.4.6 *Magnetic Resonance Imaging*
350

MRI is perhaps the most used imaging modality for studying the anatomy and function of the brain today. The findings in standard MRI studies of TBI are similar to CT, but MRI is more sensitive than CT for small lesion detection such as TAI and DAI as seen with SWI (see above). MRI also offers a variety of different measures to study TBI such as Diffusion Tensor Imaging (DTI), Magnetic Resonance Spectroscopy Imaging (MRSI), and functional magnetic resonance imaging (fMRI) (Haacke et al. 2011) which are not part of the focus of this chapter. There are three major methods that are used at the moment to study either local or global perfusion to the brain.

4.4.6.1 *DSC Perfusion Weighted Imaging (PWI)*
359

PWI is sensitive to microscopic blood flow. The method is based on monitoring a non-diffusible contrast material gadolinium DTPA (dimeglumine pentaacetic acid or diethylenetriamine pentaacetic acid) passing through brain tissue. The signal

intensity decreases as the contrast bolus passes through the tissue and returns to normal over time. Recording this time-varying signal, and extracting the concentration as a function of time, it is possible to derive the following measures of blood flow, cerebral blood volume (CBV); CBF; mean transit time (MTT) and time to peak (TTP), as well as a variety of other hemodynamic parameters. To date, there are few studies describing the use of MR perfusion in TBI evaluation or predicting outcomes after TBI. One small study (Garnett et al. 2001) showed in patients with focal injuries visible in T2 images that reductions of rCBV were found in focal lesions and significant increases of rCBV were found in pericontusional areas. This finding is also consistent with the concept of traumatic penumbra (Menon 2003). Furthermore, a subset of these patients also showed reduced rCBV in normal appearing white matter, and these patients had significantly poorer outcomes (Garnett et al. 2001). Secondary damage in TBI is usually a result of altered hemodynamics and cerebrovascular factors. Hayward et al. investigated hemodynamic coupling between CBF and CBV. In this work, surprising results were found that CBV was the same for patients and controls in all regions considered. A significant decrease in CBF was found at 48 h after TBI but the CBV remained unchanged (Hayward Nick Mark 2011). Our own work in this direction has just begun. However, we have one example with deep MVD and PWI that appears to show several regions of reduced mean transit time (Fig. 4.5). If this pattern is found to be replicated in other cases, it would demonstrate that the damaged area is also associated with reduced perfusion (Fig. 4.5).

4.4.6.2 Arterial Spin Labeling

ASL is an arterial spin tagging technique that relies on the detection of magnetically labeled blood. Once the magnetization of the inflowing arterial blood has been modified (generally inverted) upstream, it induces a small MR signal change downstream (a few percent of the tissue magnetization). Meanwhile, the magnetization of the perfusion tracer (i.e., the labeled water) is rapidly relaxing. Return of the longitudinal magnetization toward its equilibrium values takes a few seconds. Although ASL techniques have not entered widespread clinical usage, their utility has been demonstrated for a variety of acute and chronic cerebrovascular diseases such as stroke and epilepsy. (Wintermark et al. 2005). One significant advantage of ASL is the ability to perform multiple repeated measurements without the use of a contrast agent. This might be necessary before and after treating the patient with a cerebrovascular dilator (acetazolamide) or vasoconstrictor inhibitor (clazosentan), for example. Kim et al. used ASL to measure the resting state CBF in 28 moderate to severe TBI patients in the chronic stage and found that (a) there was a global decrease of CBF compared to controls and (b) prominent regional hypoperfusion was present in the posterior cingulate cortices, the thalami, and multiple locations in the frontal cortices (Kim et al. 2010). However, in the population of mTBI, how cerebral perfusion is being affected in patients and their association with patients' neurocognitive status is still not understood. Given the milder severity in mTBI

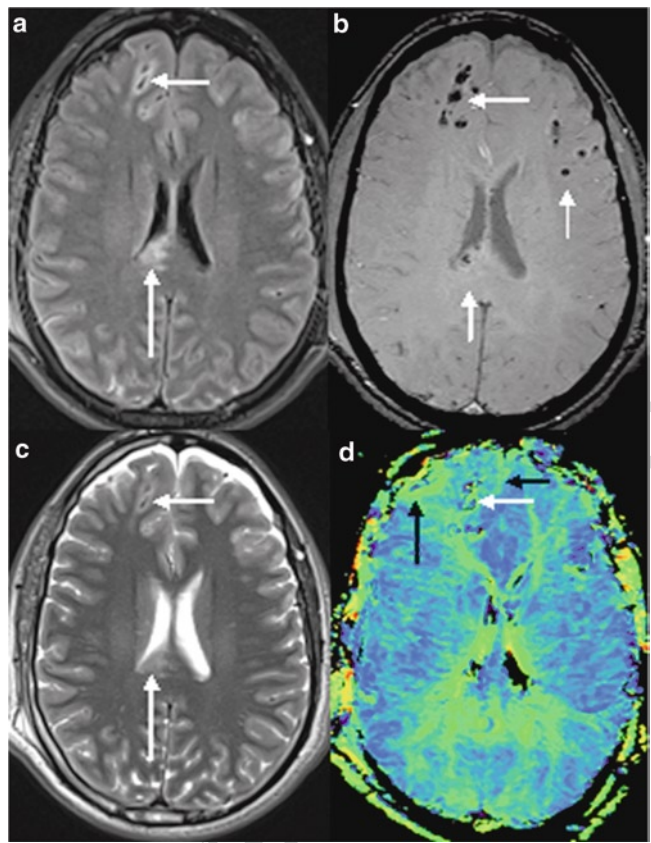


Fig. 4.5 An example of TBI case with frontal medullary vein damage and microbleeds. (a) FLAIR image showing two of the damaged frontal areas (*short arrow*) and enhanced signal in the splenium of the corpus callosum (*long arrow*). (b) SWI data showing multiple bleeds in the frontal, lateral, and the splenium of the corpus callosum (*short arrows*). (c) T2 weighted scan showing similar results to the FLAIR data. (d) Mean transit time images from the PWI data showing possible delayed arrival times in frontal regions and medial gray matter regions (*black arrows*) that may represent reduced perfusion to these tissues. Note the dark regions correspond to the bleeds and because of the long echo times used for PWI, the signal there was too small to be used to determine PWI parameters correctly and hence are set to zero here

patients, perfusion imaging at the acute stage could be meaningful both for clinical decision-making and patients' outcome prediction. Ge et al. also employed ASL to study 21 mTBI patients at the chronic stage and demonstrated reduced CBF in both sides of the thalamus, which is correlated with the patients' speed of information processing, memory, verbal, and executive function (Ge et al. 2009). ASL has also been used in conjunction with functional brain imaging studies and with animal studies, but these directions are outside the scope of the material presented in this chapter. However, some of the fMRI/ASL research does suggest that there are reductions in CBF that may be related to diffuse pathology.

405
406
407
408
409
410
411
412
413

4.4.6.3 Blood Flow Measurements in the Neck and the Poor Man's Bulk Perfusion Measure

Phase-contrast MR images are used for blood flow measurement in the neck and brain. Flow can be obtained for all major vessels in the neck thereby allowing a measure of the cardiovascular input and output to the brain. By measuring flow at C1/C2, one can focus on just the internal carotid artery and vertebral artery. By normalizing this arterial inflow to brain volume, it is possible to obtain the average flow in units of mL/100 g tissue/min. CSF flow can also be measured at this level. Similarly, by measuring flow at C7/T1, the total venous outflow can be determined. Flow is actually measured throughout the cardiac cycle (on the order of 20–40 points per cardiac cycle). A number of flow measures can be then determined including, flow velocity (average, peak positive, and peak negative), volume flow rate (average, positive, and negative), and total flow volume per cardiac cycle. The following arteries and veins of left and right sides are measured: common carotid arteries, internal/external carotid arteries, vertebral arteries, internal/external jugular veins, vertebral veins, deep cervical veins, anterior jugular vein, and any other major veins that are apparent.

4.5 Measuring Oxygen Saturation Changes with SWIM

Blood oxygen saturation imaging provides a means to monitor changes in oxygen saturation indirectly. SWI can be used to not only visualize small veins and microbleeds but also provide phase information for major veins. Such changes can occur when there is a change in blood flow. When the local field changes because of deoxyhemoglobin changes, the phase changes in and around the major veins. In Fig. 4.6 below, we show the effect of a systemic reduction in blood flow to the brain after ingestion of 200 mg of caffeine (the subject ingested a 200 mg NoDoz pill). Measuring changes in phase is tantamount to measuring changes in oxygen saturation (Shen et al. 2007). Similarly, reductions in perfusion or local bleeding can lead to the apparent enlargement of a local medullary vein (see Figs. 4.1 and 4.2) caused by either this blood oxygenation level dependent (BOLD) effect or by local bleeding in and around the vessel.

Applying susceptibility mapping to the phase yields a SWIM image (Fig. 4.7b) that looks similar to the SWI data of the venous system (Fig. 4.7a). Although the latter is important in detecting vascular abnormalities, it is not quantitative. With high-enough resolution and improved SWIM algorithms, it is expected that major veins (roughly 2 mm or greater in diameter) will yield reasonably accurate values for the oxygen saturation in those veins (Figs. 4.6 and 4.7).

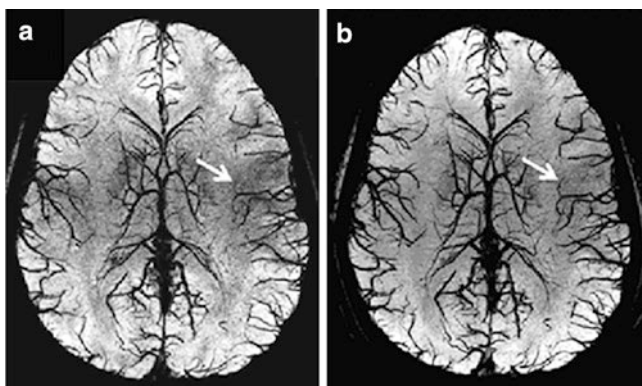


Fig. 4.6 SWI projection images showing the same individual (a) pre-caffeine and (b) post-caffeine. The patient had ingested one No-Doze pill containing 200 mg of caffeine. Note the increased contrast of the smaller veins. This is caused by the increased levels of deoxyhemoglobin after caffeine. Since caffeine is a vasoconstrictive agent, the blood flow slows to the brain. However, since the cerebral metabolic rate of oxygen utilization (CMRO₂) does not change, the amount of deoxyhemoglobin increases

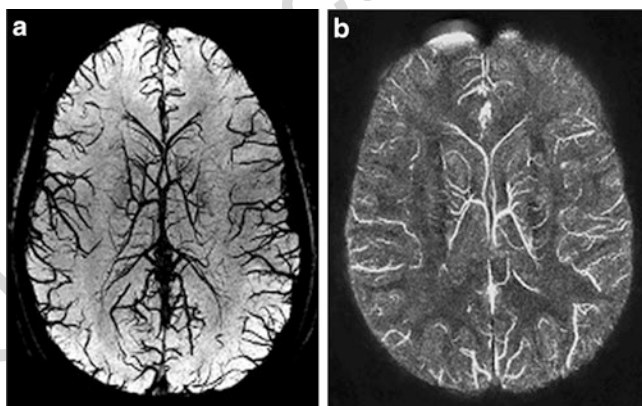


Fig. 4.7 SWI versus SWIM. (a) SWI projection image from Fig. 4.6b showing the major veins in the brain. (b) SWIM image (of a different individual) showing a quantitative map of oxygen saturation in the brain

4.6 Role of Finite element Modeling in Understanding TBI

Finite element (FE) models of brain injury are essential to study brain injury mechanisms. A number of studies have been conducted to investigate the contribution of the vasculature on the dynamic response of the brain in traumatic injury (Zhang et al. 2002). The hypothesis is that the vascular tree contributes to the strength of the neural tissues of the brain when it is subjected to applied loads. Data on mechanical properties of vascular tissues (Monson et al. 2000; Arbogast and Margulies 1997) suggest that cerebral vessels are much stiffer than brain tissue. Two-dimensional FE models of the brain with and without the simulation of major cerebral arteries were evaluated to test the hypothesis that the structural stiffness of the human brain is influenced by the pressure of these vessels. Overall results from this study suggests that explicit modeling of blood vessels increases the stiffness of the brain to resist both rotational and linear impulses and increases the threshold of neural injury. Zhang et al. assumed in her study that the blood vessel walls were directly connected to the surrounding brain tissues (Zhang et al. 2002). However, there is no data that describe the mechanical interaction between the vessels and brain.

Medullary vein damage may be due to the presence of internal shear forces (intracerebral stresses). How this occurs likely depends on the stiffness and natural frequency of the structure impacted. For impacts with structures of relatively low stiffness, the brain tends to move with the skull because of the predominantly low frequencies involved in these impacts. These movements result in intracerebral strains (ICS) that can produce lesions in the central parts of the brain. These ICS usually occur when the natural frequency of the impact is less than about 250 Hz, with the result that the outer parts of the brain move with the skull causing shear strains in the cerebral tissue as the inner parts of the brain lag behind the outer due to initial effect. A theoretical model suggests that the natural frequencies of the head and the structure are the characteristics with most importance in determining the distribution of injury in the brain for a particular location of impact on the head (Willinger et al. 1994). Clearly, knowing the tissue properties and the local structures of the vessels and how they are embedded in the surrounding tissue is necessary for proper modeling of the brain injury due to a given loading condition. The SWI and MRA data we have collected makes it possible to create an anatomically detailed FE model of the medullary veins down to 250 μm in size (see Fig. 4.8). Armed with this detailed local model embedded in the whole brain model and estimates for the tissue properties, it may be possible in the future to predict local venous damage and surrounding neural tissue injury. Some early attempts to model the vasculature from MRA data were presented by Parnaik et al. (2004) (Fig. 4.8).

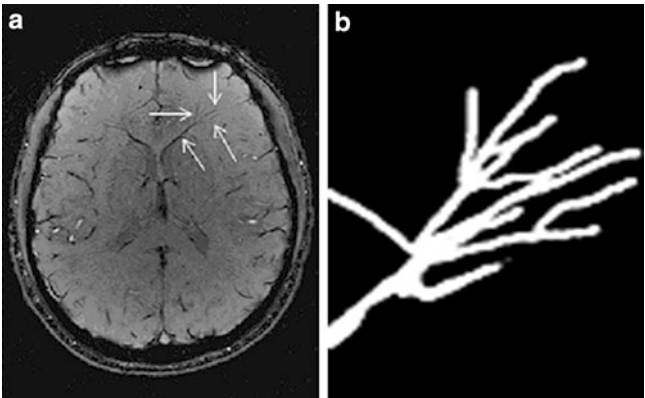


Fig. 4.8 Modeling the medullary veins. An SWI projection image is used to find medullary veins and then they are extracted in 3D. **(a)** An example image from SWI data showing the septal vein and the confluence of several medullary veins. **(b)** A projection of 3D model of medullary veins branching off the septal vein. The resolution in the model is $62.5\text{ }\mu\text{m}$ and vessel range in size from 1 mm (the septal vein) to the first branchings (0.5 mm) to the second branchings (0.25 mm). These veins can be damaged in frontal or side impact

4.7 Conclusions and Future Directions

SWI has proven to be one of the methods of choice along with DTI and T2 weighted FLAIR (Fluid Attenuation Inversion Recovery) when imaging TBI. SWI detects abnormalities caused by focal lesions and DAI, many of which may be missed in conventional MRI and CT scans. Currently, there is a paucity of information about perfusion in human TBI studies. It is likely that perfusion could play a major role in understanding patient outcomes. Perfusion combined with oxygen saturation measurements using SWIM may also open the door for a better understanding of the type of damage done in TBI. However, there is still one missing piece to the puzzle that is a critical precursor to understanding flow changes in TBI and that is the arterial system. Despite our focus on measuring blood products, veins, oxygen saturation, and perfusion, it is critical to gain an understanding of damage to the arterial system as well. Practically, the ideal protocol would be to start with an MR angiogram (MRA) and venogram (SWI) at the beginning of the scanning for TBI patients. Recently, we have implemented a double echo sequence that can be used to create both MRA and SWI data for such an analysis (Haacke et al. 2012). This should then be followed by a perfusion scan and any other key sequences such as FLAIR and DTI. We anticipate that it may then be possible to better diagnose many more mild TBI patients than is otherwise possible today.

Acknowledgments We would like to thank Sagar Bush for Fig. 4.8, Tang Jin for Fig. 4.7, Meng Li for Fig. 4.5, and Yongquan Ye for Fig. 4.4, and to Yongquan Ye for reviewing the chapter and Liying Zhang for reviewing the section on finite element methods for studying brain trauma.

References

- Abdel-Dayem HM, Abu-Judeh H, Kumar M, Atay S, Naddaf S, EL-Zeftawy H, Luo J (1998) SPECT brain perfusion abnormalities in mild or moderate traumatic brain injury. *Clin Nucl Med* 23(5):309–317
- Abu-Judeh H, Singh M, Masdeu JC (1998) Discordance between FDG uptake and technetium-99 m-HMPAO brain perfusion in acute traumatic brain injury. *J Nucl Med* 39:1357–1359
- Alexander MP (1995) Mild traumatic brain injury, pathophysiology, natural history, and clinical management. *Neurology* 45:1253–1260
- Arbogast KB, Margulies SS (1997) Regional differences in mechanical properties of the porcine central nervous system. SAE, Warrendale, PA, Proc. 41st Stapp Car Crash Conference, SAE Paper No. 973336
- Bergsneider M, Hovda D, Shalmon E, Kelly D, Vespa P, Martin N, Phelps M, McArthur D, Caron M, Kraus J, Becker D (1997) Cerebral hyperglycolysis following severe traumatic brain injury in humans, a positron emission tomography study. *J Neurosurg* 86:241–251
- Bergsneider M, Hovda D, McArthur DL, Etchepare M, Huang S, Sehati N, Satz P, Phelps ME, Becker DP (2001) Metabolic recovery following human traumatic brain injury based on FDG-PET, time course and relationship to neurological disability. *J Head Trauma Rehabil* 16(2):135–148
- Bouma GJ, Muizelaar JP (1995) Cerebral blood flow in severe clinical head injury. *New Horiz* 3(3):384–394
- Bouma GJ, Muizelaar JP, Choi SC, Newlon PG, Young HF (1991) Cerebral circulation and metabolism after severe traumatic brain injury: the elusive role of ischemia. *J Neurosurg* 75:585–593
- Brandi G, Bechir M, Sailer S, Habethur C, Stocker R, Stover JF (2010) Transcranial color-coded duplex sonography allows to assess cerebral perfusion pressure noninvasively following severe traumatic brain injury. *Acta Neurochir (Wien)* 152(6):965–972
- Catherine R, Sophie L, Nicolas B, Bernard V (2007) Transcranial Doppler ultrasound goal directed therapy for the early management of severe traumatic brain injury. *Intensive Care Med* 33:645–651
- Christian Z, Marek C, Andrea L, Gianluca C, Dong-Joo K, Emmanuel C, John P, Peter K, Peter S (2010) A comparison study of cerebral autoregulation assessed with transcranial Doppler and cortical laser Doppler flowmetry. *Neurol Res* 32(4):425–428
- DeWitt DS, Prough DS, Taylor CL, Whitley JM (1992) Reduced cerebral blood flow, oxygen delivery, and electroencephalographic activity after traumatic brain injury and mild hemorrhage in cats. *J Neurosurg* 76(5):812–821
- Duhaime AC, Gean AD, Haacke EM, Hicks R, Mukherjee P, Brody D, Latour L, Riedy G (2010) Common data elements in radiologic imaging of traumatic brain injury. *Arch Phys Med Rehabil* 91(11):1661–1666
- Fujima N, Kudo K, Terae S, Ishizaba K, Yazu R, Zaitsu Y, Tha K, Yoshida D, Sukhara AT, Haacke EM, Sasaki M (2011) Non-invasive measurement of oxygen saturation in the spinal vein using SWI: quantitative evaluation under conditions of physiological and caffeine load. *Neuroimage* 54(1):344–349
- Garnett M, Blamire A, Corkill R, Rajagopalan B, Young J, Cadoux-Hudson T, Styles P (2001) Abnormal cerebral blood volume in regions of contused and normal appearing brain following traumatic brain injury using perfusion magnetic resonance injury. *J Neurotrauma* 18(6):585–593
- Ge Y, Patel MB, Chen Q, Grossman EJ, Zhang K, Miles L, Babb JS, Reaume J, Grossman RI (2009) Assessment of thalamic perfusion in patients with mild traumatic brain injury by true FISP arterial spin labelling MR imaging at 3 T. *Brain Inj* 23(7):666–674

- Ge Y, Zhang Z, Lu H, Tang L, Jaggi H, Herbert J, Babb JS, Rusinek H, Grossman RI (2012) Characterizing brain oxygen metabolism in patients with multiple sclerosis with T2-relaxation-under-spin-tagging MRI. *J Cereb Blood Flow Metab* 32(3):403–412
- Gennarelli TA (1987) Cerebral concussions and diffuse brain injuries. In: Cooper PR (ed) *Head injury*. Williams and Wilkins, Baltimore, pp 108–124
- Gennarelli TA, Graham DI (1998) Neuropathology of the head injuries. *Semin Clin Neuropsychiatry* 3:160–175
- Grossman CB (1996) Magnetic resonance imaging and computed tomography of the head and spine. Williams & Wilkins, Baltimore, U.S.A
- Haacke EM (2004) Susceptibility weighted imaging (SWI). *Magn Reson Med* 52(3):612–618
- [AU2] Haacke EM, Ye Y (2012) The role of susceptibility weighted imaging in functional MRI. *Neuroimaging* (in press)
- Haacke EM, Duhaime AC, Gean AD, Riedy G, Wintermark M, Mukherjee P, Brody DL, DeGraba T, Duncan TD, Elovic E, Hurley R, Latour L, Smirniotopoulos JG, Smith DH (2010a) Common data elements in radiologic imaging of traumatic brain injury. *J Magn Reson Imaging* 32(3):516–543
- Haacke EM, Tang J, Neelavalli J (2010b) Susceptibility mapping as a means to visualize veins and quantify oxygen saturation. *J Magn Reson Imaging* 32(3):663–676
- Haacke EM, Reichenbach J, Xu Y (2011) *Susceptibility weighted imaging in MRI: basic concepts and clinical applications*. Wiley Blackwell, Hoboken, New Jersey
- Haacke EM, Feng W, Utriainen D, Trifan G, Wu Z, Latif Z, Katkuri Y, Hubbard D (2012) Patients with multiple sclerosis with structural venous abnormalities on MR imaging exhibit an abnormal flow distribution of the internal jugular veins. *J Vasc Interv Radiol* 23(1):60–68
- Hayward NM, Tuunanen PI, Immonen R, Ntode-Ekane XE, Pitkänen A, Gröhn O (2011) Magnetic resonance imaging of regional hemodynamics and cerebrovascular recovery after lateral fluid-percussion brain injury in rats. *J Cereb Blood Flow Metab* 31(1):166–177
- Homburg AM, Jakobsen M, Enevoldsen E (1993) Transcranial Doppler recordings in raised intracranial pressure. *Acta Neurol Scand* 87(6):488–493
- Kelly DF, Martin NA (1997) Cerebral blood flow as a predictor of outcome following traumatic brain injury. *J Neurosurg* 86:633–641
- Kim J, Whyte J, Patel S, Avants B, Europa E, Wang J, Slattery J, Gee JC, Coslett HB, Detre JA (2010) Resting cerebral blood flow alterations in chronic traumatic brain injury, an arterial spin labeling perfusion fMRI study. *J Neurotrauma* 27(8):1399–1411
- Kou Z, Benson RR, Haacke EM (2008) Susceptibility weighted imaging in traumatic brain injury. In: Gillard J, Waldman A, Barker P (eds) *Clinical MR neuroimaging*, 2nd edn. Cambridge University, Cambridge
- Kou Z, Wu Z, Tong KA, Holshouser B, Benson RR, Hu J, Haacke EM (2010) The role of advanced MR imaging findings as biomarkers of traumatic brain injury. *J Head Trauma Rehabil* 25(4):267–282
- Lam JMK, Hsiang JN, Poon WS (1997) Monitoring autoregulation using laser Doppler flowmetry in patients with head injury. *J Neurosurg* 86:438–445
- Lee J, Martin N, Alsina G, McArthur D, Zaucha K, Hovda D, Becker D (1997) Hemodynamically significant cerebral vasospasm and outcome after head injury, a prospective study. *J Neurosurg* 87(2):221–233
- Lewine JD, Davis JT, Bigler ED, Thoma R, Funke M, Sloan JH, Hall S, Orrison WW (2007) Objective documentation of traumatic brain injury subsequent to mild head trauma, multimodal brain imaging with MEG, SPECT, and MRI. *J Head Trauma Rehabil* 22(3):141–155
- Li D, Wang Y, Waight DJ (1998) Blood oxygen saturation in vivo using T2* estimation. *Magn Reson Med* 39(5):685–690
- Lu H, Ge Y (2008) Quantitative evaluation of oxygenation in venous vessels using T2-relaxation-under-spin-tagging MRI. *Magn Reson Med* 60(2):357–363
- Menon DK (2003) Procrustes, the traumatic penumbra, and perfusion pressure targets in closed head injury. *Anesthesiology* 98(4):805–807
- Metting Z, Rodiger LA, de Jong BM, Stewart RE, Kremer BP, van der Naalt J (2010) Acute cerebral perfusion Ct abnormalities associated with posttraumatic amnesia and mild head injury. *J Neurotrauma* 27(12):2183–2189

- Mintun MA, Lundstrom BN, Snyder AZ (2001) Blood flow and oxygen delivery to human brain during functional activity, theoretical modeling and experimental data. *Proc Natl Acad Sci USA* 98:6859–6864
- Monson KL, Barbaro NM, Goldsmith W, Manley G (2000) Static and dynamic mechanical and failure properties of human cerebral vessels. *Proc Crashworthiness, Occupant Protection, and Biomechanics in Transportation Systems* 49:255–265, AMD- 246/BED-49
- Muir JK, Boerschel M, Ellis EF (1992) Continuous monitoring of posttraumatic cerebral blood flow using laser-Doppler flowmetry. *J Neurotrauma* 9(4):355–362
- Obrist WD, Langfitt TW, Jaggi JL et al (1984) Cerebral blood flow and metabolism in comatose patients with acute head injury, relationship to intracranial hypertension. *J Neurosurg* 61:241–253
- Oertel M, Boscardin W, Orbits W, Glenn T, McArthur D, Gravori T, Lee J, Martin N (2005) Posttraumatic vasospasm, the epidemiology, severity, and time course of an underestimated phenomenon, a prospective study performed in 299 patients. *J Neurosurg* 103(5):812–824
- Parnaik Y, Beillas P, Demetropoulos CK, Hardy WN, Yang KH, King A (2004) The influence of surrogate blood vessels on the impact response of a physical model of the brain. *Stapp Car Crash J* 48:259–277
- Rafols J, Kreipke CW, Petrov T (2007) Alterations in cerebral cortex microvessels and the microcirculation in a rat model of traumatic brain injury: a correlative EM and laser Doppler flowmetry study. *Neurol Res* 29(4):339–347
- Schmidt EA, Czosnyka M, Matta BF, Gooskens I, Piechnik S, Pickard JD (2000) Non-invasive cerebral perfusion pressure (nCPP), evaluation of the monitoring methodology in head injured patients. *Acta Neurochir Suppl* 76:451–452
- Shen Y, Kou Z, Kreipke CW, Petrov T, Hu J, Haacke EM (2007) In vivo measurement of tissue damage, oxygen saturation changes and blood flow changes after experimental traumatic brain injury in rats using susceptibility weighted imaging. *Magn Reson Imaging* 25(2):219–227
- Soustiel JF, Mahamid E, Chistyakov A, Shik V, Benenson R, Zaaroor M (2006) Comparison of moderate hyperventilation and mannitol for control of intracranial pressure control in patients with severe traumatic brain injury – a study of cerebral blood flow and metabolism. *Acta Neurochir* 148:548–551
- Thomale UW, Kroppenstedt SN, Beyer TF, Schaser KD, Unterberg AW, Stover JF (2002) Temporal profile of cortical perfusion and microcirculation after controlled cortical impact injury in rats. *J Neurotrauma* 19:403–413
- Tong KA, Aswal S, Obenaus A, Nickerson JP, Kido D, Haacke EM (2008) Susceptibility-weighted MR imaging: a review of clinical applications in children. *Am J Neuroradiol* 29:9–17
- Willinger R, Ryan GA, Mclean AJ, Kopp CM (1994) Mechanisms of brain injury related to mathematical modeling and epidemiological data. *Accid Anal Prev* 26(6):767–779
- Wintermark M, Chioloro R, van Melle G, Revelly JP, Porchet F, Regli L, Meuli R, Schnyder P, Maeder P (2004) Relationship between brain perfusion computed tomography variables and cerebral perfusion pressure in severe head trauma patients. *Crit Care Med* 32(7):1579–1587
- Wintermark M, Sesay M, Barbier E, Borbely K, Dillon WP, Eastwood JD, Glenn TC, Grandin CB, Pedraza S, Soustiel J, Nariai T, Zaharchuk G, Caille J, Dousset V, Yonas H (2005) Comparative overview of brain perfusion imaging techniques. *Stroke* 36(9):83–99
- Wu Z, Li S, Lei J, An D, Haacke EM (2010) Evaluation of traumatic subarachnoid hemorrhage using susceptibility weighted imaging. *Am J Neuroradiol* 31(7):1302–1310
- Zaitzu Y, Kudo K, Terae S, Yazu R, Ishizaka K, Fujima N, Tha KK, Haacke EM, Sasaki M, Shirato H (2011) Mapping of cerebral oxygen extraction fraction changes with susceptibility weighted phase imaging. *Radiology* 261(3):930–936
- Zhang L, Bae J, Hardy WN, Monson KL, Manley GT, Goldsmith W, Yang KH, King AI (2002) Computational study of the contribution of the vasculature on the dynamic response of the brain. *Stapp Car Crash J* 46:145–164
- Zhao L, Nowak TS Jr (2006) CBF changes associated with focal ischemic preconditioning in the spontaneously hypertensive rat. *J Cereb Blood Flow Metab* 26(9):1128–1140
- Zwienenberg M, Muizelaar JP (2001) Cerebral perfusion and blood flow in neurotrauma. *Neurol Res* 23(2–3):167–174

Author Queries

Chapter No.: 4 0001544162

Queries	Details Required	Author's Response
AU1	The reference Haacke (2004) is not cited in text. Please check.	
AU2	Please update reference Haacke and Ye (2012).	

Uncorrected Proof

CHAPTER 2

Magnetic Resonance Imaging Biomarkers of Mild Traumatic Brain Injury

Z. KOU,^{*a} R. R. BENSON^b AND E. M. HAACKE^a

^a Departments of Biomedical Engineering and Radiology, Wayne State University School of Medicine, Detroit, Michigan 49098 USA;

^b Departments of Neurology and Radiology, Wayne State University School of Medicine, Detroit, Michigan

*Email: zhifeng_kou@yahoo.com

2.1 Introduction

Traumatic brain injury (TBI) affects 1.5 million Americans each year,^{1,2} the majority of which are mild TBI (mTBI).³ Today, more people who might have had more severe TBI or died in motor vehicle accidents suffer milder head injury, thanks to the advancements in motor vehicle safety. mTBI affects over 1 million Americans annually. It is a major public healthcare burden, yet has been overlooked for decades.^{1,2} Despite its name, the impact of mTBI on the patients and their family are not mild at all.³ mTBI patients typically develop a variable constellation of physical, cognitive, and emotional symptoms, collectively known as post-concussive syndrome (PCS), that significantly impact their quality of life. The direct cost of mTBI in the U.S. is approximately \$16.7 billion annually and this does not include the indirect costs to society and families.³⁻⁵

Up to 50% of patients with mTBI have persistent neurocognitive symptoms at three months and 5% to 15% at 1 year.^{6,7} Meanwhile, among the 1.8 million troops who have served in Iraq and Afghanistan, it is estimated that at least 20%

of returning troops have suffered at least one, and some multiple, concussions. This means up to 360 000 veterans may have brain injuries after discharge.⁸ However, most *symptomatic* mTBI patients have normal CT and conventional MRI scans,^{9,10} even with the greater sensitivity of MRI to TBI.¹¹ In addition to neuroimaging, clinical indices of severity, such as the Glasgow Coma Scale (GCS) and duration of post-traumatic amnesia (PTA) are lacking in sensitivity in mTBI and are not helpful in predicting outcome.¹² In summary, using currently available clinical instruments, it is difficult to determine which mTBI patients will have prolonged or even permanent neurocognitive symptoms.

With greater appreciation of incidence and impact of “civilian,” sports, and military mTBI, there is an increasing need to identify a minimally invasive biomarker (or biomarkers) of mTBI. A clinically useful biomarker or biomarkers should ideally be very sensitive to TBI (including mild cases) but should have reasonable specificity. That TBI pathology is not singular but involves multiple functional and structural changes affords greater opportunity for detection and characterization of injury with sensitive instruments. Similarly, biomarkers meeting these criteria should improve clinical trial efficiency since patients with similar types and grades of pathology could be grouped together in order to reduce the chances of a negative result due to prohibitive pathologic heterogeneity.

With both hardware and pulse sequence design advances, newer MRI methods have demonstrated the ability to detect and localize with high resolution *several* of the pathologic and pathophysiologic consequences of mTBI. These advanced MR technologies include susceptibility weighted imaging (SWI) for hemorrhage detection,¹³ MR spectroscopy (MRS) for metabolite measurement,¹⁴ diffusion weighted and diffusion tensor imaging (DWI/DTI) for edema quantification¹⁵ and axonal injury detection,¹⁶ perfusion weighted imaging (PWI) and arterial spin labeling (ASL) to measure blood flow to brain tissue,¹⁷ and functional MRI (fMRI), which measures changes in blood oxygen level locally in response to neuronal activity.¹⁸ Having a number of imaging biomarkers, all of which are obtained in a single scanning session (or multiple for longitudinal study) and are sensitive to different consequence of traumatic injury affords great advantages: 1) enhanced sensitivity; 2) ability to study inter-relationships among these biomarkers and between the biomarkers and clinical/neurocognitive deficits; 3) improved clinical management resulting from more precise characterization of injuries; and 4) enhanced power of clinical interventional studies (see above). Furthermore, the information comes “cheaply” since MRI is non-invasive and is widely available.

2.2 Search Criteria and Results

The purpose of this chapter is to review the current status and clinical impact of MR imaging findings in mTBI. BeLanger *et al.*¹⁹ provided an informative review on this topic in 2007. Since then many original works have been published.

The following inclusion criteria were used to identify potential papers: a) must be cited in Medline database; b) must use MRI as a major component of the study; c) only clinical (human) studies of mTBI patients; d) published in the

past five years (i.e. 2006 and later); and e) published in peer-reviewed English language journals. Readers interested in moderate to severe TBI imaging are encouraged to refer to another recent review paper, which covers SWI, DTI, and MRS.¹⁹

The authors conducted a Medline search at www.pubmed.com in September 2011 by using the search phrases “mild traumatic brain injury” and “magnetic resonance imaging.” There were a total 356 publications, of which 46 were reviews and 310 were original studies. After excluding articles that did not fit our criteria, we found a total 62 articles; 11 reviews and 51 original studies. Of original studies, 32 used structural imaging, DTI, MRS, and perfusion imaging and 19 articles used fMRI, including both resting state fMRI and task-oriented fMRI. This review focuses on clinical MRI, DTI, MRS, and perfusion imaging. The following was categorized according to the technical approaches being used. The literature is listed in Table 2.1.

2.3 Clinical CT and MRI

Although CT is still the first step in the search for large hemorrhages that may require surgical intervention, it is insensitive to small hemorrhages, whether from early contusion or from diffuse axonal injury. Most patients with mTBI have normal CT and conventional MRI findings. Indeed, they usually do not get clinical MRI scans in the emergency department, which sees the majority of patients with mTBI. Any intracranial abnormality would classify the patients as complicated mTBI,²⁰ which could have long-term sequelae similar to moderate TBI. A clinical radiological sequence protocol typically includes T1-weighted imaging for structural damage and brain atrophy, T2-weighted FLAIR for edema and acute stage subarachnoid hemorrhage, and T2* gradient recalled echo (GRE) for hemorrhages.

It would be of clinical value to know: “How many patients with mTBI have positive MRI findings?” and “How these findings may account for their neurocognitive or functional symptoms?” Regarding the prevalence of positive MRI findings in mTBI, different groups reported different findings. After reviewing 182 adolescent patients, Fay *et al.*²¹ reported 18% had positive MRI findings. Topal *et al.*²² reported that of 40 patients with mTBI, 12.5% had positive MRI. In contrast, Lee and colleagues²³ reported 50% with positive CT and 75% with positive MRI in 36 mTBI patients with both loss of consciousness and post-traumatic amnesia. The discrepancy among the figures could be due to the different study populations and different patient inclusion criteria.

Regarding the relationship between MRI findings and patient outcome, Muller *et al.*²⁴ reported that GCS < 14, CT/MRI positive, and S100B > 0.14, together, predicted impaired cognitive performance both at baseline and after 6 months. Kurca *et al.*²⁵ reported that patients with mTBI with true traumatic MRI lesions are different neuropsychologically from those of mTBI with non-specific MR lesions, and neurocognitive and symptom signs have organic bases that can be detected by MRI. Fay *et al.*²¹ reported that ratings of PCS in

Table 2.1 Summary of literature search result.

First author and year	Imaging approach	Number of patients	Inclusion criteria	Imaging stage	Analytical approach	Major findings
Clinical MRI Fay 2010 ²¹	Clinical MRI (T1, T2, and FLAIR)	182 children	LOC or GCS<15 or 2+ PCS symptoms	Acute	Clinical radiological diagnosis	18% with positive MRI finding (complicated mTBI); ratings of PCS were moderated by both cognitive ability and injury severity; children with lower cognitive ability with cmTBI were prone to PCS
Muller 2009 ²⁴	Clinical MRI, serum S-100B, ApoE	59 mTBI			Clinical radiological diagnosis	GCS<14, CT/MRI + and S100B>0.14 predicted impaired cognitive performance both at baseline and after 6 months; ApoE allele predicted less recovery of cognitive function after mTBI
Lee 2008 ²³	CT and clinical MRI	36 mTBI	Both LOC and PTA	Acute CT, subacute MRI (in 2 weeks)	Clinical radiological diagnosis	CT detected 50% with abnormality; MRI detected 75% with abnormalities. CT and MR finding did not account for cognitive impairment
Topel 2008 ²²	CT and clinical MRI	40 mTBI	Normal CT, GCS 13–15	Acute (within 24 hours)	Clinical radiological diagnosis	12.5% patients had MR abnormality, 10% with hemorrhagic lesion on T2 GRE, and 12.5% with high intensity on FLAIR and DW sequences
Lewine 2007 ¹⁰¹	MEG, SPECT, and MRI	30 mTBI, retrospective review	GCS 13–15 and LOC<20 min	subacute (Weeks after TBI)	Clinical radiological diagnosis	MEG is more sensitive to brain injury and correlated with memory and attention problems
Kurca 2006 ²⁵	MRI	30 mTBI	WHO definition: GCS 13–15, LOC, PTA or mental status change	Acute (≤4 days)	Clinical radiological diagnosis	mTBI patients with true traumatic MRI lesions are different neuropsychologically from mTBI with non-specific MR lesions; neurocognitive and symptom signs have real organic basis, which can be detected by MRI

1
5
10
15
20
25
30
35
40
45

Inglese 2006 ¹⁰²	MRI	38 mTBI	Acute and chronic	Clinical radiological diagnosis	Average number of Virchow Robin Space was significantly higher in mTBI patients than in controls. VRS was not associated with neurocognitive findings	1
Perfusion imaging Ge 2009 ⁶¹	ASL perfusion	21 mTBI	Chronic	ROI on thalamus	Reduced CBF in both sides of thalamus, in correlation with speed of information processing, memory, verbal, and executive function	5
MR spectroscopy imaging Kirov 2007 ⁶⁵	2D MRSI	20 mTBI	Chronic	Mixed model regression, LCModel	mTBI had more variations in NAA, Cre and Cho than controls	10
Cohen 2007 ⁸⁶	MRS, MRI	N = 20 mTBI	Acute and chronic	Single voxel MRS, T1 volumetry	Whole brain NAA decreased by 12%; mTBI patients had global and GM atrophy	15
Yeo 2011 ¹⁰³	MRSI	N = 30 mTBI	Subacute (within 21 days)	MRSI, LC model	Cre and Glx increase at WM and Glx decrease at GM at subacute stage; GM Glx normalized and WM Cre and Glx tend to normalize at 4 months after injury	20
Govind 2010 ⁹¹	3D MRSI	N = 20 mTBI, 9 moderate TBI	Subacute (mean 21 days)	3D MRSI	Widespread decrease of NAA and NAA/Cre, and increases of Cho and Cho/NAA in whole brain, and with the largest differences in WM; negative correlations between Cho/NAA with neurocognitive score in the frontal lobe; no significant correlations between any MRSI or neuropsychological measures and the GCS	25

Table 2.1 (Continued)

First author and year	Imaging approach	Number of patients	Inclusion criteria	Imaging stage	Analytical approach	Major findings
Diffusion imaging						
Grossman 2011 ⁶⁰	Diffusion Kurtosis imaging (DKI)	22 mTBI	ACRM	Subacute to chronic	Diffusion Kurtosis analysis	Changed DTI and DKI measures in thalamus and IC, and CC and centrum semiovale in more chronic patients; cognitive impairment associated with mean kurtosis in thalamus and IC
MacDonald 2011 ⁶³	DTI	N = 63/21, Service personnel	LRMC ¹¹⁹	Subacute	ROI	Abnormalities in the middle cerebellar peduncles, cingulum bundles, and in the right orbitofrontal white matter
Cubon 2011 ⁴⁸	DTI	10 college Sports concussion	No LOC, symptom based diagnosis	Chronic	TBSS	MD increase in left WM fibre tracts, IC, and thalamic acoustic radiations
Sponheim 2011 ⁶⁴	EEG and DTI	9 blast-mTBI soldiers	ACRM, definition	N/A	ROI of ICBM atlas	Diminished interhemispheric coordination of brain activity; EEG Phase synchrony associated with FA in frontal WM
Messe 2011 ⁴⁵	DTI	23 mTBI	ACRM	Subacute	TBSS	MD increase associated with patients' outcome
Holli 2010 ^{104,105}	Structural MRI, DTI	42 mTBI	WHO definition on mTBI ¹²²	Subacute, (3 weeks)	ROI Texture analysis of MRI, DTI ROI	Textural differences between left and right hemispheres; Texture parameters in mesencephalon and genu of cc correlate with memory; texture parameters in mesencephalon correlated with DTI FA and ADC
Mathew 2011 ⁶⁵	fMRI, DTI	11 bTBI with major depression disorder	LOC or change of mental status during interview	Chronic	Face matching fMRI, DTI VBA	Hyperactivity in amygdala and other emotional processing structure; Low FA in SLF; depression symptoms correlated with FA in SLF

1
5
10
15
20
25
30
35
40
45

Mayer 2010 ⁴²	DTI	22 mTBI	ACRM	Subacute (12 days)	ICBM atlas ROI	Normal structural imaging, FA increase, reduced radial diffusivity in CC and left hemisphere tracts	1
Chu 2010 ³⁸	DTI	10 adolescents	Normal CT, GCS 15, brief LOC	Acute (1–6 days post)	VBA	Increase FA, reduced ADC, and reduced radial diffusivity in WM regions and in left thalamus	5
Wu 2010 ³⁹	DTI	12 adolescents	Brief LOC	Acute (1–6 days)	ROI	Lower ADC than controls; FA increase of left cingulum bundle correlated with delayed recall	10
Lipton 2009 ⁴⁶	DTI	20 mTBI	LOC < 20 min, PTA < 24 hours, GCS ≤ 15, not neurologic deficit	2–24 days	VBA	FA reduced in WM of dorsolateral prefrontal cortex (DLPFC), correlated with worse executive function; MD increased in several clusters of WM; FA increase in the posterior limb of IC bilaterally	15
Lo 2009 ⁴⁹	DTI	10 mTBI with persistent cognitive symptoms		Chronic	ROI	Reduced FA and increased ADC at the left side of CC genu. FA increased in IC bilaterally	20
Lipton 2008 ⁸²	DTI	17 mTBI with persistent cognitive impairment	LOC < 20 min, PTA < 24 hours, GCS ≤ 15, not neurologic deficit	Chronic	Whole brain histogram; VBA	Histogram of WM FA shift to lower end; Reduced FA and increased mean diffusivity in CC, subcortical WM, and IC bilaterally	25
Niogi 2008 ⁶²	DTI	43 mTBI	LOC and PTA	Chronic	ROI	Reduced FA in left anterior corona radiata in correlation with attentional control, and reduced FA in uncinate fasciculus in correlation with memory performance	30
Wilde 2008 ⁴⁰	DTI, SWI	10 adolescents	Normal CT, GCS = 15, brief LOC	Acute (1–6 days post)	ROI on CC	One patient with SWI bleed; increased FA and decreased ADC and MD in CC, in correlation with PCS score	35
							40
							45

Table 2.1 (Continued)

First author and year	Imaging approach	Number of patients	Inclusion criteria	Imaging stage	Analytical approach	Major findings
Niogi 2008 ⁵⁰	DTI, T2* GRE	34 mTBI with persistent symptoms	GCS 13–15, LOC and PTA; 1 + symptom at time of imaging	Subacute to Chronic	ROI on major WM tracts	FA decreased in several WM regions: anterior corona radiata, uncinate fasciculus, cc genu, cingulum bundle; number of damaged WM regions correlated with reaction time.
Miles 2008 ⁴⁷	DTI	17 mTBI		Subacute	ROI	Increased MD and reduced FA in mTBI patients; baseline MD tend to correlate with response speed.
Rutgers 2008 ⁶⁶	DTI fibre tracking	21 mTBI	Clinical diagnosis	Chronic	VBA	Patients had multiple WM regions with reduced FA; 19.3% fiber bundles show discontinuity on fiber tracking
Bazarian 2007 ⁴¹	DTI	6 mTBI/6 orthopedic injury controls	ACRM	Acute (within 72 hours)	VBA and ROI	mTBI with lower mean trace in left anterior IC and higher FA in posterior CC. FA values correlated with 72-hour PCS score and neurobehavioral tests (visual motor speed and impulse control)
Inglese 2005 ⁴³	DTI	N = 46 mTBI		20 acute and 26 chronic	Whole brain histogram, and ROI	Reduced FA in patients' CC, IC, and centrum semiovale. Increased MD in cc and IC. No group difference

Abbreviations: ACRM, American Congress of Rehabilitation Medicine; ADC, apparent diffusion coefficient; ASL, arterial spin labeling; CBF, cerebral blood flow; CC, corpus callosum; CT, computed tomography; DKI, diffusion kurtosis imaging; FA, fractional anisotropy; FLAIR, fluid attenuated inversion recovery; fMRI, functional MRI; GCS, Glasgow Coma Scale; GM, grey matter; IC, internal capsule; ICBM, International Consortium of Brain Mapping; LRMIC, Landstuhl Regional Medical Centre; MD, mean diffusivity; MEG, magnetic encephalography; MRI, magnetic resonance imaging; PCS, post-concussive syndrome; PTA, post-traumatic amnesia; ROI, region of interest; SLF, superior longitudinal fasciculus; SPECT, single-photon emission computed tomography; TBSS, tract-based spatial statistics; THA, thalamus; VBA, voxel-based analysis; VRS, Virchow Robin Space; WHO, World Health Organization; WM, white matter.

1
5
10
15
20
25
30
35
40
45

adolescents were moderated by both cognitive ability and injury severity. Children with lower cognitive ability with complicated mTBI were prone to PCS. Comparatively, Lee *et al.*²³ reported that CT and MRI findings were not associated with a patient's neurocognitive impairment. Clearly, the seemingly conflicting findings on the predictive role of structural MRI need further investigation.

2.3.1 Susceptibility Weighted Imaging (SWI) of Hemorrhagic Lesions

In diagnostic radiology, intracranial hemorrhage has been sought as a biomarker of TBI. Some investigators have suggested that the presence of hemorrhage in DAI is predictive of poor outcome in moderate to severe TBI. SWI was developed by Haacke *et al.*²⁷ as a high resolution venography method. It has been used to evaluate moderate to severe TBI patients since 2003 by Tong *et al.*,¹³ who have shown that SWI is 3 to 6 times more sensitive than conventional T2* gradient echo imaging (GRE) for detecting suspected DAI lesions in children.^{13,28} SWI has been shown to detect tiny hemorrhages that may be the only abnormal finding that can confirm the presence of brain injury, and change management of the patient. In addition, lesion number and volume identified by SWI are negatively associated with patient outcome²⁸ and neuropsychological functions²⁹ in patients with moderate to severe injury.

After brain injury, the hemorrhagic bleed may undergo a temporal transformation from oxyhemoglobin and then deoxyhemoglobin in the acute stage; intra- and then extracellular methemoglobin in the subacute stage; and finally, hemosiderin in the chronic stage.^{30–32} SWI is sensitive to deoxyhemoglobin in the acute stage and extracellular methemoglobin in the subacute stage and hemosiderin in the chronic stage.³⁰ Therefore, positive results with SWI should provide a biomarker for hemorrhagic brain injury at any stage. However, very few data have been reported regarding the possible role of SWI in an improved detection of microhemorrhages and its predictive value of patient outcome in mTBI. Unlike DTI, which requires complex post-processing and comparison with proper controls, SWI hemorrhage is readily available for radiological reading immediately after MRI scans. This makes SWI more likely to have a direct impact on the radiological diagnosis. Furthermore, with quantitative susceptibility mapping, the hemorrhagic lesion load could be more acutely mapped through next generation SWI analysis and potentially improve the prediction of a patient's outcome. Figure 2.1 demonstrates an exemplary case to show the SWI detection of brain hemorrhages in mTBI in the acute stage in comparison with the usual clinical T2* GRE.

In summary, there is still a need to evaluate a large number of patients with mTBI by using structural imaging, particularly SWI, to see the clinical value of intracranial hemorrhage detected by MRI. This should be done along with other clinical measures, e.g. GCS, as well as other biological markers, such as serum biomarkers.

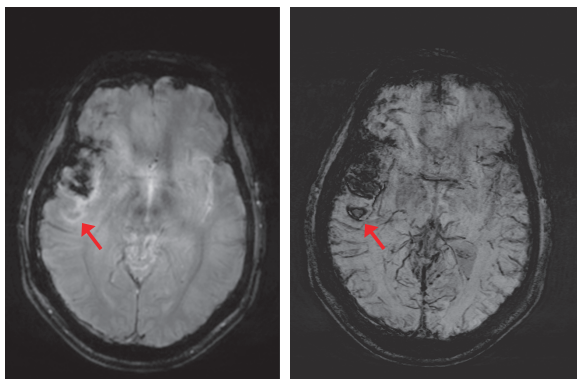


Figure 2.1 Comparison of T2* with SWI on the detection of hemorrhagic lesions. Image order: T2* GRE (left) and SWI (right). A 45-year-old man fell down a staircase and then visited ER with severe headache. Both T2* GRE and SWI detected hemorrhages on the right side of inferior temporal lobe. However, in a small area with mixed blood and edema signal, T2* GRE only detects edema (bright signal) and SWI detects hemorrhage (dark signal) (see arrows).

2.4 Diffusion Tensor Imaging (DTI) of Axonal Injury

Diffusion imaging sequences are sensitive to traumatic axonal injury (TAI) secondary to stretch and shear forces. DTI measures the bulk motion of water molecular diffusion in biological tissues. It is most useful when tissues are anisotropic, i.e. when diffusion is not equivalent in all directions, such as in skeletal muscle or axons in white matter of the central nervous system. Histological correlates have validated DTI's sensitivity to brain injury for both focal³³ and diffuse axonal injury³⁴ models. The apparent diffusion coefficient (ADC) and fractional anisotropy (FA)^{35,36} are two parameters derived from DTI that have been extensively studied in TBI. ADC is an estimate of the average *magnitude* of water movement in a voxel (regardless of direction), while FA is an index of the *directional non-uniformity*, or anisotropy, of water diffusion within a voxel.

FA has been used to detect alterations in directional diffusion resulting from tissue damage. FA in white matter is highest when fibers are long (relative to voxel dimension) and oriented uniformly (collinear) within a voxel and lowest when fibers are not collinear (e.g. "crossing fibers") or have been damaged. When axons are injured, as in acceleration/deceleration injuries (such as MVCs), diffusion anisotropy typically decreases. Loss of diffusion anisotropy is the result of a number of axonal changes after injury including: 1) increased permeability of the axonal membrane; 2) swelling of axons; 3) decreased diffusion in the axial (long axis) direction; 4) degeneration and loss of axons in the chronic stage. In general, any pathological alteration of white matter fibers will result in FA decrease, since one or more of these axonal changes occurs in disorders of white matter. Not surprisingly, most clinical studies of moderate and severe TBI have shown FA to be more sensitive than ADC to traumatic injury. On the other

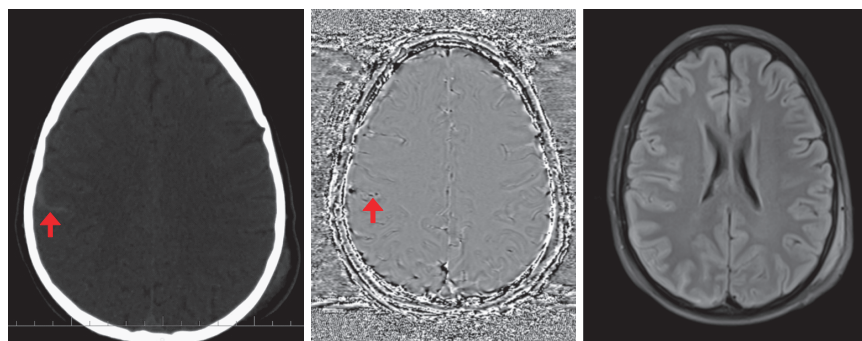


Figure 2.2 SWI detects subarachnoid hemorrhage (SAH) in an acute mTBI case. Image order from left to right: CT, SWI phase, and T2 FLAIR. A 21-year-old man fell from a 15-foot (4.5 m) high ladder. Both CT and SWI phase detected sub-arachnoid hemorrhage (see arrows) at the acute stage, while F2 FLAIR failed to detect.

hand, ADC, FA, and directionally selective diffusivities (principal, intermediate, and minor components of diffusion) can help to better characterize brain injury pathologies. Trace and mean diffusivity are two other measurements similar to ADC and vary similarly. Changes in FA in association with ADC changes can differentiate the type of edema. For example, in the acute stage, decreased FA in association with increased ADC suggests vasogenic edema, while increased FA in association with decreased ADC suggests cytotoxic edema. Decreased FA in association with decreased ADC and decreased longitudinal (parallel to the long axis of the axons) water diffusivity suggests axonal transport failure as occurs in degenerative neurological diseases such as in ALS.

Regarding the location of brain lesions detected by DTI, Niogi *et al.*³⁷ summarized that the frontal association pathways, including anterior corona radiata, uncinate fasciculus, superior longitudinal fasciculus, and genu of corpus callosum (CC), were the mostly frequently injured WM structures in this cohort of mTBI patients. Single subject results were not reported but it can be assumed that significant inter-individual variability for location and extent of WM injury exists due to varying injury mechanisms (and forces) and biological (neural and non-neural) differences across patients.

2.4.1 Imaging at Different Pathological Stages

Interestingly, despite the higher incidence of milder TBI compared with more severe TBI in Western countries, there are many fewer mTBI imaging studies reported in the literature. One reason is the fact that recruitment of patients with mTBI is more difficult, since they are typically outpatients. Another reason is the common conception that mTBI is a transient problem from which virtually all who are afflicted will recover fully. Therefore, some question the clinical importance of studying mTBI. Certainly, insurance reimbursement for MRI scanning of mTBI is rare and even rarer in the acute setting, so that “adding on

research sequences” is not possible. With these limitations in mind, a growing literature on DTI in TBI has begun to address the DTI findings at different stages.

2.4.1.1 Acute Stage

There are conflicting findings for FA and ADC in mTBI. Chu *et al.*,³⁸ Wu *et al.*,³⁹ and Wilde *et al.*⁴⁰ from Baylor College of Medicine scanned 10 to 12 adolescents with mTBI within 6 days of injury and reported *increased FA*, *reduced ADC* and *reduced radial (short axis) diffusivity* in WM regions and left thalamus. Similarly, Bazarian *et al.*⁴¹ studied six mTBI patients within 72 hours and reported *increased FA* in the posterior CC and *reduced ADC* in the anterior limb of the internal capsule (IC). Similar to Chu *et al.*,³⁸ and Wilde *et al.*,³⁹ Mayer *et al.*⁴² studied 22 patients with mTBI within 12 days of injury and reported *FA increase* and *reduced radial diffusivity* in the CC and left hemisphere tracts.

Inglese *et al.*,⁴³ in contradiction to Chu *et al.*,³⁸ Wilde *et al.*,^{39,40} Bazarian *et al.*,⁴¹ and Mayer *et al.*,⁴² found *reduced FA* in the splenium of CC and posterior limb of IC in 20 patients with mTBI imaged up to 10 days after injury (mean = 4 days). Manually drawn regions of interest were used to assay the genu and splenium of the CC, the centrum semiovale, and the posterior limb IC bilaterally. In the same line as Inglese *et al.*, Arfanakis and colleagues⁴⁴ studied a handful of patients with mTBI at the acute stage and reported FA decrease in major WM tracts.

2.4.1.2 Subacute Stage

All studies reported *reduced FA* and/or *increased diffusivity*; i.e. ADC, trace or mean diffusivity (MD), at this stage. Messe *et al.*⁴⁵ studied 23 mTBI at the subacute stage and found significantly *increased MD* in mTBI patients with poor outcome.⁴⁵ The authors did not find significant changes of FA values. Lipton *et al.*⁴⁶ scanned 20 mTBI patients in the subacute stage and demonstrated *reduced FA* and *increased MD* in frontal subcortical WM. Miles *et al.*⁴⁷ studied 17 acute and subacute mTBI patients and found *reduced FA* and *increased MD*. All of these studies at the subacute stage reported a similar profile of DTI measures except for different locations of injury.

2.4.1.3 Chronic Stage

Three studies report either *reduced FA* or *increased diffusivity* or both. Cubon *et al.*⁴⁸ studied 10 collegiate athletes with concussion at the chronic stage and found MD increase in left WM tracts, internal capsule, and thalamic acoustic radiations. Lo *et al.* studied 10 mTBI patients and reported *reduced FA* and *increased ADC* in the left genu of the CC and *increased FA* in internal capsule bilaterally.⁴⁹ Niogi *et al.*⁵⁰ studied 43 patients with chronic mTBI and reported *reduced FA* in a large number of WM tracts.

All DTI studies of moderate to severe TBI patients^{16,51–53} and subacute/chronic mTBI patients^{43,50,54–56} report FA *decreases*, which are correlated with clinical or neuropsychological measures. However, there are seemingly

contradictory findings in mTBI in the acute stage (within 1 week after injury) in the literature: Inglesse⁴³ and Arfanakis⁴⁴ both reported FA *decreases*, while Wilde⁴⁰ and Bazarian⁴¹ reported FA *increases* and decreased radial diffusivity. It has been suggested that increased FA *acutely* may reflect cytotoxic edema,⁴⁰ which would shunt extracellular fluid into swollen cells. This could have the effect of reducing inter-axonal free water and therefore increasing anisotropy.

2.4.1.4 Longitudinal Studies

Only a few investigators have followed FA over time in the *same* patients. Sidaros *et al.*⁵⁷ studied 23 patients with severe TBI at 8 weeks and again at 12 months and found that partial recovery of initially depressed FA values in the internal capsule and centrum semiovale predicted a favorable outcome. Kumar *et al.*⁵⁸ studied 16 patients with moderate to severe TBI at 2 weeks or less, 6 months, and 2 years and found persistently reduced FA except in the genu of the corpus callosum, where there was partial normalization by 2 years. Recently, two studies by Mayer *et al.*⁴² and Rutgers *et al.*⁵⁵ reported that FA may partially normalize, reflecting recovery. This evidence suggests that a systematic investigation of a large number of patients with mTBI at acute, subacute, and chronic stages is warranted to reveal the evolution of pathophysiology in mTBI.

2.4.2 Correlation Between DTI-Derived WM Injury Topography and Neuropsychological Deficits

Patients with mTBI often develop a constellation of physical, cognitive, and emotional symptoms that are collectively known as post-concussion syndrome (PCS). In terms of neurocognitive symptoms, there are four key domains implicated in chronic neuropsychological impairment after mTBI. These domains include: 1) higher-order attention, 2) executive function, 3) episodic memory, and 4) speed of information processing. To date, several studies have demonstrated typical mTBI cognitive profiles and association with DTI findings. Niogi *et al.* summarized the topographic and neurocognitive deficits.³⁷

Damage to the frontal WM has been reported to be associated with impaired executive function. Lipton *et al.*⁴⁶ studied 20 acute to subacute patients and reported that reduced FA in WM of dorsolateral prefrontal cortex (DLPFC) is correlated with worse executive function. Frontal WM injury is also associated with attention deficit. Niogi *et al.*⁵⁰ reported that reduced FA in the left anterior corona radiata is correlated with attention control in chronic mTBI patients.

Injury at the temporal WM tracts or cingulum bundle may cause memory problems. Niogi *et al.* reported that reduced FA in uncinate fasciculus correlated with memory performance.⁵⁹ Wu *et al.*³⁹ reported that FA measure of left cingulum bundle correlated with delayed recall.

Injury of the callosal fibers has been reported to be associated with PCS scores. Wilde *et al.*⁴⁰ studied 10 adolescent patients with mTBI in the acute stage and reported that increased FA and decreased ADC and MD in corpus callosum is correlated with patient PCS score. Bazarian *et al.*⁴¹ studied 6

patients with mTBI in the acute stage and reported a lower mean trace in the left anterior IC and a higher FA in the posterior CC. FA values correlated with patient's 72 hours PCS score and visual motor speed and impulse control.

The overall burden or extent of WM injury is associated with both speed of information processing and overall functional outcome. Niogi *et al.*⁵⁰ studied 34 subacute to chronic mTBI patients and reported that FA decreased in several WM regions, including anterior corona radiata, uncinate fasciculus, CC genu, and cingulum bundle. They demonstrated that the number of damaged WM regions is correlated with patient's reaction time. Miles *et al.*⁴⁷ studied 17 mTBI patients at the acute stage and followed them up to 6 months after injury. They reported that, at the acute stage, the increased mean diffusivity (MD) in centra semiovale, the genu and splenium of CC, and the posterior limb of IC tended to correlate with patient response speed at 6 months after injury. Regarding the overall outcome, Messe *et al.*⁴⁵ divided patients with mTBI into two outcome groups, poor outcome versus good outcome. Poor outcome patients showed significantly higher mean diffusivity (MD) values than both controls and good outcome patients in the corpus callosum, the right anterior thalamic radiations and the superior longitudinal fasciculus, the inferior longitudinal fasciculus and the fronto-occipital fasciculus bilaterally.

Interestingly, injury or reduced blood supply in the thalamus, which is the relay station of neuronal pathways, may cause a constellation of symptoms in speed of information processing, memory, verbal, and executive function. Grossman *et al.* studied 22 patients with subacute to chronic mTBI by using diffusion kurtosis imaging, which is a more advanced form of diffusion analysis, and demonstrated that overall cognitive impairment is associated with the diffusion measurement in the thalamus and internal capsule.⁶⁰ This work is along the same line of a perfusion study by the same group, which demonstrated that reduced blood flow in the thalamus correlated with patient's overall neurocognitive function.⁶¹

In summary, significant progress has been made by researchers in recent years regarding the prognostic value of DTI in the form of FA for neurocognitive outcome in patients with mTBI. There is still a need to evaluate the neural basis of a patient's recovery process, which requires longitudinal studies over a large number of patients.

2.4.3 Pros and Cons of Different Analytical Approaches

One challenge of DTI is post-processing and interpretation of the images. There are several approaches available, including whole brain histogram analysis, region of interest analysis, voxel-based analysis, and tract-based spatial statistics, to name a few. Each approach has pros and cons. There is no standardized procedure for DTI analysis; it is a moving target. The choice of analytical approach depends on the hypothesis and goal of the study. Table 2.2 lists the pros and cons of each approach.

A whole brain histogram analysis is used to segment out the whole brain WM and plot the FA frequency distribution.¹⁶ Two studies have demonstrated

Table 2.2 Comparison of different DTI analytical approaches.

Approach	Pros	Cons
Whole brain histogram	Easy to implement	Not sensitive to subtle changes of mild brain injury; lack of regional injury information
Manual ROI	Easy to implement, detect regional injury	Inter-rater and intra-rater variability issue; time consuming
Automated or semi-automated ROI	Objective, consistent, detect regional injury	Normalization may distort DTI indices; potential misregistration issue; small fraction of voxels may be averaged out
Voxel-based analysis	Data driven, automated, objective	Warping may cause DTI indices' change; misregistration cause artificial edging effect
Tract based spatial statistics	Data driven, automated, objective, least mis-registration issue.	Only look at the center line of WM tracts; may miss the target of lesions at other areas of WM

DTI, diffusion tensor imaging; ROI, region of interest; WM, white matter.

that moderate to severe TBI patients had their FA histograms shifted toward zero,^{16,51} and the TBI group had larger variations than controls. In a mTBI study, Inglese *et al.*⁴³ did a whole brain histogram analysis by combining both grey and white matter, and did not find a group difference between mTBI patients and controls. Instead of combining both GM and WM, Lipton *et al.*⁶² segmented out WM and demonstrated the mTBI patient group's FA histogram of WM only shifted to lower end. However, as their data demonstrated, it is not as sensitive as that of the voxel-based analysis. The advantage of the histogram analysis is that it is relatively easy to implement. The disadvantage is the lack of regional injury information and lack of sensitivity to subtle changes of the WM, particularly for mild cases. Unless the subject has widespread multifocal injury on WM tracts, a small fraction of WM injury may not demonstrate a shift in the histogram or change its kurtosis.

To test a hypothesis of injury at specific WM tract(s) in association with specific domain of neurocognitive or neural behavioral symptoms, researchers used region of interest (ROI) analysis by either manually drawing^{41,43,44,47,49,50,59,63} or segmenting out the regions in a prior defined template in an automated or semi-automated way.^{42,64} This could also provide needed lesion localization information, which should improve biomechanical models of TBI. Manually drawn ROI is relatively easy and convenient to do. One could use a color-encoded FA diffusion map as a guide to define the boundary of a target region. It works on the native space of the subject's brain without worrying about the distortion caused by the warping algorithm. However, it is time consuming and error prone. It requires the rater's prior knowledge of which specific tracts or locations to define the region. It also has a potential inter-rater and intra-rater variability problem.

An automated ROI analysis approach would need initially to transform the images into a standard reference space; for example, International Consortium

of Brain Mapping (ICBM) atlas, by using SPM8, FSL, or other software, in order to derive statistical maps computed from comparing “cases” and non-TBI controls, and then further divide the WM into standardized regions that are already defined on the atlas. Then each regional FA, ADC, or Eigen values could be computed. In this category, several studies reported significant FA differences between mTBI patients and controls.^{42,64} This method overcomes the subjective issue in manually drawn ROIs by using a computer algorithm to warp each subject to a standard space. The result is objective and consistent. However, the use of a computer algorithm for image warping and registration will introduce new problems. Due to individual variations, the warping of one image to a standard space could change the DTI indices’ values from the native space. Furthermore, in a relatively large region like the splenium of corpus callosum, a small fraction of voxels with abnormal FA value could be averaged out by the surrounding voxels in the same region, rendering this method insensitive to small lesions.

Voxel-based analysis (VBA) overcomes the sensitivity issue of the ROI approach by comparing patient and control DTI images voxel by voxel to determine the abnormal voxels between groups. This approach is fully automated, data-driven, and reproducible. Several studies reported different clusters of WM tracts with abnormal FA values by using this method.^{38,41,46,62,65,66} However, it suffers from the same warping and misregistration problems as that of the automated ROI approach. Particularly at the edge of WM or GM/WM junction area, any misregistration will result in comparing WM of one group with GM of another group and result in abnormal values of DTI indices.

To overcome the misregistration problem, a relatively new approach, called tract-based spatial statistics (TBSS), has been introduced.⁶⁷ First, it averages both patient and control brains to form a template brain. Second, it defines a template skeleton of the WM tracts from the center lines of WM of the template

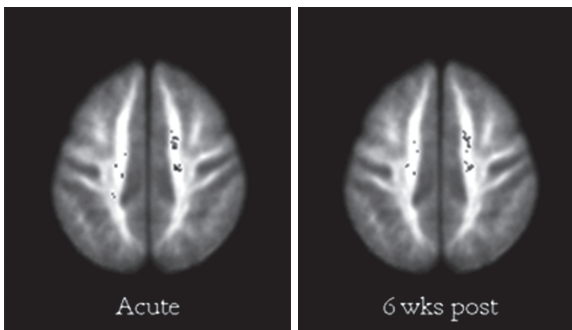


Figure 2.3 A mTBI patient scanned on the day of injury (5.5 hours after injury) and 6 weeks later. A 31-year-old male fell 10 feet (3.0 m) off a ladder, striking the back of his head with brief loss of consciousness and confusion. The patient developed persistent mild cognitive symptoms 6 weeks after injury. Note the same location of reduced FA in left corona radiata. Similar finding in splenium of CC (not shown). Global WM FA mean was within normal.

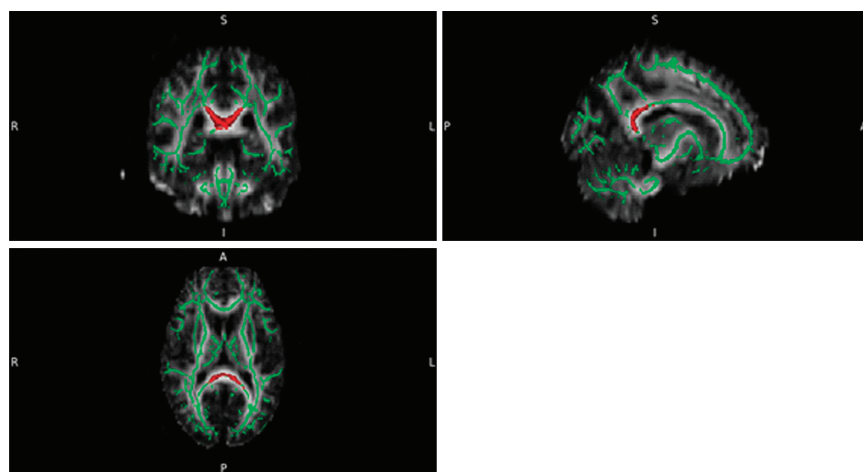


Figure 2.4 A demonstration of TBSS analysis to detect WM injury at the splenium of corpus callosum. A young man involved in a motor vehicle accident with negative structural MR images. TBSS analysis demonstrated significantly lower FA values at the splenium of corpus callosum, as demonstrated in the highlighted area. As shown on the image, it focuses on the skeleton (center lines) of WM.

brain. Third, all of the subjects' WM skeletons are nonlinearly registered onto the template skeleton. As such, the WM skeletons of all subjects will be aligned at the same space. Abnormal DTI indices could be defined along the skeletons by using a group comparison on a voxel-based analysis. Two groups reported the use of this method in the detection of mTBI^{45,48} in association with patient outcome. This method is automated and reproducible and suitable for data-driven analysis. It has the least problem of misregistration. However, it only looks at the center lines of WM tracts. In thick WM bundles, like corpus callosum, it might miss lesions located off the center lines of WM.

AQ6

2.4.4 DTI Caveat

In addition to the post-processing concerns mentioned above, another caveat of DTI is that it is experiment dependent. Different magnet field strength and image acquisition parameters, among others, will result in different DTI measures.¹⁹ Furthermore, to date, most publications are performed with group comparisons between patients and controls instead of an individual-based analysis. However, radiological diagnosis is case-based. A radiologist or a clinician needs to make a decision for each individual subject instead of group comparison. The low sensitivity of DTI to individual case hinders its further implementation as a routine clinical sequence. A relatively standardized protocol is needed to test a large number of controls to determine the normal variations before deciding which specific case has brain injury.

2.5 *In Vivo* ^1H MR Spectroscopic Imaging

Cellular changes to neurons and glia following TBI are complex and dynamic. Proton (^1H) MRSI has the advantage of measuring brain metabolism *in vivo*, and is able to detect various biochemical processes of brain injury such as the loss (or dysfunction) of neuronal cells. TBI is known to induce changes in *N*-acetylaspartate (NAA) (a neuronal marker), choline (Cho) (a marker for membrane disruption, synthesis, or repair), and lactate (Lac) (a measure of anaerobic glycolysis).⁶⁸ Many studies of metabolic changes after TBI have proven MRS to be a sensitive tool to predict neurologic,^{69–74} cognitive,^{75–79} and functional outcome.⁸⁰ Significant decreases of NAA and increases of Cho have been observed in “normal appearing” WM or GM following moderate to severe TBI.^{74–76,81–83} Elevated Cho may be detected in WM as a breakdown product after shearing of myelin⁸⁴ and the presence of lactate in the brain suggests hypoxic/ischemic injury. Researchers from Loma Linda University Medical Center found that increased frontal white matter (FWM) Cho/creatine and decreased FWM NAA/Cho at acute stage are useful for predicting functional outcome in patients with moderate to severe TBI. In addition, they also found that elevated Glx and Cho in the acute stage are sensitive indicators of injury and predictors of poor outcome in *normal appearing brain* of severe TBI patients.⁷¹ They also found that the decrease of NAA at subacute stage is more predictive of patient outcome.

In mTBI studies, there are relatively less data reported in comparison with moderate to severe TBI studies. For a chronic mTBI study, Kirov *et al.*⁸⁵ scanned 20 mTBI patients and 17 age- and gender-matched controls and reported that the mTBI group had more variations in NAA, Cre, and Cho than the control group. Cohen *et al.*⁸⁶ investigated 20 patients with mTBI from 9 days to years after injury and found that whole brain NAA decreased by 12% along with significant global and grey matter atrophy, in comparison with 19 controls. This further demonstrates NAA as a biomarker of neuronal injury or cellular loss. Regarding the investigations of mTBI in the subacute or semi-acute stages, a few studies reported an NAA/Cr decrease,^{86–88} which is suggestive of neuronal loss.

A recent study on 10 patients with mTBI in the semi-acute stage showed creatine increases in white matter and Glx (glutamate and glutamine) decreases in grey matter. The creatine (Cre) increases in white matter were correlated with patient’s executive function.⁸⁹ The same research group also studied a relatively larger group of patients with longitudinal follow-up. In their study of 30 mTBI patients at the first visit within 3 weeks after injury, they reported Cre and Glx increases in WM and Glx decreases in GM.⁹⁰ Among the patients, 17 returned for follow-up at the chronic stage; their GM Glx demonstrated normalization and their WM Cre and Glx demonstrated a trend of normalization. Of particular note is that, at the first visit, the mTBI group did not have any difference from the controls in neuropsychological assessment except for more somatic, cognitive, and emotional symptoms.⁹⁰ This demonstrates that MRS may be sensitive to subtle changes of the brain, which may not yet be manifesting significant neural cognitive deficits.

As with other MRI techniques, MR spectroscopy has also undergone tremendous advancements in the past two decades, evolving from single voxel MR spectroscopy to 2D spectroscopy imaging and 3D whole brain spectroscopy imaging. Single voxel spectroscopy (SVS) allows acquisition of a single spectrum from one volume element (voxel) typically 8 cm³ or more, whereas 2D or 3D magnetic resonance spectroscopic imaging (2D-MRSI/3D-MRSI), also called chemical shift imaging (CSI), allows for the simultaneous acquisition of multiple spectra from smaller adjacent voxels through multiple sections of the brain. MRSI has an inherent advantage over SVS because it is better able to evaluate regional distributions of neurochemical alterations. Instead of hypothesizing a certain region or certain slice of the brain to have abnormal metabolite signals; 3D MRSI allows investigators to search the whole brain to identify any area that might have abnormal metabolites. This could be useful in mTBI due to the fact that choosing an arbitrary region to study would be like searching for a needle in a haystack. Govind *et al.*⁹¹ used a 3D-MRSI sequence to scan 20 mild and 9 moderate TBI patients and found a widespread decrease of NAA and NAA/Cr, and increases of Cho and Cho/NAA, within all lobes of the TBI subject group, and with the largest differences seen in WM. Examination of the association between all of the metabolite measures and the neuropsychological test scores found the strongest negative correlations to occur in the frontal lobe and for Cho/NAA.

One caveat of the previous MRS work on TBI is that Cr has been used as an internal reference with the assumption that Cr levels will remain constant after injury.⁹ However, this might not be true in an injured brain, which could have Cr disturbance after TBI. As demonstrated by Gasparovic *et al.*,^{89,90} the Cr increase in mTBI patients at the semi-acute stage might give a false impression of decreased NAA/Cr level. It is therefore important to quantitate metabolite concentrations carefully, particularly after mTBI, to determine possible small changes in all metabolites. Comparing metabolite ratios may mask important metabolite changes.

2.6 Perfusion Imaging

After the primary brain damage occurs, even more devastating secondary brain injuries can occur.⁹² This usually includes, but is not limited to, ischemic and hypoxic damage, cerebral swelling, rise of intracranial pressure, hydrocephalus, and infection⁹³ in moderate to severe TBI patients at the acute stage. The injury to the brain can result in disturbance of cerebral blood flow (CBF), which correlates with poor brain tissue oxygenation,⁹⁴ and unfavorable neurological outcome,⁹⁵ which is implicated in rendering the brain vulnerable to secondary damage.⁹⁵ It has been recognized that the failure of brain perfusion is the most common type of hypoxic-ischemic brain damage, but is difficult to identify even in histological studies.⁹³ Cerebral ischemia (CBF \leq 18 mL/100 g/min) is present in approximately 90% of patients who die with head injury.^{92,96,97} Furthermore, after TBI, the uncoupling between CBF and brain metabolic demand

occurs, whereby local cerebral glucose demand increases and local CBF is disturbed due to damage to the vascular muscle tone and arterioles.⁹⁸ The early hyper-glycolysis is thought to be due to the cellular efforts to reestablish ionic gradients.⁹⁵ Different aspects of ischemia and/or edema after injury can be quantified using perfusion imaging, including perfusion weighted imaging (PWI) and arterial spin labeling (ASL), and DWI/DTI. Kim *et al.*¹⁷ used ASL to measure the resting state CBF in 28 moderate to severe TBI at chronic stage and found a) a global decrease of CBF in TBI patients than that in controls, and b) prominent regional hypoperfusion in the posterior cingulate cortices, the thalami, and multiple locations in the frontal cortices.

However, in the population of mTBI, how cerebral perfusion is being affected in patients and their association with patients' neurocognitive status is still less understood. Given the milder severity in mTBI patients, perfusion imaging at the acute stage could be meaningful both for clinical decision-making and patients' outcome prediction. Ge *et al.*⁶¹ also employed ASL to study 21 mTBI patients at the chronic stage and demonstrated reduced CBF in both sides of the thalamus, which is correlated with the patients' speed of information processing, memory, verbal, and executive function.

In summary, our knowledge is very limited in the understanding of cerebral blood flow and its impact to mTBI patients. Perfusion imaging of mTBI, particularly at the acute stage, might shed new light in our understanding of this disease.

2.7 Delivering Improved Care to Patients with mTBI

AQ7

Despite the fact that the ED sees the majority of patients with mTBI,⁹⁹ most stay only a few hours and then are discharged home. After that, most patients fail to be followed up. The acute stage, within 24 hours after injury, is the critical time point for imaging to deliver a real impact to medicine.¹⁰⁰ Either improved detection or outcome prediction will greatly help emergency physicians develop a better referral pattern or management plan for the patient or notify the patient's family members to arrange necessary resources in advance. However, most of the patients with mTBI at the acute stage do not get an MRI scan due to the high cost for medical insurance and the lack of accessibility to an MRI magnet. To date, very few studies are designed to target this critical time point. There is an urgent need for a comprehensive use of advanced MRI techniques to evaluate the patients from the acute setting (within 24 hours) to the chronic stage after injury to identify the association between injury pathology and outcome. In the future, with the availability of MR magnets in the ED and reduced costs for an MRI scan, routinely scanning mTBI patients at the acute stage will be possible. However, to determine who will get MRI scan in ED will be another issue, due to cost. In conjunction with other biochemical markers, a policy on clinical decision making would be expected to define a subgroup of patients for MRI scan.

2.8 Conclusions

MRI has demonstrated superior capabilities over CT in the detection of subtle changes of the brain after mTBI. As an advanced MRI technique, DTI can detect white matter abnormalities that are unseen in structural MRI and further map it with a patient's specific domain of neuropsychological symptoms. Other advanced MRI techniques also demonstrate the potential to detect other types of brain pathologies, including SWI for microhemorrhage detection, MRS for measuring abnormal cerebral metabolites, and perfusion imaging for detecting cerebral blood flow disturbances. In the future, these advanced MRI techniques should be used in a comprehensive way in a large cohort of patients to provide a panorama view of brain pathologies. The MRI investigations at the acute stage, within 24 hours after injury, will most likely impact emergency medicine, which is at the forefront of mTBI care. Furthermore, conjunctional use of imaging with other biological markers, such as serum biomarkers, will likely help screen patients who really need MRI in the acute setting.

Uncited reference

26

References

1. T. Kay, *J. Head Trauma Rehabil.*, 1993, **8**, 74.
2. National Institutes of Health, *JAMA*, 1999, **282**, 974.
3. CDC, *Report to Congress on Mild Traumatic Brain Injury in the United States: Steps to Prevent a Serious Public Health Problem*, Centers for Disease Control and Prevention, National Center for Injury Prevention and Control, Atlanta (GA), 2003.
4. J. J. Bazarian, J. McClung, M. N. Shah, Y. T. Cheng, W. Flesher and J. Kraus, *Brain Injury*, 2005, **19**, 85–91.
5. R. Ruff, *J. Head Trauma Rehabil.*, 2005, **20**, 5.
6. W. Alves, S. N. Macciocchi and J. T. Barth, *J. Head Trauma Rehabil.*, 1993, **8**, 48.
7. J. J. Bazarian, T. Wong, M. Harris, N. Leahey, S. Mookerjee and M. Dombovy, *Brain Inj.*, 1999, **13**, 173.
8. D. Warden, *J. Head Trauma Rehabil.*, 2006, **21**, 398.
9. H. G. Belanger, R. D. Vanderploeg, G. Curtiss and D. L. Warden, *J. Neuropsychiatry Clin. Neurosci.*, 2007, **19**, 5.
10. National Academy of Neuropsychology, *Mild Traumatic Brain Injury – An Online Course*, National Academy of Neuropsychology, Denver (CO), 2002.
11. E. Teasdale and D. M. Hadley, in *Head Injury*, ed. P. Reilly and R. Bullock, Chapman & Hall, London, 1997, p. 167.
12. A. Tellier, L. C. Della Malva, A. Cwinn, S. Grahovac, W. Morrish and M. Brennan-Barnes, *Brain Inj.*, 1999, **13**, 463.

13. K. A. Tong, S. Ashwal, B. A. Holshouser, L. A. Shutter, G. Herigault, E. M. Haacke and D. Kido, *Radiology*, 2003, **27**, 332. 1
14. B. A. Holshouser, K. A. Tong, S. Ashwal, U. Oyoyo, M. Ghamsary, D. Saunders and L. Shutter, *J. Magn. Reson. Imaging*, 2006, **24**, 33.
15. A. Marmarou, S. Signoretti, P. P. Fatouros, G. Portella, G. A. Aygok and M. R. Bullock, *J. Neurosurg.*, 2006, **104**, 720. 5
16. R. R. Benson, S. A. Meda, S. Vasudevan, Z. Kou, K. A. Govindarajan, R. A. Hanks, S. R. Millis, M. Makki, Z. Latif, W. Coplin, J. Meythaler and E. M. Haacke, *J. Neurotrauma*, 2007, **24**, 446.
17. J. Kim, J. Whyte, S. Patel, B. Avants, E. Europa, J. Wang, J. Slattery, J. C. Gee, H. B. Coslett and J. A. Detre, *J. Neurotrauma*, 2010, **27**, 1399. 10
18. T. W. McAllister, A. J. Saykin, L. A. Flashman, M. B. Sparling, S. C. Johnson, S. J. Guerin, A. C. Mamourian, J. B. Weaver and N. Yanofsky, *Neurology*, 1999, **53**, 1300.
19. Z. Kou, Z. Wu, K. A. Tong, B. A. Holshouser, R. R. Benson, J. Hu and E. M. Haacke. 15
- AQ8 20. S. Margulies and R. Hicks, *J. Neurotrauma*, 2009, **26**, 925.
- AQ9 21. T. B. Fay, K. O. Yeates, H. G. Taylor, B. Bangert, A. Dietrich, K. E. Nuss, J. Rusin and M. Wright.
- AQ10 22. N. B. Topal, B. Hakyemez, C. Erdogan, M. Bulut, O. Koksall, S. Akkose, S. Dogan, M. Parlak, H. Ozguc and E. Korfali, *Neurol. Res.*, 2008, **30**, 974. 20
23. H. Lee, M. Wintermark, A. D. Gean, J. Ghajar, G. T. Manley and P. Mukherjee, *J. Neurotrauma*, 2008, **25**, 1049.
24. K. Müller, T. Ingebrigtsen, T. Wilsgaard, G. Wikran, T. Fagerheim, B. Romner and K. Waterloo, *Neurosurgery*, 2009. 25
- AQ11 25. E. Kurca, S. Sivak and P. Kucera, *Neuroradiology*, 2006, **48**, 661.
26. K. Paterakis, A. H. Karantanas, A. Komnos and Z Volikas, *J. Trauma*, 2000, **49**, 1071.
27. J. R. Reichenbach, R. Venkatesan, D. J. Schillinger, D. K. Kido and E. M. Haacke, *Radiology*, 1997, **204**, 272. 30
28. K. A. Tong, S. Ashwal, B. A. Holshouser, J. P. Nickerson, C. J. Wall, L. A. Shutter, R. J. Osterdock, E. M. Haacke and D. Kido, *Ann. Neurol.*, 2004, **56**, 36.
29. T. Babikian, M. C. Freier, K. A. Tong, J. P. Nickerson, C. J. Wall, B. A. Holshouser, T. Burley, M. L. Riggs and S. Ashwal, *Pediatr. Neurol.*, 2005, **33**, 184. 35
30. Z. Kou, R. R. Benson and E. M. Haacke, in *Clinical MR Neuroimaging*, 2nd edn, ed. J. Gillard, A. Waldman and P. Barker, Cambridge University Press, Cambridge, 2010.
31. K. R. Thulborn, A. G. Sorensen, N. W. Kowall, A. McKee, A. Lai, R. C. McKinstry, J. Moore, B. R. Rosen and T. J. Brady, *AJNR Am. J. Neuroradiol.*, 1990, **11**, 291. 40
32. W. G. Bradley, *Radiology*, 1993, **189**, 15.
33. C. L. Mac Donald, K. Dikranian, S. K. Song, P. V. Bayly, D. M. Holtzman and D. L. Brody, *Exp. Neurol.*, 2007, **205**, 116. 45

34. Z. Kou, Y. Shen, N. Zakaria, S. Kallakuri, J. M. Cavanaugh, Y. Yu, J. Hu and E. M. Haacke, in *Joint Annual Meeting ISMRM-ESMRMB*, Berlin, Germany, 2007, Abstract 824, p. 186. 1
35. J. S. Shimony, R. C. McKinstry, E. Akbudak, J. A. Aronovitz, A. Z. Snyder, N. F. Lori, T. S. Cull and T. E. Conturo, *Radiology*, 1999, **212**, 770. 5
36. T. E. Conturo, R. C. McKinstry, E. Akbudak and B. H. Robinson, *Magn. Reson. Med.*, 1996, **35**, 399.
37. S. N. Niogi and P. Mukherjee, *J. Head Trauma Rehabil.*, 2010, **25**, 241.
38. Z. Chu, E. A. Wilde, J. V. Hunter, S. R. McCauley, E. D. Bigler, M. Troyanskaya, R. Yallampalli, J. M. Chia and H. S. Levin, *AJNR Am. J. Neuroradiol.*, 2010, **31**, 340. 10
39. T. C. Wu, E. A. Wilde, E. D. Bigler, R. Yallampalli, S. R. McCauley, M. Troyanskaya, Z. Chu, X. Li, G. Hanten, J. V. Hunter and H. S. Levin, *J. Neurotrauma*, 2010, **27**.
40. E. A. Wilde, S. R. McCauley, J. V. Hunter, E. D. Bigler, Z. Chu, Z. J. Wang, G. R. Hanten, M. Troyanskaya, R. Yallampalli, X. Li, J. Chia and H. S. Levin, *Neurology*, 2008, **70**, 948. 15
41. J. J. Bazarian, J. Zhong, B. Blyth, T. Zhu, V. Kavcic and D. Peterson, *J. Neurotrauma*, 2007, **24**, 1447.
42. A. R. Mayer, J. Ling, M. V. Mannell, C. Gasparovic, J. P. Phillips, D. Doezenia, R. Reichard and R. A. Yeo, *Neurology*, 2010, **74**, 643. 20
43. M. Inglese, S. Makani, G. Johnson, B. A. Cohen, J. A. Silver, O. Gonen and R. I. Grossman, *J. Neurosurg.*, 2005, **103**, 298.
44. K. Arfanakis, V. M. Haughton, J. D. Carew, B. P. Rogers, R. J. Dempsey and M. E. Meyerand, *Am. J. Neuroradiol.*, 2002, **23**, 794. 25
45. A. Messé, S. Caplain, G. Paradot, D. Garrigue, J. F. Mineo, G. Soto Ares, D. Ducreux, F. Vignaud, G. Rozec, H. Desal, M. Pélérini-Issac, M. Montreuil, H. Benali and S. Lehericy, *Human Brain Mapping*, 2011, **32**, 999.
46. M. L. Lipton, E. Gulko, M. E. Zimmerman, B. W. Friedman, M. Kim, E. Gellella, T. Gold, K. Shifteh, B. A. Ardekani and C. A. Branch, *Radiology*, 2009, **252**, 816. 30
47. L. Miles, R. I. Grossman, G. Johnson, J. S. Babb, L. Diller and M. Inglese, *Brain Inj.*, 2008, **22**, 115.
48. V. A. Cubon, M. Putukian, C. Boyer and A. Dettwiler, *J. Neurotrauma*, 2011, **28**, 189. 35
49. C. Lo, K. Shifteh, T. Gold, J. A. Bello and M. L. Lipton, *J. Comput. Assist. Tomogr.*, 2009, **33**, 293.
50. S. N. Niogi, P. Mukherjee, J. Ghajar, C. Johnson, R. A. Kolster, R. Sarkar, H. Lee, M. Meeker, R. D. Zimmerman, G. T. Manley and B. D. McCandliss, *AJNR Am. J. Neuroradiol.*, 2008, **29**, 967. 40
51. V. F. Newcombe, G. B. Williams, J. Nortje, P. G. Bradley, S. G. Harding, P. Smielewski, J. P. Coles, B. Maiya, J. H. Gillard, P. J. Hutchinson, J. D. Pickard, T. A. Carpenter and D. K. Menon, *Br. J. Neurosurg.*, 2007, **21**, 340. 45

52. H. S. Levin, E. A. Wilde, Z. Chu, R. Yallampalli, G. R. Hanten, X. Li, J. Chia, A. C. Vasquez and J. V. Hunter, *J. Head Trauma Rehabil.*, 2008, **23**, 197. 1
53. Z. Kou, R. Gattu, R. R. Benson, N. Raz and E. M. Haacke, *Proc. Intl. Soc. Mag. Reson. Med.*, 2008, **16**, 2272. 5
54. J. R. Wozniak, L. Krach, E. Ward, B. A. Mueller, R. Muetzel, S. Schnoebelen, A. Kiragu and K. O. Lim, *Arch. Clin. Neuropsychol.*, 2007, **22**, 555.
55. D. R. Rutgers, P. Fillard, G. Paradot, M. Tadié, P. Lasjaunias and D. Ducreux, *AJNR Am. J. Neuroradiol.*, 2008, **29**, 1730. 10
56. M. F. Kraus, T. Susmaras, B. P. Caughlin, C. J. Walker, J. A. Sweeney and D. M. Little, *Brain*, 2007, **130**, 2508.
57. A. Sidaros, A. W. Engberg, K. Sidaros, M. G. Liptrot, M. Herning, P. Petersen, O. B. Paulson, T. L. Jernigan and E. Rostrup, *Brain*, 2008, **131**, 559. 15
58. R. Kumar, S. Saksena, M. Hussain, A. Srivastava, R. K. Rathore, S. Agarwal and R. K. Gupta, *J. Head Trauma Rehabil.*, 2010, **25**, 31.
59. S. N. Niogi, P. Mukherjee, C. E. Ghajar, C. E. Johnson, R. Kolster, H. Lee, M. Suh, R. D. Zimmerman, G. T. Manley and B. D. McCandliss, *Brain*, 2008, **131**, 3209. 20
60. E. J. Grossman, Y. Ge, J. H. Jensen, J. S. Babb, L. Miles, J. Reaume, J. M. Silver, R. I. Grossman and M. Inglese, *J. Neurotrauma*, 2011. **AQ13**
61. Y. Ge, M. B. Patel, Q. Chen, E. J. Grossman, K. Zhang, L. Miles, J. S. Babb, J. Reaume and R. I. Grossman, *Brain Inj.*, 2009, **23**. **AQ14**
62. M. L. Lipton, E. Gellella, C. Lo, T. Gold, B. A. Ardekani, K. Shifteh, J. A. Bello and C. A. Branch, *J. Neurotrauma*, 2008, **25**, 1335. 25
63. C. L. MacDonald, A. M. Johnson, D. Cooper, E. C. Nelson, N. J. Werner, J. S. Shimony, A. Z. Snyder, M. E. Raichle, J. R. Witherow, R. Fang, S. F. Flaherty and D. L. Brody, *N. Engl. J. Med.*, 2011, **364**, 2091.
64. S. R. Sponheim, K. A. McGuire, S. S. Kang, N. D. Davenport, S. Aviyente, E. M. Bernat and K. O. Lim, *Neuroimage*, 2011, **54**, S21. 30
65. S. C. Matthews, I. A. Strigo, A. N. Simmons, R. M. O'Connell, L. E. Reinhardt and S. A. Moseley, *Neuroimage*, 2011, **54**, s69. **AQ15**
66. D. R. Rutgers, F. Toulgoat, J. Cazejust, P. Fillard, P. Lasjaunias and D. Ducreux, *AJNR Am. J. Neuroradiol.*, 2008, **29**, 514. 35
67. S. M. Smith, M. Jenkinson, H. Johansen-Berg, D. Rueckert, T. E. Nichols, C. E. Mackay, K. E. Watkins, O. Ciccarelli, M. Z. Cader, P. M. Matthews and T. E. Behrens, *Neuroimage*, 2006, **31**, 1487.
68. B. Alessandri, E. Döppenberg, A. Zauner, J. Woodward, S. Choi and R. Bullock, *Acta Neurochir. Suppl. (Wien)*, 1999, **75**, 25. 40
69. B. A. Holshouser, S. Ashwal, G. Y. Luh, S. Shu, S. Kahlon, K. L. Auld, L. G. Tomasi, R. M. Perkin and D. B. Hinshaw, Jr, *Radiology*, 1997, **202**, 487.
70. B. A. Holshouser, S. Ashwal, S. Shu and D. B. Hinshaw, Jr, *J. Magn. Reson. Imaging*, 2000, **11**, 9.
71. L. Shutter, K. A. Tong and B. A. Holshouser, *J. Neurotrauma*, 2004, **21**, 1693. 45

72. B. A. Holshouser, K. A. Tong, S. Ashwal, U. Oyoyo, M. Ghamsary, D. Saunders and L. Shutter, *J. Magn. Reson. Imaging*, 2006, **24**, 33. 1
73. M. R. Garnett, A. M. Blamire, B. Rajagopalan, P. Styles and T. A. D. Cadoux-Hudson, *Brain*, 2000, **123**, 1403.
74. M. R. Garnett, R. G. Corkill, A. M. Blamire, B. Rajagopalan, D. N. Manners, J. D. Young, P. Styles and T. A. D. Cadoux-Hudson, *J. Neurotrauma*, 2001, **18**, 231. 5
75. W. M. Brooks, C. A. Stidley, H. Petropoulos, R. E. Jung, D. C. Weers, S. D. Friedman, M. A. Barlow, W. L. Sibbett and R. A. Yeo, *J. Neurotrauma*, 2000, **17**, 629. 10
76. S. D. Friedman, W. M. Brooks, R. E. Jung, B. L. Hart and R. A. Yeo, *AJNR Am J Neuroradiol.*, 1998, **19**, 1879.
77. T. Brenner, M. C. Freier, B. A. Holshouser, T. Burley and S. Ashwal, *Pediatr. Neurol.*, 2003, **28**, 104.
78. T. Babikian, M. C. Freier, S. Ashwal, M. L. Riggs, T. Burley and B. A. Holshouser, *J. Magn. Reson. Imag.*, 2006, **24**, 801. 15
79. R. A. Yeo, J. P. Phillips, R. E. Jung, A. J. Brown, R. C. Campbell and W. M. Brooks, *J. Neurotrauma*, 2006, **23**, 1427.
80. S. J. Yoon, J. H. Lee, S. T. Kim and M. H. Chun, *Clin. Rehabil.*, 2005, **19**, 209. 20
81. S. Signoretti, A. Marmarou, P. Fatouros, R. Hoyle, A. Beaumont, S. Sawauchi, R. Bullock and H. Young, *Acta Neurochir. Suppl.*, 2002, **81**, 373.
82. M. R. Garnett, A. M. Blamire, R. G. Corkill, T. A. D. Cadoux-Hudson, B. Rajagopalan and P. Styles, *Brain*, 2000, **123**, 2046.
83. S. D. Friedman, W. M. Brooks, R. E. Jung, S. J. Chiulli, J. H. Sloan, B. T. Montoya, B. L. Hart and R. A. Yeo, *Neurology*, 1999, **52**, 1384. 25
84. B. D. Ross, T. Ernst, R. Kreis, L. J. Haseler, S. Bayer, E. Danielsen, S. Bluml, T. Shonk, J. C. Mandigo, W. Caton, C. Clark, S. W. Jensen, N. L. Lehman, E. Arcinue, R. Pudenz and C. H. Shelden, *J. Magn. Reson. Imag.*, 1998, **8**, 829. 30
85. I. Kirov, L. Fleysheer, J. S. Babb, J. M. Silver, R. I. Grossman and O. Gonen, *Brain Inj.*, 2007, **21**, 1147.
86. B. A. Cohen, M. Inglese, H. Rusinek, J. S. Babb, R. I. Grossman and O. Gonen, *AJNR Am. J. Neuroradiol.*, 2007, **28**, 907.
87. V. Govindaraju, G. E. Gauger, G. T. Manley, A. Ebel, M. Meeker and A. A. Maudsley, *AJNR Am. J. Neuroradiol.*, 2004, **25**, 730. 35
88. M. R. Garnett, A. M. Blamire, B. Rajagopalan, P. Styles and T. A. D. Cadoux-Hudson, *Brain*, 2000, **123**, 1403.
89. C. Gasparovic, R. Yeo, M. Mannell, J. Ling, R. Elgie, J. Phillips, D. Doezenia and A. R. Mayer, *J. Neurotrauma*, 2009, **26**, 1635. 40
90. R. A. Yeo, C. Gasparovic, F. Merideth, D. Ruhl, D. Doezenia and A. R. Mayer, *J. Neurotrauma*, 2011, **28**, 1.
91. V. Govind, S. Gold, K. Kaliannan, G. Saigal, S. Falcone, K. L. Arheart, L. Harris, J. Jagid and A. A. Maudsley, *J. Neurotrauma*, 2010, **27**, 483.
92. A. D. Mendelow and P. J. Crawford, in *Head Injury*, ed. P. Riley and R. Bullock, Chapman & Hall, London, 1997, p. 71. 45

93. P. C. Blumbergs, in *Head Injury*, ed. P. Reilly and R. Bullock, Chapman & Hill, London, 1997, p. 39. 1
94. A. Zauner, W. P. Daugherty, M. R. Bullock and D. S. Warner, *Neurosurgery*, 2002, **51**, 289.
95. E. M. Golding, *Brain Res. Brain Res. Rev.*, 2002, **38**, 377. 5
96. D. I. Graham, J. H. Adams and E. Doyle, *J. Neurol. Sci.*, 1978, **39**, 213.
97. D. I. Graham, I. Ford, J. H. Adams, D. Doyle, G. M. Teasdale, A. E. Lawrence and D. R. McLellan, *J. Neurol. Neurosurg. Psychiatry*, 1989, **52**, 346.
98. E. M. Golding, C. S. Robertson and R. M. Bryan, Jr, *Clin. Exp. Hypertens.*, 1999, **21**, 299. 10
99. J. J. Bazarian, J. McClung, Y. T. Cheng, W. Flesher and S. M. Schneider, *Emerg. Med. J.*, 2005, **22**, 473.
100. A. S. Jagoda, J. J. Bazarian, J. J. Bruns, Jr, S. V. Cantrill, A. D. Gean, P. K. Howard, J. Ghajar, S. Riggio, D. W. Wright, R. L. Wears, A. Bakshy, P. Burgess, M. M. Wald and R. R. Whitson, *Ann. Emerg. Med.*, 2008, **52**, 714. 15
101. J. D. Lewine, J. T. Davis, E. D. Bigler, R. Thoma, D. Hill, M. Funke, J. H. Sloan, S. Hall and W. W. Orrison, *J. Head Trauma Rehabil.*, 2007, **22**, 141. 20
102. M. Inglese, R. I. Grossman, L. Diller, J. S. Babb, O. Gonen, J. M. Silver and H. Rusinek, *Brain Inj.*, 2006, **20**, 15.
103. R. A. Yeo, C. Gasparovic, F. Merideth, D. Ruhl, D. Doezeema and A. R. Mayer, *J. Neurotrauma*, 2011, **28**, 1.
104. K. K. Holli, M. Wäljas, L. Harrison, S. Liimatainen, T. Luukkaala, P. Ryymin, H. Eskola, S. Soimakallio, J. Ohman and P. Dastidar, *Acad. Radiol.*, 2010, **17**, 1096. 25
105. K. K. Holli, L. Harrison, P. Dastidar, M. Wäljas, S. Liimatainen, T. Luukkaala, J. Ohman, S. Soimakallio and H. Eskola, *BMC Med. Imaging*, 2010, **10**. 30